Universidade Federal de Minas Gerais

Graduate Program in Metallurgical, Materials, and Mining Engineering (PPGEM)

Synthesis of TiO_2@MOF composites for the photodegradation of organic pollutants

Síntese de compósitos do tipo TiO_2@MOF com aplicação na fotodegradação de poluentes orgânicos

Master dissertation

Pedro Henrique Morais Andrade

Advisor: Prof. Eduardo Henrique Martins Nunes

Co-advisor: Prof. Manuel Houmard

Belo Horizonte

July 2021

PEDRO HENRIQUE MORAIS ANDRADE

“SYNTHESIS OF TiO_2@MOF COMPOSITES FOR THE PHOTODEGRADATION OF ORGANIC POLLUTANTS”

Master’s dissertation proposal presented to the Graduate Program in Metallurgical Engineering, Materials and Mining (PPGEM), from the Engineering School of the Federal University of Minas Gerais, as a partial requirement to obtain the master’s degree in Metallurgical Engineering, Materials and Mining.

Concentration area: Materials Science and Engineering

Advisor: Prof. Eduardo H. M. Nunes
Co-advisor: Prof. Manuel Houmard

Belo Horizonte
July 2021

A553s

Andrade, Pedro Henrique Morais.
Synthesis of TiO_2@MOF composites for the photodegradation of organic pollutants [recurso eletrônico] / Pedro Henrique Morais Andrade. - 2021.
1 recurso online (xiii, 91 f. : il., color.) : pdf.

Orientador: Eduardo H. M. Nunes.
Coorientador: Manuel Houmard.

Dissertação (mestrado) - Universidade Federal de Minas Gerais, Escola de Engenharia.

Bibliografia: f. 76-91.
Exigências do sistema: Adobe Acrobat Reader.

1. Materiais - Teses. 2. Ciência dos materiais - Teses. 3. Diclofenaco - Teses. 3. Dióxido de titânio - Teses. 4. Fotocatálise - Teses. I. Nunes, Eduardo Henrique Martins. II. Houmard, Manuel. III. Universidade Federal de Minas Gerais. Escola de Engenharia. IV. Título.

CDU: 620(043)

Ficha catalográfica elaborada pelo bibliotecário Reginaldo Cesar Vital dos Santos CRB/6 2165
Biblioteca Prof. Mário Werneck, Escola de Engenharia da UFMG

UNIVERSIDADE FEDERAL DE MINAS GERAIS
ESCOLA DE ENGENHARIA
Programa de Pós-Graduação em Engenharia
Metalúrgica, Materiais e de Minas

Dissertação intitulada **"Synthesis of TiO_2@MOF composites for the photodegradation of organic pollutants"**, área de concentração: Ciência e Engenharia de Materiais, apresentada pelo candidato **Pedro Henrique Morais Andrade**, para obtenção do grau de Mestre em Engenharia Metalúrgica, Materiais e de Minas, aprovada pela comissão examinadora constituída pelos seguintes membros:

Prof. Eduardo Henrique Martins Nunes
Orientador - Dr. (UFMG)

Prof. Manuel Houmard Dr.
(UFMG)

Prof. Christophe Volkringer Dr.
(École Centralle de Lille)

Prof. Alain Moissette Dr.
(Université de Lille)

Rodrigo Lambert Oréfice
____
Coordenador do Programa de Pós-Graduação em
Engenharia Metalúrgica, Materiais e de Minas/UFMG

Belo Horizonte, 07 de julho de 2021

ACKNOWLEDGEMENTS

I would like to thank all those who directly or indirectly collaborated in the preparation of this work and, in particular, my mother Ana Morais, my sister Ana Luisa, my father Sidinai Andrade, my companion Larissa Araújo, my family and my friends for their commitment and support throughout this journey, for the moments of fraternization and for the lightness of spirit. To my tutor Prof. Eduardo Nunes and to my co-tutor Prof. Manuel Houmard, for the support, availability and help during all his formation. To the collaborators of this project, Prof. Alain Moisette and Prof. Christophe Volkringer, for the contribution and cooperation among different departments, besides the supply of materials and space that were fundamental in the execution of this project. To the other professors of UFMG (*Universidade Federal de Minas Gerais),* Prof. Cláudia Windmöller and Prof. Marivalda Pereira, who were of fundamental importance in my academic formation. To Leonardo Mayer, Samuel Lima and Leonardo de Souza for their contribution with the chemical and structural characterizations of this work, besides the immense sympathy and availability. To CAPES (*Coordenação e Aperfeiçoamento de Pessoal de Nível Superior*) and to Prof. Jean-Bernard Vogt and Prof. Vicente Buono, for their opportunity and proactivity in the maintenance of the BRAFITEC project between UFMG and ENSCL (*École Nationale Supérieure de Chimie de Lille*). To UFMG, especially DEMET (*Departamento de Engenharia Metalúrgica e de Materiais*) and DQ (*Departamento de Química*), to EC-Lille (*École Centrale de Lille*), especially UCCS (*Unité de Catalyse et Chimie du Solide*) and to ULille (*Université de Lille*), especially LASIRe (*LAboratoire de Spectroscopie pour les Interactions, la Réactivité et l'Environnement),* to CNPq (*Conselho Nacional de Desenvolvimento Científico e Tecnológico*), CAPES, FAPEMIG (*Fundação de Amparo à Pesquisa do Estado de Minas Gerais*) and PRPq-UFMG (*Pró-Reitoria de Pesquisa da UFMG*) for the provision of resources, spaces, materials and financial assistance during the realization of this research. UFMG's Microscopy Center, LEPCom (Prof. Rodrigo Oréfice) and PMEL are acknowledged for the support provided in TEM, UV-Vis and SEM tests, respectively.

SUMMARY

LIST OF PICTURES

LIST OF TABLES

LIST OF RATINGS

- ADF: Annular Dark Field
- AOX: Adsorbable Organic Halogen
- ATR: Attenuated Total Reflectance
- BET: Brunauer, Emmett, Teller
- BF: Bright Field
- BOD: Biochemical Oxygen Demand
- CAPES: *Coordenação de Aperfeiçoamento de Pessoal de Nível Superior*
- CB: Conduction Band
- CNPq: *Conselho Nacional de Desenvolvimento Científico e Tecnológico*
- COD: Chemical Oxygen Demand
- CUS: Coordinatively Unsaturated Sites
- DEMET: *Departamento de Engenharia Metalúrgica e de Materiais*
- DFT: Density-Functional Theory
- DIC: Diclofenac
- DQ: *Departamento de Química*
- DTG: Differential Thermogravimetric Analysis
- EC-Lille : *École Centrale de Lille*
- EDS: Energy Dispersive X-ray Spectroscopy
- EELS: Electron Energy Loss Spectroscopy
- ENSCL: *École Nationale Supérieure de Chimie de Lille*
- FAPEMIG: *Fundação de Amparo à Pesquisa do Estado de Minas Gerais*
- FTIR: Fourier-Transform Infrared Spectroscopy
- GHG: Greenhouse gas
- GIF: Gatan Image Filter
- HKUST: Hong Kong University of Science and Technology
- IBP: Ibuprofen
- IE: Isoreticular Expansion
- LASIRe : *LAboratoire de Spectroscopie pour les Interactions, la Réactivité et l'Environnement*

- LEPCom: *Laboratório de Engenharia de Polímeros e Compósitos*
- MB: Methylene Blue
- MIL: Materials Institute Lavoisier
- MOF: Metal-Organic Framework
- NHE: Normal Hydrogen Electrode
- NSAIDs: Non-Steroidal Anti-Inflammatory Drugs
- PBU: Primary Building Unity
- PMEL: *Plateforme de Microscopie Electronique de Lille*
- PPCPs: Pharmaceutical and Personal care Products
- PRPq-UFMG: *Pró-Reitoria de Pesquisa da UFMG*
- PSM: Post-Synthetic Modification
- SAED: Selected Area Electron Diffraction
- SBU: Secondary Building Unity
- SEM: Scanning Electron Microscopy
- SSA: Specific Surface Area
- TEM: Transmission Electron Microscopy
- TG: Thermogravimetric Analysis
- TSS: Total Suspended Solids
- UCCS : *Unité de Catalyse et Chimie du Solide*
- UFMG: *Universidade Federal de Minas Gerais*
- ULille: *Université de Lille*
- UV-vis: Ultraviolet-Visible Spectroscopy
- VB: Valence Band
- VOCs: Volatile Organic Compounds
- XRD: X-ray Diffraction

ABSTRACT

The contamination of ecosystems with toxic materials is a recurring problem in human history. Pollutants such as heavy metals, organic materials, industrial dyes, radioactive waste, and solvents are commonly found in various environments, causing harmful effects to humans and other species. The pharmaceuticals and personal care products (PPCPs) pose a specific concern due to its extensive use and incorrect disposal around the world, specifically the non-steroidal anti-inflammatory drugs (NSAIDs), with ibuprofen (IBP) and diclofenac (DIC) being on the top list. The use of materials with controlled pore structures is an effective strategy for both capturing and degrading these pollutants. Through adsorption and photocatalysis, these compounds can remove several toxic species present in soil, water, and atmosphere. This work evaluates the adsorption and degradation capacity of methylene blue (MB), IBP, and DIC using the metal-organic frameworks (MOFs) HKUST-1 and MIL-100(Al). The MOFs were synthesized through a hydrothermal treatment and later impregnated with titania, which is a well-established semiconductor worldwide due to its low cost and low toxicity coupled with a high photoactivity and chemical stability. TiO_2 was produced by a sol-gel route without the presence of an acid, using the MOFs as a site for heterogeneous nucleation. In order to evaluate the influence of TiO_2 nanoparticles in the MOFs over their photocatalytic activity, UV-vis kinetic studies were conducted, and the apparent first-order constant (K_{app}) were calculated using the Langmuir-Hinshelwood (L-H) kinetic model. It was observed that aluminum trimesate withstood the modification step, and anatase nanoparticles were successfully anchored onto its surface and within its pore framework. This composite showed an improved capacity of degrading MB, IBP, and DIC under UVA illumination. Copper trimesate, on the other hand, showed a structural collapse during the modification step, probably due its fragility in water-rich media. However, the novel composite material experienced an increase in its photocatalytic activity compared to HKUST-1, due to the presence of crystallized TiO_2 in the form of rutile on its surface. This work contributes to the knowledge about the incorporation of semiconductor nanoparticles into MOFs for photocatalytic applications

KEYWORDS: MOF; HKUST-1; MIL-100(Al); TiO_2; photocatalysis; NSAIDs; ibuprofen; diclofenac.

RESUMO

A contaminação de ecossistemas com materiais tóxicos é um problema recorrente na história. Poluentes como metais pesados, materiais orgânicos, corantes industriais, lixo radioativo e solventes são comumente encontrados em vários ambientes, causando efeitos nocivos aos humanos e outras espécies. Os produtos farmacêuticos e de higiene pessoal (PPCPs) levantam preocupações relacionadas ao seu uso extensivo e ao descarte incorreto em todo o planeta, especificamente os anti-inflamatórios e drogas não esteroidais (NSAIDs), valendo citar o ibuprofeno (IBP) e o diclofenaco (DIC) como um dos principais. O uso de materiais com estrutura de poros controlada é uma alternativa eficiente para capturar e degradar esses poluentes. Através da adsorção e fotocatálise, esses compostos conseguem remover diversas espécies tóxicas presentes no solo, na água e na atmosfera. Esse trabalho avalia a capacidade de adsorção e degradação do azul de metileno (MB), IBP e DIC, usando as redes organometálicas (MOFs) HKUST-1 e MIL-100 (Al). As MOFs foram sintetizadas por meio de um tratamento hidrotérmico e posteriormente impregnadas com titânia, que é um semicondutor bem estabelecido mundialmente, devido ao seu baixo custo e à sua baixa toxicidade aliado a uma alta fotoatividade e estabilidade química. O TiO_2 foi produzido pela rota sol-gel sem a presença de ácido, utilizando as MOFs como matrizes de nucleação heterogênea. A fim de avaliar a influência das nanopartículas de TiO_2 nos MOFs sobre sua atividade fotocatalítica, estudos cinéticos UV-vis foram conduzidos e as constantes aparentes de primeira ordem (Kapp) foram calculadas usando o modelo cinético de Langmuir-Hinshelwood (L-H). Foi observado que o trimesato de alumínio resistiu à etapa de modificação e as nanopartículas de anatasio foram ancoradas com sucesso em sua superfície e dentro de sua estrutura de poros. Esse composto mostrou uma capacidade melhorada de degradar MB, IBP e DIC sob iluminação UVA. O trimesato de cobre, por outro lado, apresentou um colapso estrutural durante a etapa de modificação, provavelmente devido à sua fragilidade em meio rico em água. No entanto, o novo compósito experimentou um aumento em sua atividade fotocatalítica em relação ao HKUST-1, devido à presença de TiO_2 cristalizado na forma de rutilo em sua superfície. Esse trabalho contribui para o conhecimento sobre a incorporação de nanopartículas semicondutoras em MOFs para aplicações fotocatalíticas.

PALAVRAS-CHAVE: MOF; HKUST-1; MIL-100(Al); TiO_2; fotocatálise; NSAIDs; ibuprofeno; diclofenaco.

1 INTRODUCTION

Inadequate disposal of industrial, domestic, and agricultural waste often leads to contamination of aqueous effluents with different compounds such as heavy metals, industrial dyes, oils, organic mixtures, and drugs, which become a serious environmental problem. The increase in industrial production and global consumption has accelerated this phenomenon [1]. In Bangladesh, for example, it is estimated that by 2021 the textile industry will release 349 billion liters of sewage containing industrial dyes into the environment, an increase of 60% within five years [2]. In Brazil, since 1990, several reports point to an excessive increase in the number of pesticides used in the agricultural sector. In 2019 alone, more than 300 pesticides were released in the country [3]. As a consequence, environmental and public health problems have been recorded in ever-increasing numbers [4]. One example is the contamination by organochlorine pesticides (heptachlor, hexachlorocyclohexane, aldrin, chlordane, endrin) of surface and underground waters of the Ipojuca basin in the State of Pernambuco (Brazil), and also of the Primavera do Leste region in the State of Mato Grosso (Brazil) [5,6].

Environmental accidents and industrial crimes can also cause the contamination of waterways abruptly, as occurred in Mariana (2015) and Brumadinho (2019) in the State of Minas Gerais (Brazil). In the first disaster, the mining tailings dam called "Fundão" broke. Controlled by Samarco Mineração S.A., a joint venture between Vale S.A. and BHP Billiton, the dam caused the contamination of more than 62 million cubic meters of water in the Doce River basin [7]. After the catastrophe, arsenic concentrations of 200 mg.kg-1 were found in different locations of the river, about 20 times higher than those found before the accident on the continental shelves of the Southeast Atlantic [8]. The tragedy in Brumadinho was caused by the rupture of the dam of the Feijão stream mine. Again, the venture was controlled by Vale S.A. and, although it caused less environmental damage, it was a social and economic catastrophe for the whole of Brazil. Eight months after the tragedy, the death toll had reached 250, and there were still 20 people missing [9]. Moreover, the social and economic problems generated in the affected regions persist to this day. One example is the Inhotim Institute, one of the largest open-air museums in world. Located in Brumadinho, it had its flow of visitors reduced by half after the dam broke. However, the city also suffered impacts in mining, agriculture, and commerce, which shrank 70% in 2019 [10].

Although the main source of contamination of watercourses worldwide is of industrial origin, society also plays a considerable role in several sectors, such as solid waste and urban sewage. An example of health-damaging contaminants that are often released into the environment are pharmaceutical and personal care products (PPCPs), more specifically, NSAIDs. In the case of these drugs, their incorrect disposal and the fraction of these compounds that is excreted by the body, contributes to this scenario. A study conducted in Brazil reveals that about 66% of respondents say that they dispose of drugs in common garbage, while 72% never received instructions on how to do it properly [11]. Furthermore, after a comprehensive analysis of the literature on water quality in more than 70 countries on all continents, records were found of the presence of about 600 different drugs in samples of surface water, groundwater, and treated water [12]. Among the main contaminants present, it is worth mentioning antibiotics, analgesics, anti-inflammatory, and anti-depressants for their potential damage to human health and marine life [13]. Antibiotics, for example, can promote the proliferation of super resistant bacteria, while the presence of hormones in the water can cause physiological changes in fish, causing male animals to produce eggs [14].

There are different ways in the literature to remove these contaminants in aqueous media, worth mentioning adsorption and photocatalysis. These processes stand out due to their relatively low cost, high efficiency, low environmental impact, ease of operation, and the possibility of reuse the materials [1]. MOFs, in turn, are strong candidates for these applications. They correspond to a class of materials widely used to remove pollutants from liquid and gas media [15–18]. Their structure consists of inorganic clusters connected by organic linkers, leading to highly ordered crystalline porous networks [19,20]. MOFs show a great industrial interest since they exhibit high adsorption capacities [21] and high specific surface areas [22]. Besides, they can be chemically modified by post-synthetic treatments [23] and have tailored pore sizes while maintaining an isoreticular structure [24,25]. Several studies have been conducted aiming to improve their photocatalytic behavior [26–29]. Incorporating semiconductor nanoparticles into their structures has proven to be a promising approach to achieve this goal. Ökte et al. [26] have successfully loaded TiO_2 and ZnO nanoparticles on Cu-btc (btc = 1,3,5-benzenetricarboxylate) surface, also called HKUST-1 (HKUST = Hong Kong University of Science and Technology). Such a modification increased its photoactivity. Another study reported enhancing the photocatalytic oxidation of isopropanol when TiO_2 was added to HKUST-1 [28]. Hu et al. [30] have synthesized TiO_2 nanoparticles in chromium terephthalate MIL-101 (MIL = Materials Institute Lavoisier) structure for the adsorption and degradation of volatile pollutants.

Titanium dioxide (TiO_2 or titania) is one of the most used semiconductors in photocatalysis [31]. Several methods can be used to obtain it [32], but the sol-gel process deserves to be highlighted. This chemical route allows preparing samples with tailored particle size, pore size distribution, and specific surface area. It is well established that the TiO_2 photoactivity is strongly affected by these textural properties [33,34]. In this work, two different MOFs, namely MIL-100(Al) [35] and HKUST-1 [36], were prepared and then modified with sol-gel-derived TiO_2 nanoparticles. MIL-100(Al) was chosen due to its higher thermal and chemical stabilities than HKUST-1, which allowed comparing these properties during TiO_2 incorporation [37,38]. Moreover, it is worth highlighting the expertise of the research group in the preparation of sol-gel derived TiO_2 nanoparticles [31,33]. Scanning electron microscopy (SEM), transmission electron microscopy (TEM), selected area electron diffraction (SAED), electron energy loss spectroscopy (EELS), energy-dispersive X-ray spectroscopy (EDS), Fourier transform infrared spectroscopy (FTIR), Raman spectroscopy, thermogravimetry (TG), ultraviolet- visible (UV-Vis) spectroscopy, X-ray powder diffraction (XRD), spin trapping electron paramagnetic resonance (EPR), N_2 and Kr sorption were used to exam the obtained materials. They were also employed in the photodegradation of IBP and DIC under near-ultraviolet (UVA) light.

This work presents in the second chapter its objectives; in the third chapter, a bibliographic review of the literature about the state of the art associated with the application of MOFs on the photocatalysis of organic materials; in the fourth chapter, the materials and methods used to achieve one’s objective; in the fifth chapter, the results obtained and their discussion which were compared with others published on the literature; and, in the sixth chapter, the conclusion and final considerations..

1 INTRODUÇÃO

O descarte inadequado de resíduos industriais, domésticos e agrícolas frequentemente leva à contaminação de efluentes aquosos com diferentes compostos, como metais pesados, corantes industriais, óleos, misturas orgânicas e medicamentos, que acabam se tornando um sério problema ambiental. O aumento da produção industrial e do consumo global acelerou esse fenômeno [1]. Em Bangladesh, por exemplo, estima-se que até 2021 a indústria têxtil lançará no meio ambiente 349 bilhões de litros de esgoto contendo corantes industriais, um aumento de 60% em cinco anos [2]. No Brasil, desde 1990, diversos relatórios apontam para um aumento excessivo do número de agrotóxicos usados no setor agrícola. Só em 2019, mais de 300 agrotóxicos foram lançados no país [3]. Como consequência, problemas ambientais e de saúde pública têm sido registrados em números cada vez maiores [4]. Um exemplo é a contaminação por pesticidas organoclorados (heptacloro, hexaclorociclohexano, aldrin, clordano, endrina) de águas superficiais e subterrâneas da bacia do Ipojuca no Estado de Pernambuco (Brasil) e da região de Primavera do Leste no Estado de Mato Grosso (Brasil) [5,6].

Acidentes ambientais e crimes industriais também podem causar a contaminação de cursos d'água de forma abrupta, como ocorreu em Mariana (2015) e Brumadinho (2019) no Estado de Minas Gerais (Brasil). No primeiro desastre, a barragem de rejeitos de mineração denominada "Fundão" rompeu. Controlada pela Samarco Mineração S.A., empreendimento conjunto entre a Vale S.A. e a BHP Billiton, a barragem causou a contaminação de mais de 62 milhões de metros cúbicos de água na bacia do rio Doce [7]. Após a catástrofe, concentrações de arsênio de 200 mg.kg-1 foram encontradas em diferentes locais do rio, cerca de 20 vezes maiores do que as encontradas antes do acidente nas plataformas continentais do Atlântico Sudeste [8]. A tragédia de Brumadinho foi provocada pelo rompimento da barragem da mina do córrego Feijão. Mais uma vez, o empreendimento foi controlado pela Vale S.A. e, embora tenha causado menos danos ambientais, foi uma catástrofe social e econômica para todo o Brasil. Oito meses após a tragédia, o número de mortos chegou a 250 e ainda havia 20 pessoas desaparecidas [9]. Além disso, os problemas sociais e econômicos gerados nas regiões afetadas persistem até hoje. Um exemplo é o Instituto Inhotim, um dos maiores museus a céu aberto do mundo. Localizado em Brumadinho, teve seu fluxo de visitantes reduzido pela metade com o rompimento da barragem. No entanto, a cidade também sofreu impactos na mineração, agricultura e comércio. Esse encolheu 70% em 2019 [10].

Embora a principal fonte de contaminação de cursos d'água em todo o mundo seja de origem industrial, a sociedade também desempenha um papel considerável em diversos setores, como resíduos sólidos e esgoto urbano. Um exemplo de contaminantes prejudiciais à saúde que muitas vezes são liberados no meio ambiente são os produtos farmacêuticos e de higiene pessoal (PPCPs), mais especificamente, os NSAIDs. No caso dessas drogas, o seu descarte incorreto e a fração desses compostos que é excretada pelo organismo contribuem para esse quadro. Um estudo realizado no Brasil revela que cerca de 66% dos entrevistados afirmam que jogam as drogas no lixo comum, enquanto 72% nunca receberam orientações sobre como fazê-lo de maneira adequada [11]. Além disso, após uma análise abrangente da literatura sobre a qualidade da água em mais de 70 países em todos os continentes, foram encontrados registros da presença de cerca de 600 medicamentos diferentes em amostras de águas superficiais, subterrâneas e tratadas [12]. Dentre os principais contaminantes presentes, vale citar os antibióticos, analgésicos, anti-inflamatórios e antidepressivos por seus potenciais danos à saúde humana e à vida marinha [13]. Os antibióticos, por exemplo, podem promover a proliferação de bactérias super-resistentes, enquanto a presença de hormônios na água pode causar alterações fisiológicas nos peixes, fazendo com que os machos produzam ovos [14].

Existem diferentes formas na literatura de remoção desses contaminantes em meio aquoso, com destaque para a adsorção e fotocatálise. Esses processos se destacam pelo custo relativamente baixo, alta eficiência, baixo impacto ambiental, facilidade de operação e possibilidade de reaproveitamento dos materiais [1]. As MOFs, por sua vez, são fortes candidatas para essas aplicações. Elas correspondem a uma classe de materiais amplamente utilizados para remover poluentes de meios líquidos e gasosos [15-18]. Sua estrutura consiste em aglomerados inorgânicos conectados por ligantes orgânicos, formando redes cristalinas porosas altamente ordenadas [19,20]. MOFs apresentam grande interesse industrial, uma vez que exibem altas capacidades de adsorção [21] e altas áreas superficiais específicas [22]. Além disso, elas podem ser modificadas quimicamente por tratamentos pós-síntese [23] e têm tamanhos de poros sob medida, mantendo uma estrutura isoreticular [24,25]. Vários estudos foram conduzidos com o objetivo de melhorar seu comportamento fotocatalítico [26-29]. Incorporar nanopartículas semicondutoras em suas estruturas tem se mostrado uma abordagem promissora para atingir esse objetivo. Ökte et al. [26] carregaram com sucesso nanopartículas de TiO_2 e ZnO na superfície de Cu-btc (btc = 1,3,5-benzenotricarboxilato), também chamada de HKUST-1 (HKUST = *Hong Kong University of Science and Technology*). Essa modificação aumentou sua fotoatividade. Outro estudo relatou o aumento da oxidação fotocatalítica do isopropanol quando TiO_2 foi adicionado ao HKUST-1 [28]. Hu et al. [30] sintetizaram nanopartículas de TiO_2 na estrutura do tereftalato de cromo MIL-101 (MIL = *Materials Institute Lavoisier*) para a adsorção e degradação de poluentes voláteis.

O dióxido de titânio (TiO_2, ou ainda, titânia) é um dos semicondutores mais usados na fotocatálise [31]. Vários métodos podem ser utilizados para sua obtenção [32], mas o processo sol-gel merece destaque. Esta rota química permite a preparação de amostras com tamanho de partícula, distribuição de tamanho de poros e área de superfície específica sob medida. Está bem estabelecido que a fotoatividade do TiO_2 é fortemente afetada por essas propriedades texturais [33,34]. Neste trabalho, duas MOFs diferentes, MIL-100 (Al) [35] e HKUST-1 [36], foram preparadas e então modificadas com nanopartículas de TiO_2 derivadas de sol-gel. MIL-100(Al) foi escolhida devido às suas maiores estabilidades térmicas e químicas quando comparada à HKUST-1, o que permitiu a análise dessas propriedades durante a incorporação do TiO_2 [37,38]. Além disso, vale destacar a expertise do grupo de pesquisa na preparação de nanopartículas de TiO_2 derivadas de rotas sol-gel [31,33]. Microscopia eletrônica de varredura (SEM), microscopia eletrônica de transmissão (TEM), difração de elétrons de área selecionada (SAED), espectroscopia de perda de energia de elétrons (EELS), espectroscopia de raios-X dispersiva em energia (EDS), espectroscopia infravermelha por transformada de Fourier (FTIR), espectroscopia Raman, termogravimetria (TG), espectroscopia ultravioleta-visível (UV-Vis), difração de pó de raios-X (XRD), ressonância paramagnética de elétrons com armadilhas de spin (EPR), ensaios de adsorção de N_2 e Kr foram utilizados para examinar os materiais obtidos. Eles também foram empregados na fotodegradação de IBP e DIC sob luz ultravioleta (UVA).

Este trabalho apresenta os objetivos no segundo capítulo; no terceiro, é feita uma revisão bibliográfica da literatura sobre o estado da arte associado à aplicação de MOFs na fotocatálise de materiais orgânicos; no quarto capítulo, os materiais e métodos usados para atingir o objetivo são descritos; no quinto, os resultados obtidos são discutidos e comparados com outros publicados na literatura; e, no sexto capítulo, a conclusão e as considerações finais são apresentadas.

2 OBJECTIVES

The main objective of this study is to synthesize hybrid materials from the insertion semiconductor nanoparticles into MOFs. TiO_2 will be used as a semiconductor material. The materials will be characterized according to their chemical and pore structure. Finally, the adsorption capacity and photocatalytic activity of the prepared materials will be evaluated. Thus, during this project it is intended:

(1) To study and elaborate an adapted route of composite materials synthesis from the combination of semiconductor nanoparticles and MOFs.

(2) To characterize the materials obtained according to their chemical properties and pore structure.

(3) To evaluate the photocatalytic activity and the adsorption capacity of the composites produced.

(4) To investigate the mechanisms involved in the adsorption and photocatalysis processes.

(5) To disseminate the knowledge generated through the publication of a scientific paper.

3 BACKGROUND

3.1 Disasters and environmental contamination

The contamination of the atmosphere, soil, and waterways with different materials is a socio- environmental problem in several countries in world such as India, Bangladesh, Brazil, the United States, France, and Norway, among others [39–46]. It is estimated that more than 90% of all water used in the world is discarded without adequate treatment, as shown in Figure 3.1 [47]. The toxic compounds that pollute different ecosystems can be classified into two major groups. Those of natural occurrence, which are present in the air, water, minerals, and soil, are independent of human action. On the other hand, those of anthropogenic occurrence are due to combustion processes and other chemical reactions and the uncontrolled release of toxic waste [48]. Due to the growing socio-environmental impact caused by human action in recent centuries, this work focuses on contaminants of anthropogenic origin.

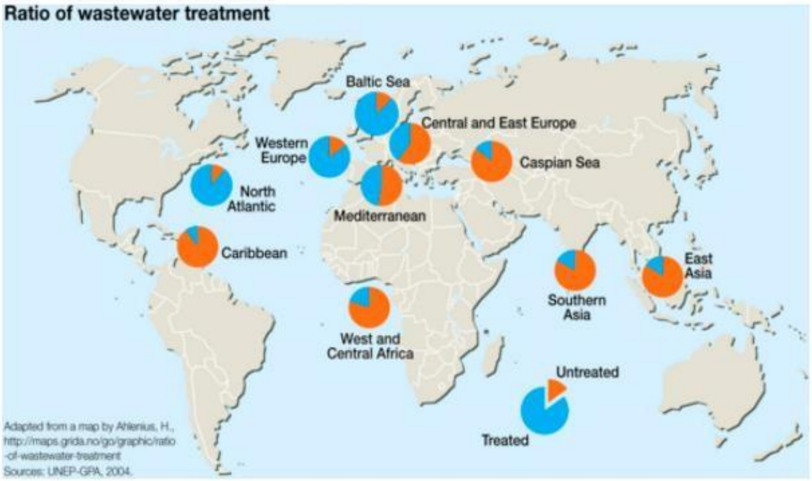

Figure 3.1: Relationship between the release of treated and untreated aqueous residues in different regions of the planet. In the South Atlantic region samples from East and Central Africa were analyzed [47].

Among the hazardous materials found in the environment, some are more important, either because of their high toxicity and difficulty of treatment or because of the enormous quantity in which these contaminants are emitted. Among the main ones, it is worth mentioning the greenhouse gases - GHGs (CO_2, CH_4, O_3, N_2O), volatile organic compounds - VOCs (toluene, benzene, naphthalene, phenols, xylenes), industrial dyes (methylene blue, methylene orange, malachite green, methyl red), heavy metals (Pb, Cu, As, Cr, Sb, Hg, Mn, Cd), and PPCPs [48]. One of the scenarios that contribute to the increasing release of these contaminants into the atmosphere is the growing worldwide demand for energy.

3.2 Contamination by organic materials

The contamination of soil and water with organic materials such as oils, solvents, adsorbable halogenated organic compounds (AOX), volatile organic compounds (VOC), and industrial dyes is also a current problem that has caused great mobilization worldwide, mainly due to recent accidents in the Gulf of Mexico (2010) and the coast of Northeast Brazil (2019). Environmental crimes are also an important source of release of this waste, as occurred in the municipality of Joinville (SC) in 2012. At the time, the textile company Döhler polluted the river Cachoeira with industrial waste, dyeing the water red, as shown in Figure 3.2. As a result, the company was fined R$ 350 thousand for environmental crimes [49].

Figure 3.2: Photo of the river Cachoeira after water pollution with textile waste by the company Döhler [49].

One of the main concerns related to contamination with organic materials is the enormous amount in which they are present in our daily lives and their toxicity. One of its main sources that are considered critical nowadays are the industrial dyes. Usually formed by chromophore groups such as azo (-N=N-), carbonyl (-C=O), and nitro (-N=O), these organic compounds have a very characteristic color and even in small amounts they can already color the water. Moreover, they restrict the entry of light and compromise the photosynthesis of algae and phytoplankton, which decreases oxygen levels in the water and unbalances the whole aquatic ecosystem. The main responsible for the incorrect disposal of these materials in the ecosystem is the textile industry. In India, around 80% of the national production of dyes is consumed by this branch [50]. In the Indian district of Jaipur, there are more than 300 industries related to this segment and which release a large amount of toxic waste without treatment in the environment. A study using *Salmonella* bacteria showed that the surface waters of the *Amani Shah Ka Nallah* River contained high amounts of mutagenic compounds,which is a considerable risk for the population living nearby [51]. One of the most commonly used dyes in the textile industry is methylene blue (MB). Its structural formula can be seen in Figure 3.3. Due to its two aromatic rings and the unpaired electrons from N and S, MB possess a well-established adsorption band in the visible region related to HOMO-LUMO π-π* transitions – with maximum absorbance at λ = 664 nm [52].

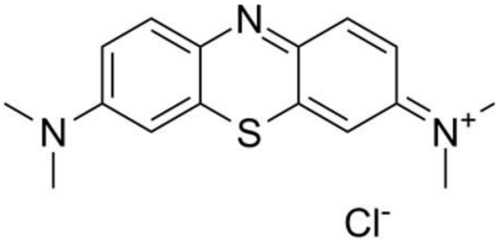

Figure 3.3: Structural formula of Methylene Blue.

3.3 Contamination by pharmaceutical and personal care products

PPCPs are another class of pollutants that have been increasingly mentioned in the literature. Some of the compounds most found in the environment are synthetic aromas, antibiotics, NSAIDs, analgesics, antidepressants, antiseptics, and steroids. They are present in quantities comparable to other contaminants such as pesticides and organic materials. However, the concern about the residues of these materials and their consequences for human health and the ecosystem is relatively new [53–56]. The main ways of improper disposal of these contaminants are the pharmaceutical industries and urban and agricultural sewage. Most of the drugs that are out of date or not fully used are disposed of incorrectly by the population. Antibiotics, for example, are already found in large quantities in surface water, underground, sewage network, and even in the water for human consumption. Studies prove that, in these concentrations, they contribute to the natural selection of increasingly resistant bacteria [47,53,57]. On the other hand, NSAIDs are one of the most common drugs used across the world, and they are easily founded in sewage treatment plants and surface waters [58].

In the pharmaceutical industry, water is widely used in the processing and even in drug formulation. The aqueous residues produced by these companies on chemical synthesis and fermentation processes are, in great part, rich in acids, bases, organic products, solvents, metallic salts, nitrates, and phosphates. They are residues of great toxicity, generally showing high chemical and biochemical oxygen demands (COD and BOD), and high concentration of total suspended solids (TSS) [47]. Another factor that potentiates the negative effect of PPCPs is their considerable capacity to bioaccumulate. Hydrophobic PPCPs, for example, are known for their high persistence in different ecosystems and low biodegradability. On the other hand, the hydrophilic PPCPs are easily dispersed in water courses, which facilitates their interaction with different aquatic organisms and directly interferes with the metabolism of these species [55,57]. Thus, the incorrect disposal of these materials in landfills, sewers or even septic tanks is a significant source of contamination. In the rainy season, these compounds are easily carried through the soil, contaminating the groundwater and other sources of underground water. In addition to the immediate impact that this type of contamination can cause, it is necessary to consider the chronic effect of these pollutants on different ecosystems. For this reason, their toxicity is difficult to be completely measured [55].

Therefore, the study of the removal and degradation of these contaminants in an aqueous environment is critical in the maintenance, recovery, and development of healthy environments that are suitable to marine and terrestrial life. Moreover, products for human consumption are not free of the dangers caused by toxic materials. The different means of water pollution, atmosphere, and soil contribute to an emergency on a global scale, either by the direct effect on completely devastated ecosystems, or by the stochastic and chronic effect that can cause, for example, soil infertility, genetic mutations, and fertility problems among different species. These systems are completely interconnected, and thus, influence each other. For this reason, anthropogenic environmental contamination is a problem on a global scale that demands new materials with great mineralization properties to remove these pollutants.

3.3.1 Non-steroidal anti-inflammatory drugs: IBP and DIC

One of the most common NSAIDs founded in water courses are IBP and DIC. They have beenwidely applied for human and veterinary use and can be obtained without a recipe in many countries. Their incorrect disposal and their residues in human and animal urine contribute to the spread of these contaminants into the environment [58]. IBP, for example, is suspected to influence sex steroid hormones through steroidogenic pathways in different aqueous species [59]. Moreover, a decrease in reproduction was observed in crustaceans and fishes after DIC exposure [60]. These drugs are not easily degraded by conventional wastewater treatment plants, which increases the necessity of developing new methods for their removal [61]. For these reasons, studies about their degradation are being carried out throughout the world [61–68].

IBP and DIC are commonly used for the treatment of pain, fever, and inflammation. They can be easily founded in drugstores worldwide, and their structural formula can be seen in Figure 3.4. IBU and DIC are slightly soluble in water and have high persistence in the aquatic environment [69].

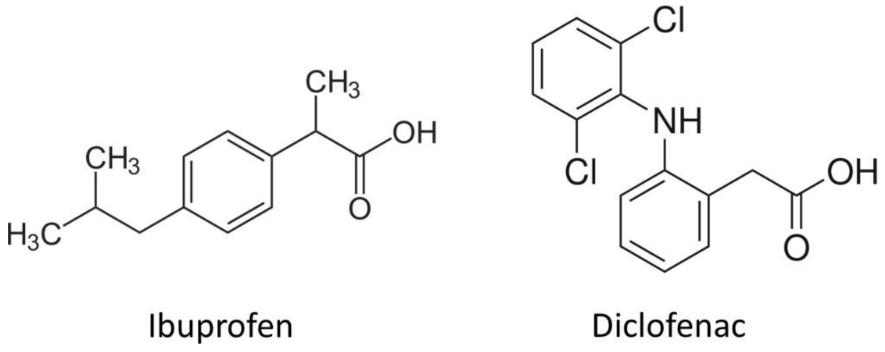

Figure 3.4: Structural formula of Ibuprofen and Diclofenac.

3.4 Methods to remove contaminants

Several methods are reported in the literature for the removal of PPCPs and organic materials. However, some aspects must be considered for it to be accepted as efficient and advantageous over others. It is worth mentioning price, complexity, selectivity, toxicity, and the possibility of reusing the materials as key factors that directly interfere in their applications. Following this reasoning, the methods that are most indicated for the capture and removal of a wide range of pollutants are adsorption and photocatalysis [50,53,70,71]. Table 3.1 shows some of the main ways of decontamination of aqueous solutions.

Table 3.1: Main methods to remove organic materials and PPCPs.

Contaminant	Main removal methods	References
Organic materials	Electrochemical treatments, photocatalysis, coagulation, flocculation, ion exchange, irradiation, ozonation, Fenton process, adsorption, filtration, biodegradation, enzymatic degradation, photocatalysis, hybrid technologies.	[50,71–76]
PPCPs	Electrochemical treatments, ozonation, reverse osmosis, Fenton process, photocatalysis, adsorption, sedimentation, flotation, nanofiltration, biodegradation, volatilization, hybrid technologies.	[47,53,54,57]

3.4.1 Adsorption processes

The process of adsorption and desorption of substances is a physical-chemical phenomenon that occurs on solid particles' surface from the interaction between adsorbate and adsorbent. They are often divided into two groups: chemisorption and physisorption. The former occurs preferentially at higher temperatures, it is formed by covalent and ionic chemical bonds, has high specificity and activation energy, it is characterized by the formation of a single layer and its desorption is very hard. The last occursat milder temperatures, is formed by London-Van der Walls forces, has lower specificity and activation energy, and it can form multilayers, which makes the desorption easier. However, both processes can also coexist [77,78].

Adsorption poses a significant advantage over other techniques because of its simplicity and for being a low-cost procedure. Studies show the use of activated carbons for the adsorption of IBP and DIC, and it is also considered one of the most common processes to remove industrial dyes from wastewater [69,79]. However, adsorption processes also present some disadvantages as, for example, the possibility or not of desorption, the reusability of the adsorbent, the necessity of post-treatment for removing the contaminant, and the possible need to discard the adsorbent after a few cycles [80,81]. Thus, heterogeneous photocatalysiscan be an improvement when combined with adsorption methods.

3.4.2 Photocatalysis

Photocatalysis is a term used to describe the acceleration of a chemical reaction induced by light in the presence of a catalyst. It can be divided into two major groups: homogeneous photocatalysis and heterogeneous photocatalysis [82,83]. Only from the 70's on heterogeneous photocatalysis started to be widely developed and, since then, the dispersion of solid semiconductors in liquid or gaseous mixtures has been widely studied. This type of system influences the chemical reactivity of several substances, promoting chemical reactions of reduction, oxidation, isomerization, substitution, and polymerization; all of them induced by the presence of light [82,84]. Among the enormous possibilities presented, the oxidative photodegradation with the aid of semiconductors proved to be an efficient route in mineralizing toxic and biologically persistent organic materials. In this case, the pollutants are oxidized in compounds such as CO_2, H_2O, NO_3^-, or in other oxides, phosphates, sulfates, and halides. This method of degradation of pollutants offers several advantages over others (e.g., ozonation, chlorination, adsorption), because it does not use materials strongly oxidizing or toxic, does not generate solid waste or pollute the atmosphere [84,85].

Figure 3.5 shows the positions of the valence band (VB) and conduction band (CB) for different semiconductor materials, besides their electrical potential in front of the standard hydrogen electrode at pH = 1 (NHE - Normal Hydrogen Electrode). It is worth mentioning that TiO_2 has a band gap that contemplates the redox reactions of the water [84–86].

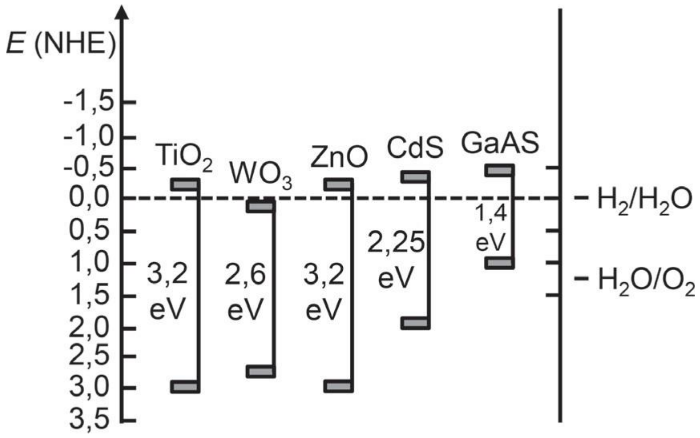

Figure 3.5: Diagram illustrating the position of the valence and conduction bands for different semiconductor materials, relating them to the potential of the standard hydrogen electrode (NHE) at pH = 1. The band gap of each material is supplied in eV. The redox reactions of water decomposition in oxygen and hydrogen are also illustrated for comparative purposes [86].

When light falls on a semiconductor, photons that have energy greater than or equal to the band gap of that material can excite electrons from VB to CB, according to Equation (3.1).

$$h\nu \geq E_{gap} \tag{3.1}$$

In this process, when an electron (e^-) jumps into the conduction band, it leaves a hole in the valence band, which is considered a positive charge (h^+). In the case of oxidative photodegradation, several reactions may occur, as schematically represented in Figure 3.6. The radical OH• is extremely oxidizing (E^o = 2.4) and is considered one of the most important in the mineralization of organic compounds. However, other reactive species can also be formed, worth mentioning: $O_2\cdot$, $HO_2\cdot$, H_2O_2, HO_2^-, OH^- [85,87,88].

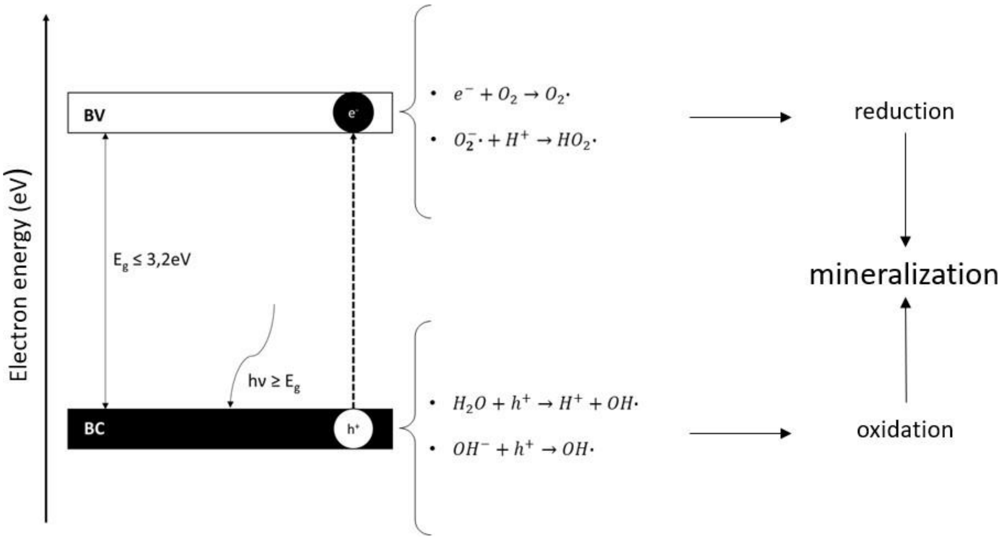

Figure 3.6: Scheme of photodegradation of pollutants in the presence of a semiconductor and some of the main chemical reactions. Adapted from MILLS *et al.* [85].

Spontaneous recombination of electrons and holes, also known as charge carriers, should be avoided in photocatalytic processes. These entities, which can be formed both inside and on the surface of the semiconductor, can annihilate themselves by recombining due to electrostatic interactions [87]. Moreover, electrons and holes have a defined lifetime, related to the probability of reacting with some component of the medium before finding the species of interest. Thus, recombination tends to occur mainly in the bulk of the material but also occur on its surface [85]. When they recombine, two photons with total energy hv are released, according to Equation (3.2). Obviously, when this occurs, the entities lose their potential to oxidize and reduce other species, harming the photocatalytic process.

$$h^+ + e^- \rightarrow hv \tag{3.2}$$

To avoid this scenario, materials are inserted into the system to trap the produced electrons, the holes, or both. In some cases, the presence of oxygen or extremely oxidizing species such as peroxides and periodates helps in the trapping of electrons in the conduction band, which prevents the process of recombination [84].

It is worth mentioning that the phenomena of adsorption and photocatalysis correlate. In practice, as recombination is a phenomenon that should be avoided, the presence of adsorbed species gives a greater probability that the electrons and holes generated can reach the surface and react with the pollutant before being extinguished. Materials such as MOFs, graphene oxides, Pt, Pd, and Au nanoparticles can trap these entities. Thus, the use of composites that present, at the same time, high SSA and good photocatalytic behavior is an advantageous alternative for the degradation of pollutants [84,89–91].

3.5 Metal-Organic Frameworks - MOFs

MOFs, initially called coordination polymers, are a relatively new class of hybrid materials, which are composed of inorganic clusters connected by organic binders, giving rise to highly organized and open crystalline networks. Their highly directional bonds can generate structures in the forms of chains, layers, and three-dimensional networks [68,69]. As there are no standards for the nomenclature of these compounds, they are commonly classified according to the institute or university where they were first synthesized. For example, HKUST-1 was developed at the Hong Kong University of Science and Technology, MIL-100 at the Materials Institute of Lavoisier, and UiO-66 at the University of Oslo (*Universitet i Oslo)*.

MOFs generally have high specific surface areas and can reach values of around 10,000 $m^2.g^{-1}$ [92]. In addition, they exhibit an ultra-porous nanocrystalline structure, which allows their application as adsorbents to remove contaminants in aqueous media, in the storage of gases such as H_2 and CO_2, and catalysis processes. They can also be chemically functionalized, which represents a great advantage of MOFs over other materials [21,22]. Therefore, these compounds have been extensively studied in recent years, as shown in Figure 3.7

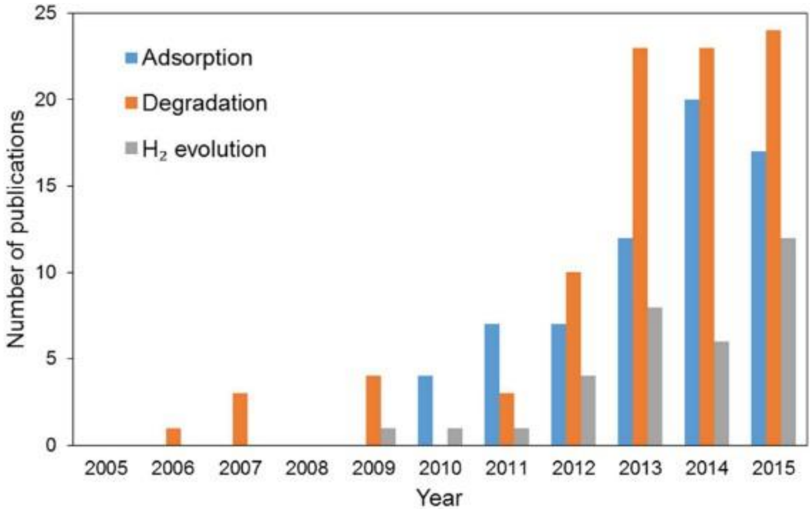

Figure 3.7: Number of publications on MOFs in recent years separated by themes: adsorption, degradation, and H_2 reduction [90].

3.5.1 Structure and synthesis of MOFs

The structure of MOFs can be described as a hybrid inorganic-organic network that resembles a classic inorganic solid. In both cases, their crystalline networks have a skeleton formed through the association of primary (PBU) and secondary (SBU) building units. They are basically units that repeat themselves to generate the crystalline structure of a solid. PBU are formed by clusters with a defined structural organization, such as what occurs with SiO_4 and AlO_4 tetrahedrons in zeolites, for example. SBU are basically the repetition of these structures in larger organizations, as shown in Figure 3.8 [93,94].

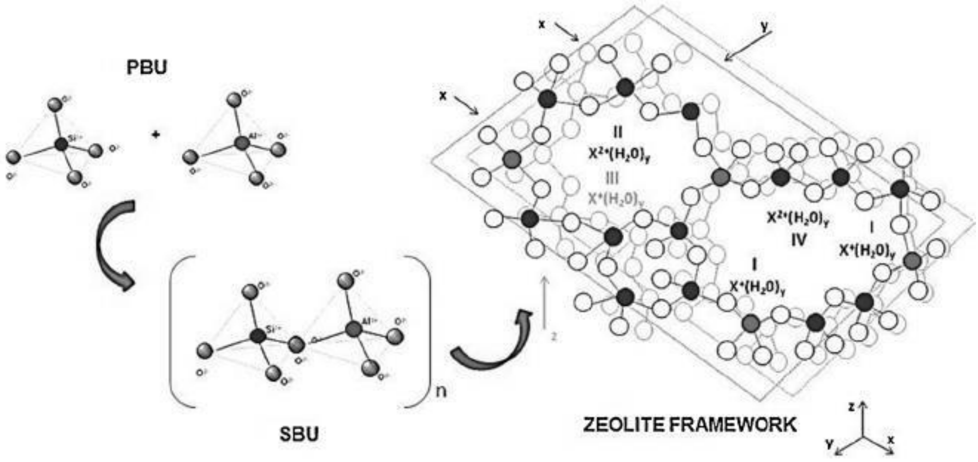

Figure 3.8: Formation of zeolites by organizing primary building units of AlO_4 and SiO_4 into secondary building units, thus forming their crystalline structure [93].

The main difference between zeolites and MOFs is their SBU. In the case of zeolites, they present only inorganic parts (e.g., sulfates, phosphates) associated with metallic ions in coordination numbers of 4, 5, or 6. In MOFs, SBU present organic binders instead of inorganic species, as can be seen in Figure 3.9 [20]. The organization of MOFs' structures, as well as the possibility of modulation through the combination of different metals and organic binders, resulted in the mistaken classification of these materials as coordination polymers. Despite presenting several similar characteristics with the polymers, such as an enormous range of architectural possibilities, topology, size, shape, and rigidity, the metal-organic frameworks can present higher thermal stability than these materials. In addition, their pores maintain their dimensions and are permanent as long as the structure of the MOF remains stable, unlike polymers [20,94].

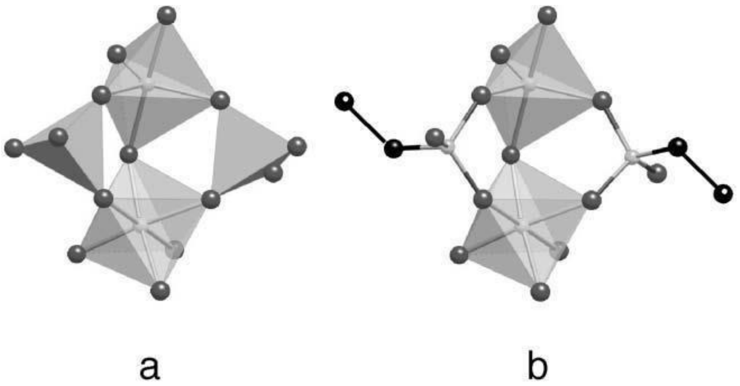

Figure 3.9: Structural scheme of (a) SBU of a porous inorganic solid and (b) SBU of a porous hybrid solid that presents organic binders [20].

In 2010, two different studies were published in the Journal of Solid-State Chemistry, mentioning that some MOFs structures corresponded to extended versions of simpler structures such as diamonds and sodalites [95,96]. From that moment on, it was possible to perform simulations and predict the formation of these crystalline networks, considering the selection of PBU, their spatial organization, unit cell parameters, atomic positions, and the minimum organizational energy point for possible combinations. In addition, the structure and properties of the MOFs can also be influenced by synthesis parameters such as pH, pressure, solvent, reaction time, and temperature [20,23,94–96]. The main characteristics of these materials are undoubtedly their large SSA and the presence of permanent porosity. Thus, the study of methods that allow altering these characteristics without changing the fundamental structure of metal-organic frameworks is of extreme importance. Among these routes, two are well known for allowing to function the structure of the MOFs and change the size and shape of their pores:

a) Isoreticular expansion (IE): this process allows controlling the pore size of metal-organic frameworks by varying the organic binder introduced during the synthesis of the network [23,24].

b) Post-synthetic modification (PSM): it is a way to modify the metal-organic framework, either by replacing organic linkers, inorganic cluster atoms, or by functionalizing its surface. It is performed after the synthesis of the solid [23,97,98].

The IE process, despite modifying the pore size of the material, does not alter the isoreticular nature of the MOF structure. For example, NU-1101 is one of the best examples of structure expansion in Zr-based MOFs. It is produced with the organic binder Py-XP^{4-}. When this binder is replaced by a larger one, like Py-PTP^{4-}, the metal-organic framework formed is isoreticular to that of NU-1101, but with larger pores and a larger SSA, as shown in Figure 3.10. Only by varying the binder used in the synthesis of MOF it was possible to change the specific surface area from 4422 $m^2.g^{-1}$ to 5290 $m^2.g^{-1}$, which demonstrates the importance of the method to increase the efficiency of these compounds in certain applications [24]. The PSM method has the advantage of enabling the manufacture of structures that could not be obtained by other direct routes [23,97]. A good example occurs, again, in Zr-based MOFs. This family of metal-organic frameworks has been widely studied for this type of modification due to its high stability in more aggressive chemical environments such as acid and basic media [98]. *Volkringer et al.* showed that Zr-based MOFs remain stable even under gamma irradiation [99]. The modification of UiO-66(Zr) through the substitutionof Zr atoms by Ti or Hf generates organometallic nets with a mixture of different clusters, as shown in Figure 3.11 [97].

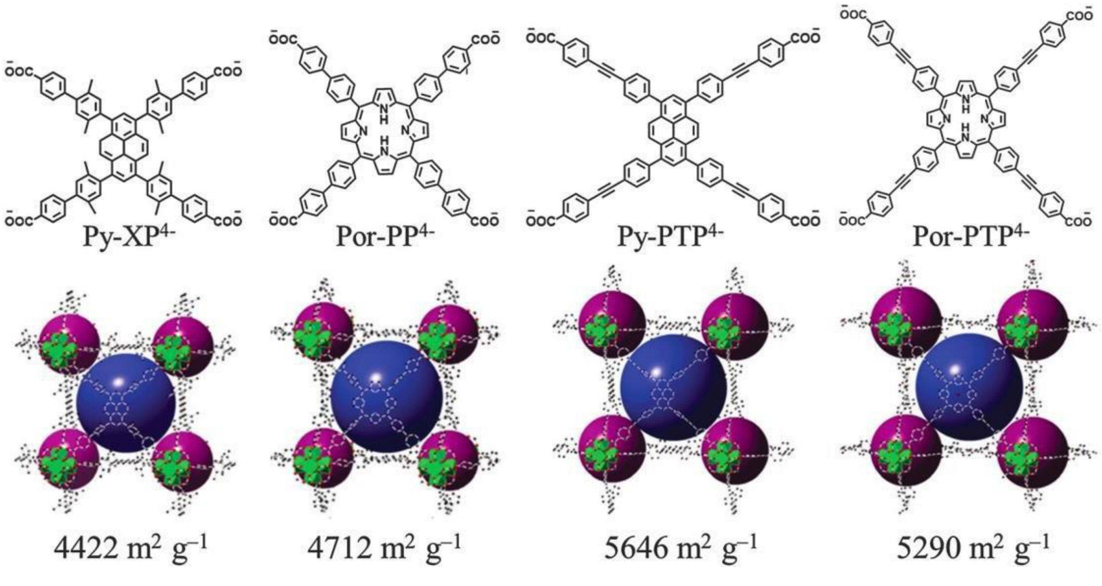

Figure 3.10: Schematic showing the influence of Py-XP^{4-}, Por-PP^{4-}, Py-PTP^{4-}, and Por-PTP^{4-} (top) tetraded binders used in the construction of the metal-organic frameworks NU-1101, NU-1102, NU-1103, and NU-1104, respectively (below). In this case, each respective SBU of the MOFs represented has two types of pores: a larger one, formed by the space between the binders (in blue), and four smaller ones, formed by the space between the inorganic clusters (in purple). The inorganic clusters are represented in green [24].

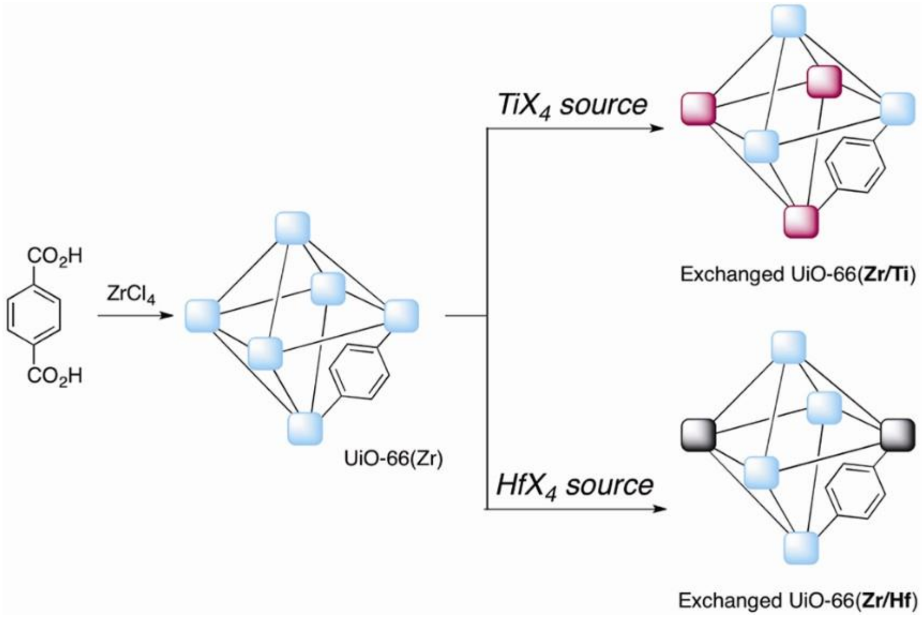

Figure 3.11: UiO-66(Zr) and its later PSM synthesis scheme by replacing Zr ions with Ti or Hf ions [97].

3.5.2 Adsorption and degradation of pollutants through MOFs

MOFs presents countless applications in the removal of environmental contaminants. Several studies mention the electrostatic interaction between adsorbent and adsorbate, the coordinated unsaturated sites (CUS), and the breathing properties of MOFs as main factors for their efficiency in the removal of various pollutants [48,100]. Some of them act with great efficiency to remove these toxic species from the environment without any kind of structural or chemical modification. An example is the MIL-100(Fe), which showed an excellent adsorption capacity in the removal of the malachite green dye, due to the presence of CUS, which causes the metal to interact strongly with the dye [101]. In other applications, it is extremely interesting to alter some characteristics of these materials, most of the time superficial, to achieve a considerable degradation rate [17,102].

In this way, several compounds can be incorporated into metal-organic frameworks to alter their chemical and structural properties. Functional groups (e.g., amino, thiol, hydroxyl), metals, oxides, and nanoparticles, are some examples of species that can be inserted into the structure of MOFs. In the case of adsorption and photocatalysis processes, these species can alter the selectivity, efficiency, and kinetics of the reactions. A good example is the functionalization of HKUST-1 with thiol for the removal of Hg^{2+}. Studies have shown that pure HKUST-1 is not able to adsorb the metal, while Tiol@HKUST-1 adsorbs about 714 $mg.g^{-1}$ [103]. This affinity can be explained by the fact that mercury is considered a weak Lewis acid due to its high polarizability. It therefore forms strong covalent bonds with weak Lewis bases, such as reduced sulfur [104].

Photocatalytic semiconductor materials also represent a relevant alternative for the degradation of pollutants, due to their low toxicity and cost. Among these materials, titanium (TiO_2) and zinc oxide (ZnO) can be mentioned [105,106]· However, one of the main difficulties associated with the use of these compounds is their tendency to agglomeration, attributed to a small particle size and low adsorption capacity. To overcome these limitations, several studies have focused on the incorporation of nanoparticles of these semiconductors in materials with high specific surface areas [26].

This range of structural possibilities presented by MOFs, combined with their great capacity for adsorption and stability in water, make them promising candidates for modification with ceramic nanoparticles [94]. There are different strategies used in the literature to modify these compounds, worth mentioning:

- The preparation of a coating of MOF particles on a surface of semiconductor material [27];

- The formation of a semiconductor material shell on a MOF nucleus, forming a core-shell structure [29,107];

- Combining hydrothermal synthesis of MOF and semiconductor material [108];

- PSM route: traditional sol-gel process [109];

- PSM route: sol-gel process without the presence of acid catalyst [30].
- PSM ligand exchange [97].

3.6 The sol-gel synthesis of TiO_2

In this work, the PSM sol-gel route without the presence of acid [30] was chosen due to the low stability of HKUST-1 and MIL-100(Al) over acid media [37,38]. Titanium dioxide, or titania (TiO_2), was chosen as the semiconductor material due to its low toxicity, low cost, elevate chemical and thermal stability, and high photocatalytic activity over organic materials [33]. Moreover, it is the semiconductor most used in the field of photocatalysis, presenting three main polymorphic phases: rutile, anatase, and brookite. Among these, the last one is considered unstable in ambient temperatures and pressures, which makes most of its photocatalytic applications impossible [33]. The other two phases are thermodynamically stable and anatase presents the best photocatalytic behavior due to its higher adsorption capacity, smaller particle size, and larger specific surface area than rutile, despite having a higher band gap (3.20 eV against 3.03 eV of rutile) [110]. Studies show that mixtures of rutile and anatase can be more photoactive than each of them separately [31].

This team has know-how on the sol-gel synthesis of TiO_2 samples with great improvements over its properties, already achieving higher photoactivity than the commercial titania Degussa P25 [31]. The structure and SSA of TiO_2 strongly affect its photocatalytic activity and the use of nanocrystalline TiO_2 poses major challenges regarding its poor adsorption capacity related to its non-porous structure, and the tendency of agglomeration upon suspension systems due to its low particle size [26,111]. These challenges can be overcome by using a sol-gel route combined with hydrothermal treatment in the presence of a MOF powder. In this case, MOF’s framework acts as a porous matrix for TiO_2 to grow inside, which creates a composite material that presents both high SSA and high photocatalytic activity [29]. Moreover, the transference of photogenerated electrons to other materials can act as an electron trap and increase the half-life time of the electron-hole entities, reducing the recombination rate of charge carries in the semiconductor [33].

Another advantage of anatase is the wide variety of synthesis routes that available, which can result in diverse structures with different properties, especially concerning their SSA and particle size. Studies carried out at UFMG showed that other factors directly influence the size of the formed crystals, such as the type of solvent used during the synthesis of titania, for example [31]. By combining the sol-gel route of TiO_2 with the MOF matrix, a high photocatalytic and porous material is to be produced. Therefore, the insertion of TiO_2 in MOFs' porous structure is of great interest, which highlights the importance of this work.

4 MATERIALS AND METHODS

During this work, metal-organic frameworks were produced at the Unity of Catalysis and Solid Chemistry (*Unité de Catalyse et Chimie du Solide* – UCCS), department of the University of Lille (*Université de Lille* - ULille) in France. Briefly, the hydrothermal synthesis of the MOFs consists of a mixture of the metal precursor, the linker, the modulator, and the solvent in a Teflon bottle inserted inside a stainless-steel autoclave, which is further heated in an oven for a determined time. After that, the product is washed to remove the excess of ligand and/or modulator and is activated in order to remove any free solvent within its porous structure. The conditions of their synthesis are schematizedin Table 4.1 and their structures are illustrated in Figure 4.1 and Figure 4.2.

Table 4.1: Composition of inorganic cluster and organic binder for different metal-organic frameworks

MOF	Metal Precursor	Linker	Modulator	Solvent	Washed	Heating conditions	Activation conditions
HKUST-1	$Cu(NO_3)_2.3 H_2O$	trimethyl-1-3-5-trimesate		EtOH + H_2O	EtOH	110 °C for 12h	70 °C for 1h then 110 °C for 2h
MIL-100(Al)	$Al(NO_3)_3.9 H_2O$	trimethyl-1-3-5-trimesate	HNO_3, 1M	H_2O	DMF	180 °C for 3h	200 °C for 5h

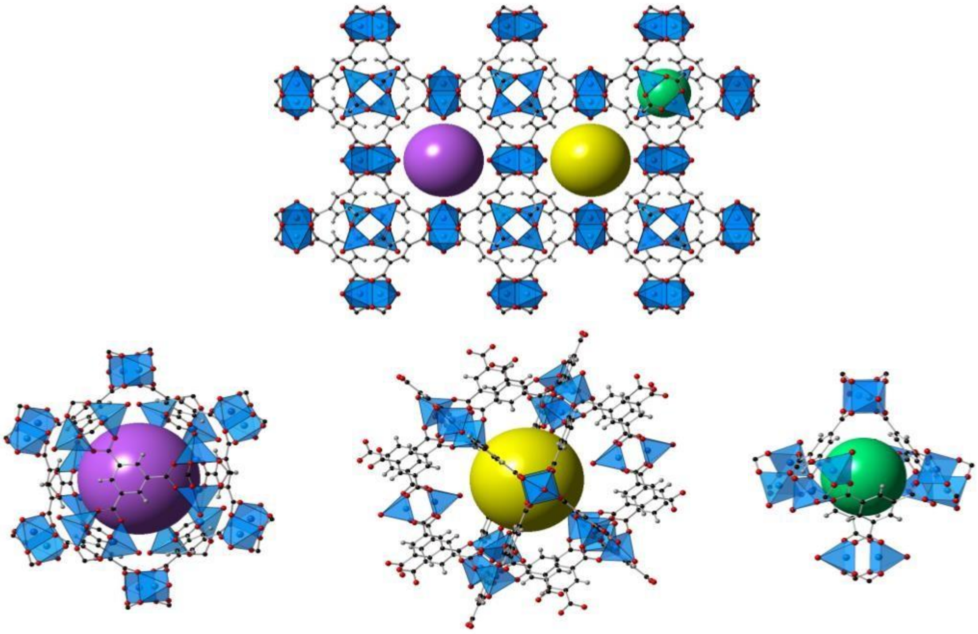

Figure 4.1: HKUST-1 structure. In blue: the metal cluster, in red: oxygen atoms, in black: carbon atoms, in grey: hydrogen atoms. The smallest cavity is represented in green and has a 0.5 nm diameter, followed by yellow with 1.1 nm and purple with 1.4 nm. The entering windows contain approximately 0.6 nm.

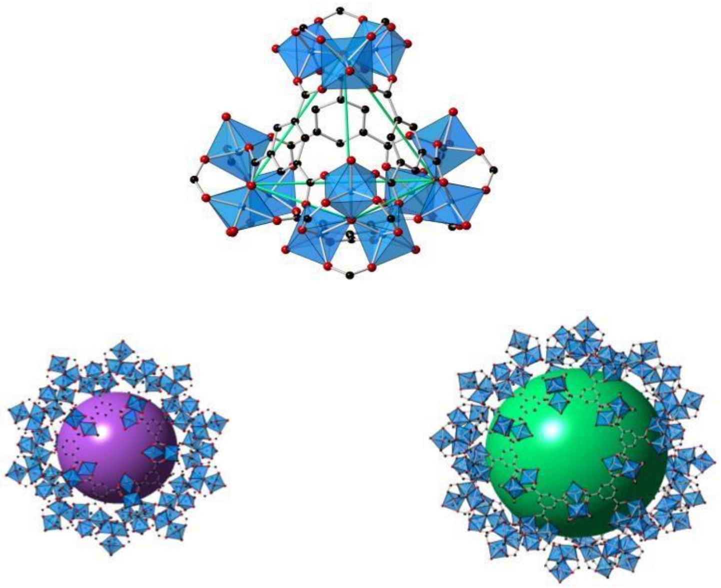

Figure 4.2: MIL-100(Al) structure. In blue: the metal cluster, in red: oxygen atoms, in black: carbon atoms. The smallest cavity is represented in purple with a 2.5 nm diameter and the largest in green with 2.9 nm. The entering window contains approximately 0.9 nm.

4.1 Overview of MOFs

MOFs were produced following routes mentioned in the literature [17]. All were produced in hydrothermal reactors, under autogenous pressure. The procedure is described below:

HKUST-1 was hydrothermally prepared as well. Copper(II) nitrate trihydrate ($Cu(NO_3)_2.3H_2O$, Aldrich, 99%, 3.5 g), 1,3,5-benzenetricarboxylic acid ($(COOH)_3C_6H_3$, Sigma Aldrich, 98%, 2.1 g), EtOH (36 mL), and H_2O (36 mL) were poured in a 500 mL Teflon container and then placed in a furnace. It was then heat-treated in air at 110 °C for 12 h using a heating rate of around 1.4 $°C.min^{-1}$. After reaching room temperature, a dark blue solid was recovered by centrifugation, washed with EtOH, and subsequently air-calcined at 70 ºC for 1 h and then at 110 °C for 2 h. This procedure gave rise to about 2.5 g of dried solid material.

MIL-100(Al) was prepared by hydrothermal treatment as follows. Aluminum nitrate nonahydrate ($Al(NO_3)_3.9H_2O$, Carlo Erba, 99%, 7.48 g), trimethyl-1-3-5-benzenetricarboxylate ($(CH_3COO)_3$-C_6H_3, Aldrich, 98%, 3.39 g), nitric acid solution (HNO_3, Aldrich, 1M, 25 mL) and deionized water (H_2O, 91 mL) were initially poured in a 500 mL Teflon flask. The container was transferred to a stainless-steel autoclave and then placed in a furnace. It was subsequently heat-treated in air at 180 °C for 3 h at a heating rate of about 2.6 $°C.min^{-1}$. Next, the autoclave was allowed to cool down to room temperature inside the furnace. A yellow solid was then recovered by centrifugation and stirred with 200 mL of anhydrous N,N-dimethylformamide ($(CH_3)_2NCH$, Aldrich, 99.8%) at 150 °C for 5 h. The solid was collected by centrifugation, washed with absolute ethanol (EtOH, Aldrich), and then calcined in air at 200 °C for 5 h. Around 2.3 g of dried solid was collected after this step.

4.2 MOFs functionalization with TiO_2

For the incorporation of TiO_2, a PSM sol-gel route without the presence of acid was adapted [30]. The proposed route can be described as follows. Initially, 500 mg of the prepared MOFs was dried under air at 150 °C for at least 5 h. Next, it was added under stirring to a solution containing 20 mL of titanium (IV) tetraisopropoxide (TITP, Sigma Aldrich 98%) and 26 mL of isopropyl alcohol (IPrOH, Aldrich, 98%). The solution was sonicated for 30 min and kept under stirring for another 30 min. After 10 h, the solid was recovered by centrifugation at 6,000 rpm for 20 min and washed with IPrOH. It was subsequently aged for 48 h in air and then poured in a 350 mL Teflon container previously filled with 210 mL of deionized Milli-Q water. The system was transferred to a stainless-steel autoclave and heated at 150 °C for 10 h. After cooling down to room temperature, the solid was recovered by centrifugation (20 min at 6,000 rpm) and then air-dried at 80 °C for 72 h. The samples modified with titania were identified as TiO_2@MIL-100 and TiO_2@Cu-btc. The former did not present any changes in its color after the functionalization with TiO_2, while the latter became light blue. Figure 4.3 presents photographs of the materials synthesized in this work.

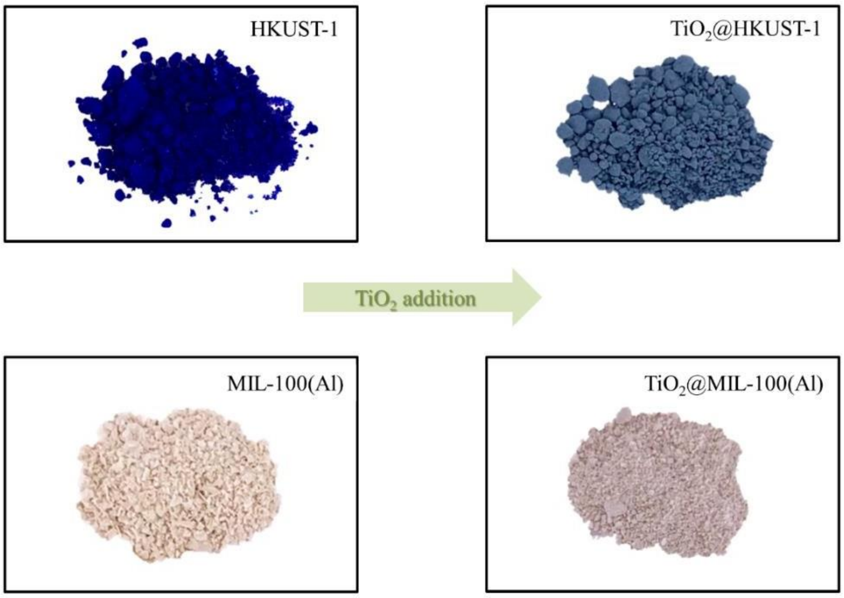

Figure 4.3: Photographs of the materials synthesized in this work.

4.3 Characterization of MOFs

XRD was conducted on a Philips-PANalytical diffractometer (PW1710) at a step rate of 0.06°.s^{-1}, using CuKα as the radiation source (λ = 1.54 Å). N_2 and Kr sorption were performed at the liquid nitrogen temperature (-196 °C) using a Micromeritics ASAP 2020 apparatus using samples previously degassed under vacuum at 105 °C for copper trimesate and at 200 °C for MIL-100(Al). The specific surface area (SSA) and pore size distribution of the examined samples were evaluated by the multipoint BET (Brunauer–Emmett–Teller) model and density functional theory (DFT). TEM, SAED, EDS, and EELS were conducted on an FEI microscope (Tecnai G2-20 SuperTwin) at an accelerating voltage of 200 kV. This microscope is equipped with a Si(Li) EDS detector (EDAX) with a 30 mm^2 window and a post-column Gatan Image Filter (GIF) Quantum SE System coupled with a bright and annular dark field (BF/ADF) STEM detector, Orius SC200 and GIF (US1000FTXP) CCD cameras. The samples used in these tests were previously dispersed in EtOH and sonicated for 5 min at room temperature. The obtained suspensions were dripped on carbon-coated grids. After drying in air at room temperature, those grids were used in TEM, EELS, EDS, and SAED examinations. SEM was conducted on a FEG microscope (Hitachi SU 5000) at an accelerating voltage of 5 kV, using samples previously sputter-coated with carbon. This microscope is equipped with a Si(Li) EDS detector (AZtec from Oxford Instruments) with a 60 mm^2 window.

The apparent bandgap energy (E_{gap}) of the materials obtained in this study was evaluated by UV-Vis diffuse reflectance spectroscopy at a resolution of 1 cm^{-1} on a Shimadzu UV-2600 spectrometer. The Kubelka-Munk method was applied following a methodology recommended elsewhere [112]. FTIR was performed on a Bruker Alpha spectrometer using an attenuated total reflectance (ATR) accessory and a diamond crystal as the reflective element. The spectra were taken at a resolution of 4 cm^{-1} and 128 scans. Raman spectroscopy was carried out on a LabRaman HR-Evolution (Horiba Scientific) micro-spectrometer equipped with 600 lines per mm grating and an Olympus objective. A 515 nm laser was used as excitation source. The thermogravimetric (TG) experiments were carried out on a thermoanalyzer TGA 92 Setaram in air at a heating rate of 5 °C.min^{-1} from room temperature to 800 °C. DTG (differential thermogravimetry) profiles were obtained by calculating the first derivative of the collected thermograms. Spin trapping EPR was carried out at room temperature on an X-band (≈ 9.4 GHz) Magnettech MiniScope MS400 spectrometer. This technique allows examining short-lived free radicals, particularly reactive oxygen species (ROS). The experimental parameters used in these tests were: microwave power = 10 mW, modulation field = 100 kHz, modulation amplitude = 0.2 mT, center field = 337 mT, scan time = 60 s, and number of integration points = 4096. Aqueous solutions of IBP (10 mg.L^{-1}) and the examined photocatalyst (200 mg.L^{-1}) were initially prepared at room temperature. Solutions containing either N-tert-butyl-α-phenylnitrone (PBN, TCI America – Japan, 98%) or 5,5-dimethyl-1-pyrroline N-oxide (DMPO, Oakwood – USA, 96%) were used as spin traps in these tests. The loading of PBN and DMPO in these solutions was kept at about 200 and 100 mM, respectively. In the case of PBN, the solvent was a mixture of absolute ethanol and water in a molar ratio of 1:1, while the DMPO solution contained only water. The as-prepared solutions were subsequently illuminated with UVA light (375 nm) using a 16 mW defocused laser source. Aliquots of the supernatant of about 50 μL were collected at different times from these solutions and poured into glass capillaries for examination.

4.4 Adsorption and photocatalysis tests

The photocatalytic performance of the prepared samples was verified by evaluating the photodegradation rate of IBP (Florien Pharmaceutical Supplies – Brazil) and DIC (Henan Dongtai Pharmacy Limited Company – China) standards. These drugs were initially dissolved in distilled water at room temperature under stirring. The concentrations of the drugs and photocatalysts in the as-prepared solution were 10 and 200 mg.L^{-1}, respectively. The initial pH of the solutions was about 8. Next, the solution was poured into a photoreactor containing an Osram Dulux 9W/78 UVA lamp (1.5 W between 315 and 400 nm). The solution temperature was kept constant at 25 °C using a cooling system coupled to the reactor. It was initially kept under stirring at room temperature in the dark for 12 h for adsorption purposes. Next, the UVA lamp was turned on, and aliquots of the solution were taken as a function of time and used to monitor IBP and DIC concentrations. The aliquots were initially centrifuged at 6,000 rpm for 5 min to avoid interference from suspended particles. The particle-free supernatant was then transferred to quartz cuvettes and examined by UV-Vis spectroscopy using the spectrometer mentioned before. The light absorption at 222 and 276 nm were used as references for IBP and DIC, respectively. Photolysis tests (photodegradation in the absence of a photocatalyst) were also conducted for reference purposes. It was observed that IBP and DIC did not degrade under UVA lighting to such an extent that their photolysis can be neglected.

MB was used as a preliminary contaminant in these tests since the mechanisms of photodegradation of organic compounds that present orbital π are similar. Besides, MB is relatively cheap, easy to access, and has low toxicity. Initially, standard solutions of distilled water and MB were prepared in concentrations of 0, 5, 10, 15, and 20 mg.L^{-1}, to elaborate a calibration curve and to obtain the correlation between its concentration the absorbance values measured in a UV-Vis spectrometer; in this case was possible to achieve a correlation factor between the absorbance and concentration values of $R^2 = 0{,}9908$ – the data was collected with $\lambda = 664$ nm, which corresponds to the higher absorbance of MB in the UV-vis region. In this case, the test followed a different procedure. It is worth mentioning that adsorption tests were previously conducted with aliquots collected in every 10 minutes for 2 hours, to evaluate the amount of time that the mixture takes to achieve adsorption equilibrium. Considering this, the mixture stood in the dark for 60 minutes, and then the light was turned on for 5 hours. Aliquots were collected from time to time, centrifugated, and then measured on the UV-vis spectrometer.

A photo-reactor similar to the one shown in Figure 4.4 was used to study the adsorption capacity and photocatalytic activity in the degradation of MB, DIC, and IBP.

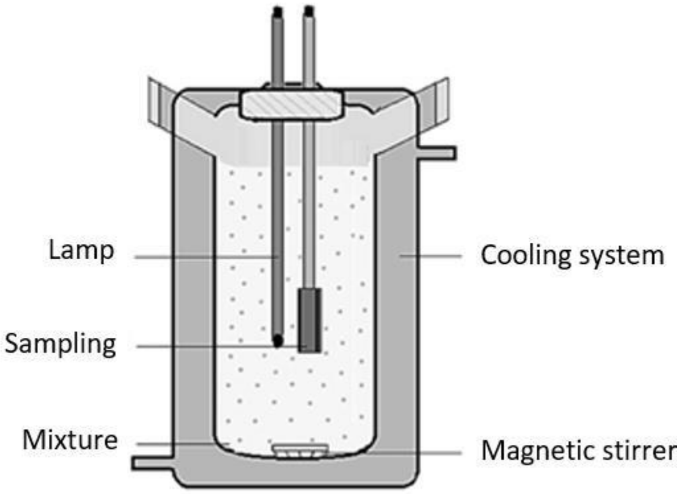

Figure 4.4: Schematic representation of a photo reactor similar to that used in this research. Adapted from DIAZ-URIBE *et al.* [113].

5 RESULTS AND DISCUSSION

5.1 Structural characterization

Figure 5.1 shows XRD patterns obtained in this work. Diffraction lines of MIL-100(Al) were observed at 2θ about 3.6°, 4.2°, 5.1°, 6.1°, and 6.5°, which have been associated with the (220), (311), (400), (442) and (333) crystal planes [35,114]. After incorporating TiO_2 into the MOF, additional diffraction lines related to anatase were also noticed at 2θ around 25.5°, 38.2°, 48.1°, and 54.4°, which are assigned to its (101), (004), (220), and (211) crystal planes [31]. The main diffraction peaks of HKUST-1 were observed at 2θ around 6.9°, 9.5°, 11.7°, 19.1°, and 26.1°, which are attributed to (200), (220), (222), (440), and (731) crystal planes [115]. The addition of TiO_2 in this MOF caused its main peaks at 9.5° and 11.7° to disappear while another crystal phase was observed (main peaks at about 9.0° and 10.0°). This new structure corresponds to $Cu_2(btc)(OH)(H_2O)$, formed after the collapse of HKUST-1 and hydrolysis of copper-oxygen bonds. Simultaneously, copper centers ($CuO_4(H_2O)$) arranged in paddlewheel units are replaced by infinite chains composed of square bipyramids $CuO_3(OH)_2$ and octahedra $CuO_4(OH)(H_2O)$ units. These reactions cause the release of H^+

ions into the solution, as described in Equation (1) [116]. For this reason, TiO_2/HKUST-1 composite was designated as TiO_2@Cu-btc, which is a non-porous copper trimesate phase.

$$2Cu_3(btc)_2 + 2H_2O \rightarrow 3Cu_2(btc)(OH)(H_2O) + btc^- + H^+ \tag{5.1}$$

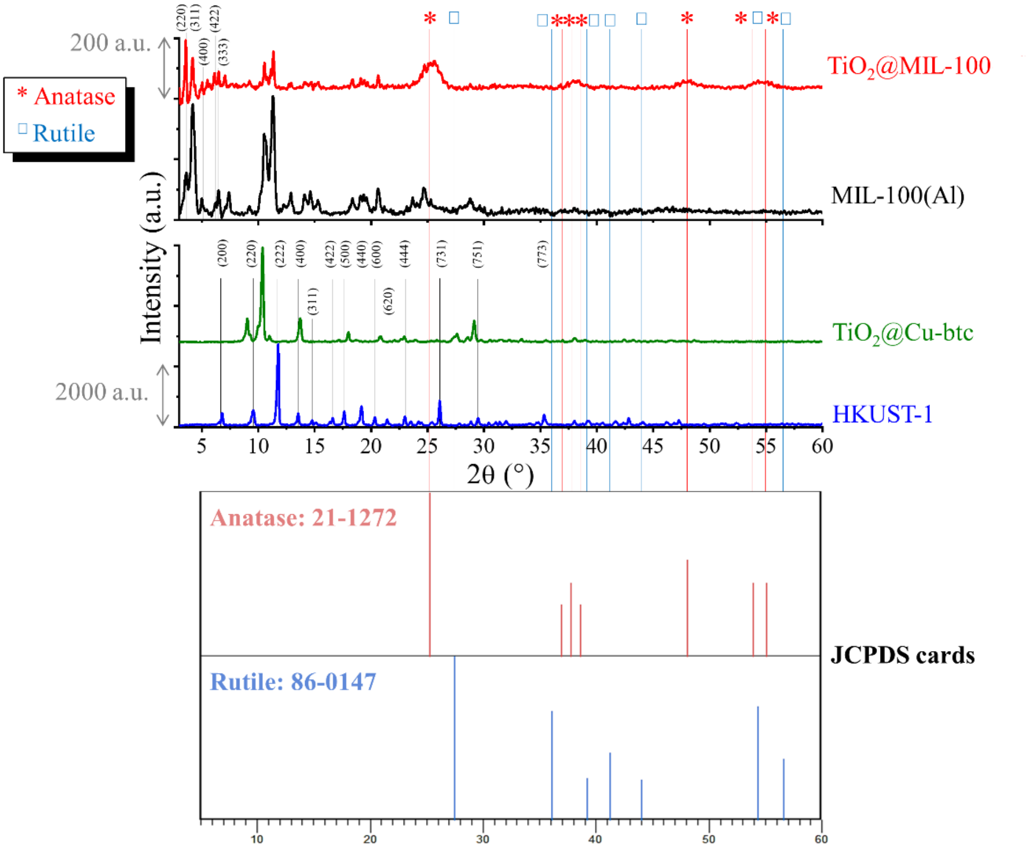

Figure 5.1: XRD patterns of the samples obtained in this work. The JCPDS file numbers 21-1272 and 86-0147 were used as the references for anatase and rutile, respectively. Such JCPDS cards are also exhibited for reference purposes.

After the chemical modification of HKUST-1 with TiO_2, a diffraction line ascribed to rutile at 2θ around 27.5° was detected, commonly associated with its (110) crystal plane [117]. The crystallization of rutile was not expected since, at standard conditions of pressure, anatase only transforms into rutile at temperatures above 500 ºC [118]. However, the acidification of the solution during the transformation of $Cu_3(btc)_2$ into $Cu_2(btc)(OH)(H_2O)$ could have favored rutile formation due to the low concentration of OH^- ligands in Ti(IV) complexes, allowing corner-shared bonds to give rise to the TiO_2 framework [119]. No XRD reflections associated with anatase were observed for TiO_2@Cu-btc.

Regarding the crystalline phases of titania, it has been reported that anatase has a higher photoactivity than rutile [120]. This behavior seems to be related to several factors. Some authors reported that anatase has a higher adsorption capacity, smaller particle size, and larger specific surface area than rutile [110]. Besides, it has been suggested that anatase has a lower recombination rate of charge carriers than rutile, which increases the concentration of photo-generated electrons and holes on the former surface. All these factors contribute to the enhanced photoactivity of anatase when compared to rutile [121].

Figure 5.2 depicts the FTIR spectra taken for MIL-100(Al), TiO_2@MIL-100, HKUST-1, and TiO_2@Cu-btc. The inset displayed in this Figure shows the FTIR spectrum collected for a pure TiO_2 sample, mainly formed by anatase. The spectra obtained for MIL-100(Al) and HKUST-1 are analogous to those reported elsewhere [122–124]. Additional absorption bands are noticed when the spectra of TiO_2-loaded samples are compared to those collected for the pure MOFs. The bands observed from 400 to about 920 cm^{-1} have been assigned to Ti–O bonds [125,126]. The features at 1390 and 1490 cm^{-1} are associated with CH_3 and CH_2 bending modes [127]. These bands can be related to IPrOH used in the sol-gel synthesis of TiO_2 or EtOH and DMF derived from the MOFs preparation. It can be observed that the bands ascribed to Ti–O bonds are so strong in TiO_2@MIL-100 that the absorption bands ascribed to MIL-100(Al) from 400 to 770 cm^{-1} are not visible in the composite; the superposition of the absorption bands related to TiO_2 and MIL-100(Al) does not allow identifying the latter signals in the composite's spectrum. The same behavior is not observed for TiO_2@Cu-btc, where the copper trimesate (mainly $Cu_2(btc)(OH)(H_2O)$) absorption bands from 400 to 800 cm^{-1} are still perceptible in the composite.

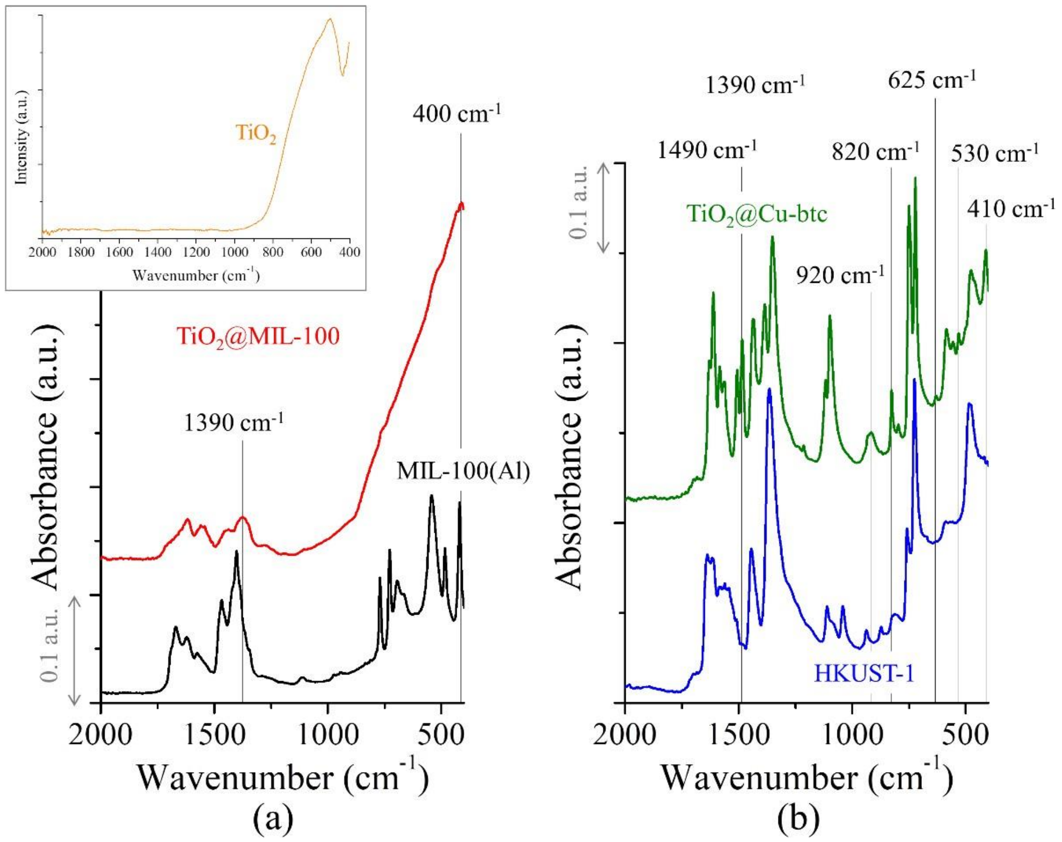

Figure 5.2: FTIR spectra obtained for (a) MIL-100(Al) and TiO_2@MIL-100 and (b) for HKUST 1 and TiO_2@Cu-btc. Inset: reference spectrum obtained for a pure TiO2 sample.

Figure 5.3 depicts the Raman spectra of the MOFs and composites prepared in this study. It is also displayed the reference spectra for anatase and rutile; differently from the observed for FTIR, these two polymorphs' spectra areeasily distinguished by Raman spectroscopy.

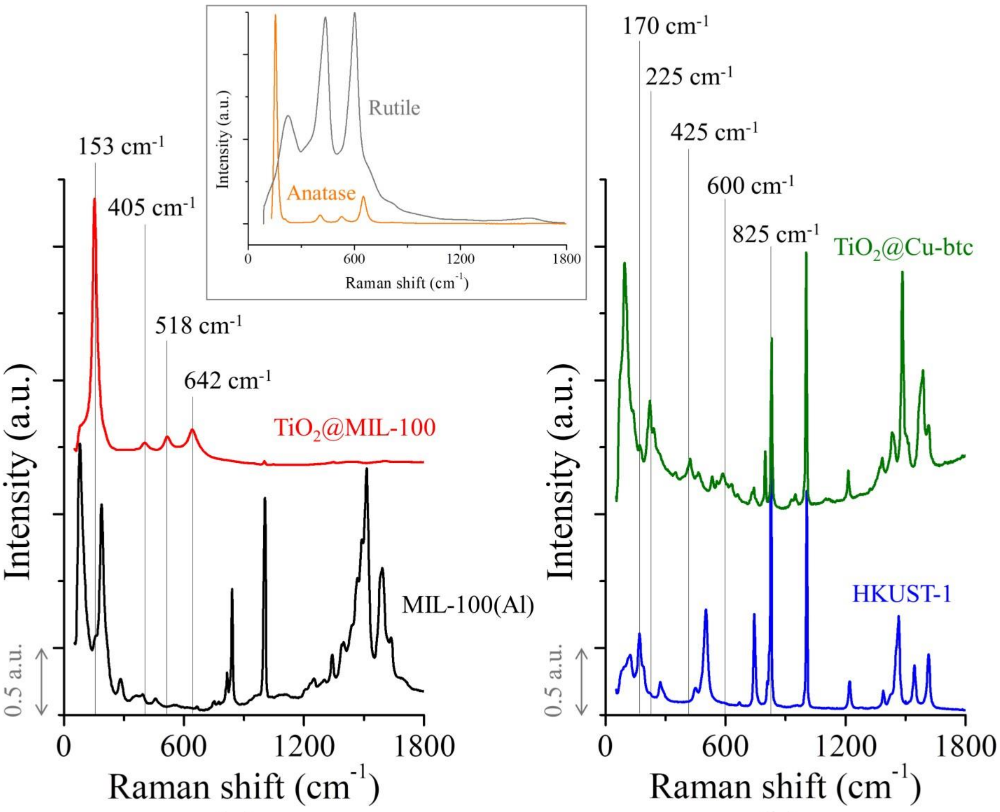

(a) (b)

Figure 5.3: Raman spectra collected for (a) MIL-100(Al) and TiO_2@MIL-100 and (b) for HKUST-1 and TiO_2@Cu-btc. Inset: reference spectra for anatase and rutile.

The spectra obtained for MIL-100(Al) and HKUST-1 are similar to those reported in the literature [128,129]. The spectrum of TiO_2@MIL-100 is similar to the observed for anatase; bands of the latter are highlighted in Figure 5.3a. The bands at 153, 405, 518, and 642 cm^{-1} have been ascribed to E_g, B_{1g}, B_{1g} + A_{1g}, and E_g vibration modes of anatase [130,131], revealing that titania is present in this polymorphic phase in MIL-100(Al), which agrees with XRD (Figure 5.1). The incorporation of TiO_2 into copper trimesate gave rise to a new band at 170 cm^{-1} (Figure 3b). Moreover, the bands at 225 cm^{-1} and 825 cm^{-1} which are related to Cu–Cu stretching [38,132] and C–H bending of the btc ligand [133], respectively, are present in HKUST-1 and TiO_2@Cu-btc. This behavior was already expected since these bondings are present in both materials [116]. Bands assigned to rutile were identified in the spectrum of TiO_2@Cu-btc, which is also in line with XRD (Figure 1). The bands at about 225, 425, and 600 cm^{-1} have been related to second-order scattering (SOS), $E_{g,}$ and A_{1g} modes of rutile [134]. Nonetheless, rutile bands are observed at lower intensities in TiO_2@Cu-btc than the anatase bands in TiO_2@MIL-100. This behavior is in line with FTIR (Figure 5.2) and may reveal TiO_2 nanoparticles are present at a higher concentration in TiO_2@MIL-100 than in TiO_2@Cu-btc. This finding is probably due to the non-porous structure of $Cu_2(btc)(OH)(H_2O)$ [116], which suggests that TiO_2 crystallized on its surface. However, due to the high porosity of MIL-100(Al), titania crystallized within its porous structure, leading to a higher amount of TiO_2 in it.

The bandgap energy (E_{gap}) of the prepared materials was evaluated by plotting the so-called Kubelka-Munk function $[(F(R)h\nu)^n]$ as a function of the photon energy ($h\nu$), where h is Planck constant (4.14×10^{-15} eV.s) and ν is the photon frequency (Hz). F(R) can be calculated by Equation (2), where R is the reflectance (%) assessed by UV-Vis spectroscopy.

$$\mathrm{F(R)} = \frac{(1-\mathrm{R})^2}{2\mathrm{R}} \tag{5.2}$$

The index n is associated with the transition exhibited by an electron when promoted from the valence band to the conduction one. It has been reported $n = \frac{1}{2}$ for an indirect allowed transition, $n = 2$ for a direct allowed transition, $n = 3$ for an indirect forbidden transition, and $n = \frac{2}{3}$ for a direct forbidden transition [135]. Direct allowed transitions occur when the electron is directly promoted to the conduction band with no phonons' absorption or emission. Phonons play an essential role in direct forbidden transitions and are less likely to occur. Indirect transitions are observed when at least one phonon participates in the absorption or emission of another phonon. Both direct and indirect transitions can occur in semiconductor materials [136]. TiO_2 has an indirect bandgap, and we considered $n = \frac{1}{2}$ in our calculations, as recommended elsewhere [137]. E_{gap} was estimated by extrapolating the line tangent to the inflection point of $(F(R)h\nu)^{1/2}$, as represented in Figure 5.4.

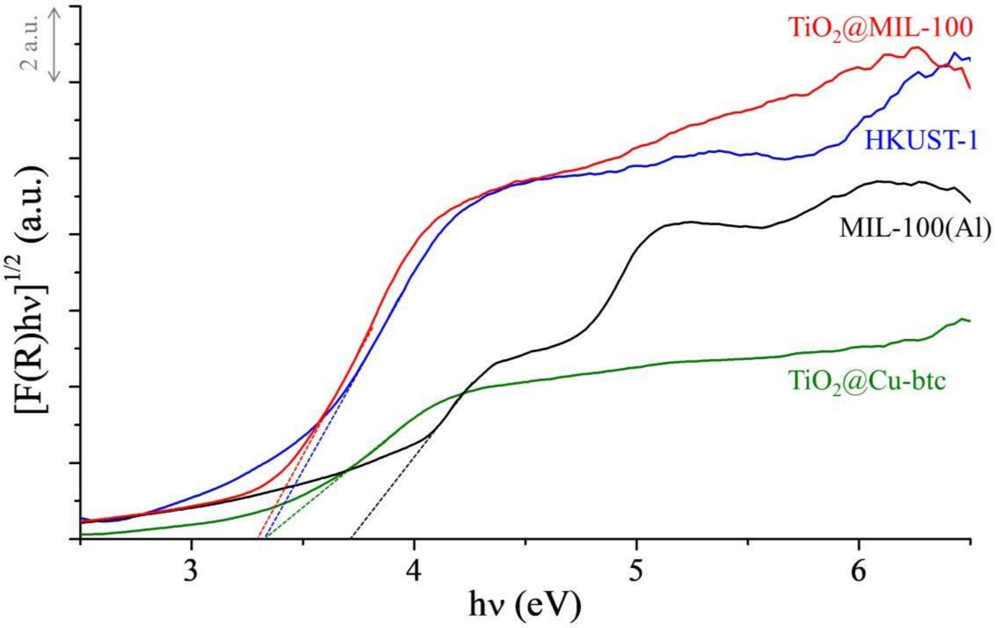

Figure 5.4: $[F(R)h\nu]^{1/2}$ as a function for the photon energy for the samples prepared here.

It was noted that the addition of TiO_2 decreased the value of E_{gap} for MIL-100(Al) from 3.70 to 3.27 eV. On the other hand, no noticeable change in this value was observed between HKUST-1 and TiO_2@Cu-btc, since E_{gap} remained around 3.32 eV. Anatase and rutile are reported to have E_{gap} around 3.2 and 3.0, respectively [138]. This result shows that the addition of TiO_2 to MIL-100(Al) had a significant effect on its electronic structure. This reinforces that TiO_2 nanoparticles are present within MIL-100(Al)’s porous structure. Furthermore, as evidenced by FTIR and Raman spectroscopies (Figure 5.2 and Figure 5.3), TiO_2 anatase is present at a significant concentration in MIL-100(Al); whereas TiO_2 rutile was observed at a slight concentration in $Cu_2(btc)(OH)(H_2O)$ powder, which also contributes to this finding.

Figure 5.5 displays TG and DTG profiles assessed for the samples prepared in this study. The profiles obtained for the pure MOFs are similar to those already reported in the literature [139,140].

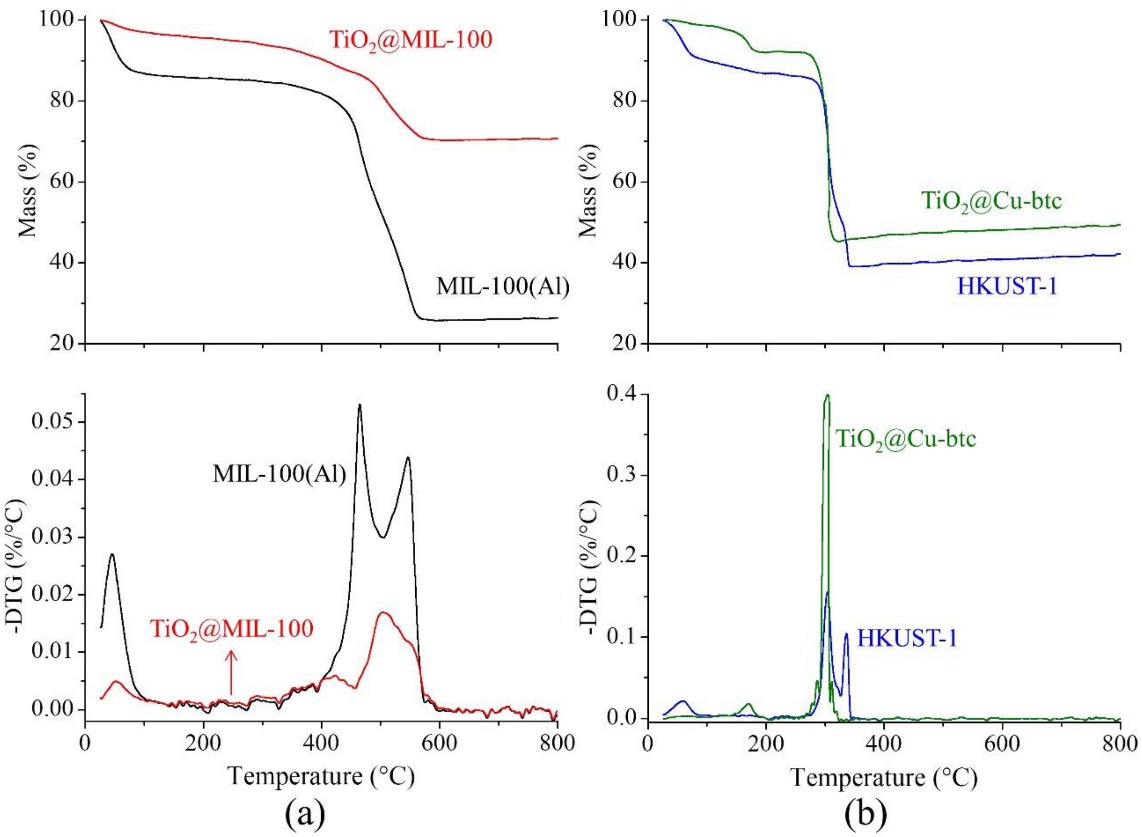

Figure 5.5: TG and DTG profiles obtained for (a) MIL-100(Al) and TiO_2@MIL-100 and (b) for HKUST-1 and TiO_2@Cu-btc.

The mass loss at temperatures up to 100 °C is ascribed to the removal of water and other physisorbed molecules [36]. MIL-100(Al) exhibited a mass loss of 13% at temperatures up to 200 °C, while HKUST-1 lost 10% in mass up to 100 ºC. However, TiO_2@Cu-btc lost 7.1% in mass at temperatures from 100 to 200 °C which is ascribed to the coordinated water in $Cu_2(btc)(OH)(H_2O)$ powder [116,141], reaching a total loss of 8.7% of its initial mass up to 200 °C. TiO_2@MIL-100 only lost 5% in mass in temperatures up to 200 °C. The sharp decrease in weight experienced by all the materials at temperatures about 300 and 400 °C has been associated with the elimination of organic linkers from their structures [36,142,143]. A distinct behavior is noticed when the TiO_2-containing samples are compared to the pure MOFs as the former had a smaller mass loss than the latter at the end of the analysis. This difference is related to the presence of TiO_2 in these materials, which displays higher thermal stability than the MOFs in the examined temperature range [144]. Moreover, the TiO_2@MIL-100 and TiO_2@Cu-btc were submitted to a pre-drying step during their preparation, leading to prior dehydration and a lower mass loss at temperatures up to 200 °C. The difference in the thermal behavior of pure and TiO_2-loaded materials is more noticeable for TiO_2@MIL-100 than TiO_2@Cu-btc, confirming that TiO_2 is present in a larger amount in the former compared to the latter. This finding is in line with the XRD, FTIR, and Raman results (Figure 5.1 and Figure 5.3) and can be related to the available surface for the nucleation of TiO_2 nanoparticles.

A mass balance was carried out to evaluate the amount of TiO_2 present in the composites. This calculation is expressed in Equation (5.3), where M_D is the mass of the dried material (g), M_L is the mass of ligand (g), and M_C is the mass of the calcinated material (g), all considered for the material j (j = MOF or TiO_2@MOF). The mass values observed at 400 ºC, 400-600 ºC, and 800 ºC were considered for calculating M_D, M_L, and M_C for MIL-100(Al)'s compounds, respectively. For HKUST-1 and TiO_2@Cu-btc the temperatures were 250 ºC (M_D), 250-400 ºC (M_L), and 800 ºC (M_C).

$$\mathrm{M}_{\mathrm{D}_j} = \mathrm{M}_{\mathrm{L}_j} + \mathrm{M}_{\mathrm{C}_j} \tag{5.3}$$

Since the MOFs were the matrix used to prepare TiO_2@MOFs, one should expect that after the calcination, the mass that remains in the TiO_2@MOFs is partially due to TiO_2 and partially due to the residues of MOF's structures, as shown in Equation (5.4), where $M_{MOF\_TiO2@MOF}$ and $M_{TiO2\_TiO2@MOF}$ are related to the mass of MOF and TiO_2 in the TiO_2@MOF composite, respectively.

$$\mathrm{M}_{\mathrm{MOF\_TiO2@MOF}} + \mathrm{M}_{\mathrm{TiO2\_TiO2@MOF}} = \mathrm{M}_{\mathrm{D}_{\mathrm{TiO2@MOF}}} \tag{5.4}$$

Moreover, these residues are the same obtained after the calcination of pure MOFs. Thus, a ratio between the masses of calcined and dried pure MOFs is related to its contribution to the final mass of the calcinated TiO_2@MOF, as demonstrated in Equation (5.5).

$$\mathrm{M}_{\mathrm{MOF\_TiO2@MOF}} \times \frac{\mathrm{M}_{\mathrm{C}_{\mathrm{MOF}}}}{\mathrm{M}_{\mathrm{D}_{\mathrm{MOF}}}} + \mathrm{M}_{\mathrm{TiO2\_TiO2@MOF}} = \mathrm{M}_{\mathrm{C}_{\mathrm{TiO2@MOF}}} \tag{5.5}$$

This calculation revealed that the mass fraction of titania in dry TiO_2@MIL-100 and TiO_2@HKUST-1 are around 68 wt.% and 9.3 wt.%, respectively. This confirms that TiO_2 has been incorporated in a significant amount within MIL-100(Al)'s porous structure, whereas its fraction in $Cu_2(btc)(OH)(H_2O)$ is comparatively poor due to the non-porous structure of this copper trimesate.

Figure 5.6 shows SEM images, TEM micrographs, and EELS spectra taken for MIL-100(Al) and TiO_2@MIL-100. Particles with sharp edges are observed for MIL-100(Al), which agrees with the literature [145,146].

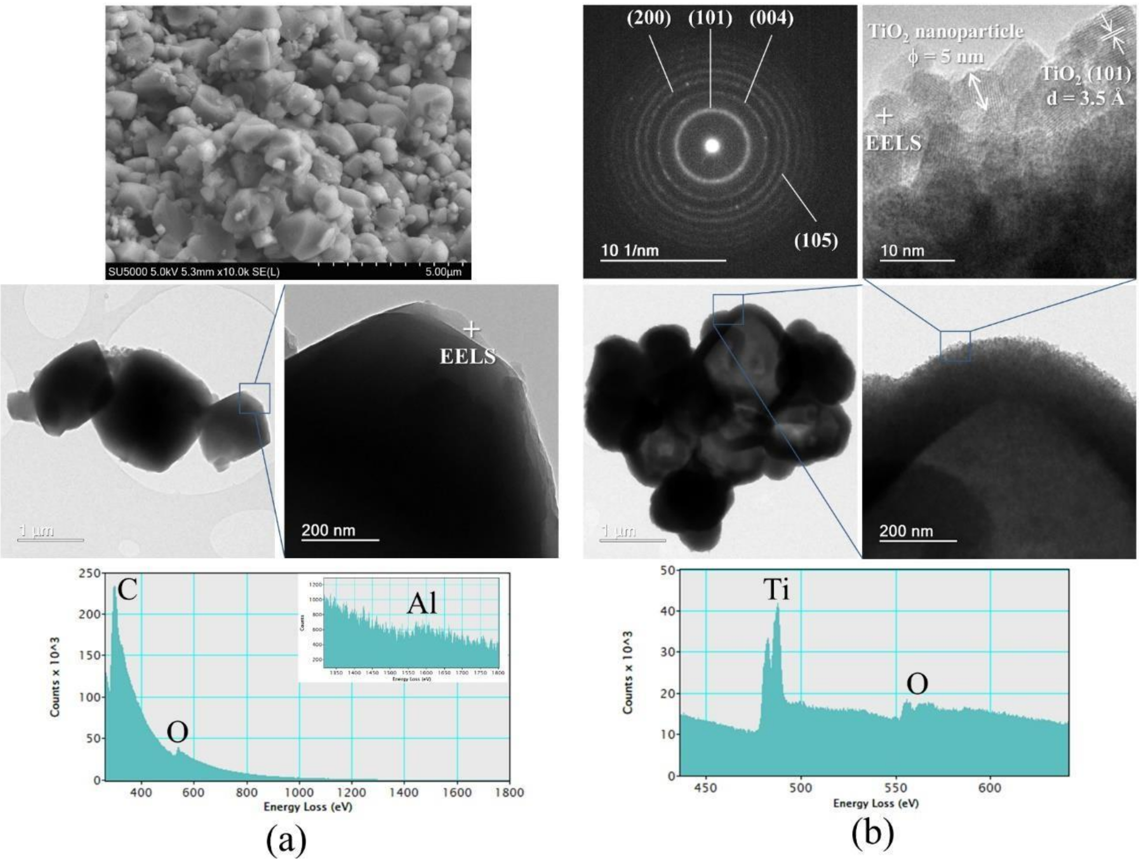

Figure 5.6: (a) SEM micrographs (top), TEM micrographs, and EELS spectrum of MIL-100(Al). (b) TEM images, EELS spectrum, and SAED pattern of TiO_2@MIL-100. The location from which the EELS spectrum was taken is identified with a cross (+).

As was expected, the EELS spectrum of this material identified carbon, oxygen, and aluminum. A distinct morphology was noticed for TiO_2@MIL-100, where TiO_2 nanoparticles with sizes as small as 5 nm were observed anchored to the TiO_2@MIL-100's crystals.

SAED analyses revealed that the titania nanoparticles observed in these micrographs are related to anatase; the SAED pattern taken for a TiO_2 nanoparticle is displayed in Figure 5.6b, where it is possible to observe the main Debye-Scherrer concentric rings of anatase. This result is in line with XRD (Figure 5.1), which also pointed out that anatase is the main phase in TiO_2@MIL-100. The EELS spectrum collected for a titania nanoparticle is exhibited in Figure 5.6b. The molar composition (mol.%) of this particle is 34Ti–66O, which gives a ratio of 2O: 1Ti, as expected for TiO_2. Figure 5.7 displays the EDS spectra and composition maps obtained for TiO_2@MIL-100. These results reveal that titania is mainly observed near the aluminum sites, reinforcing that TiO_2 mainly crystallized inside the MOF's pore structure.

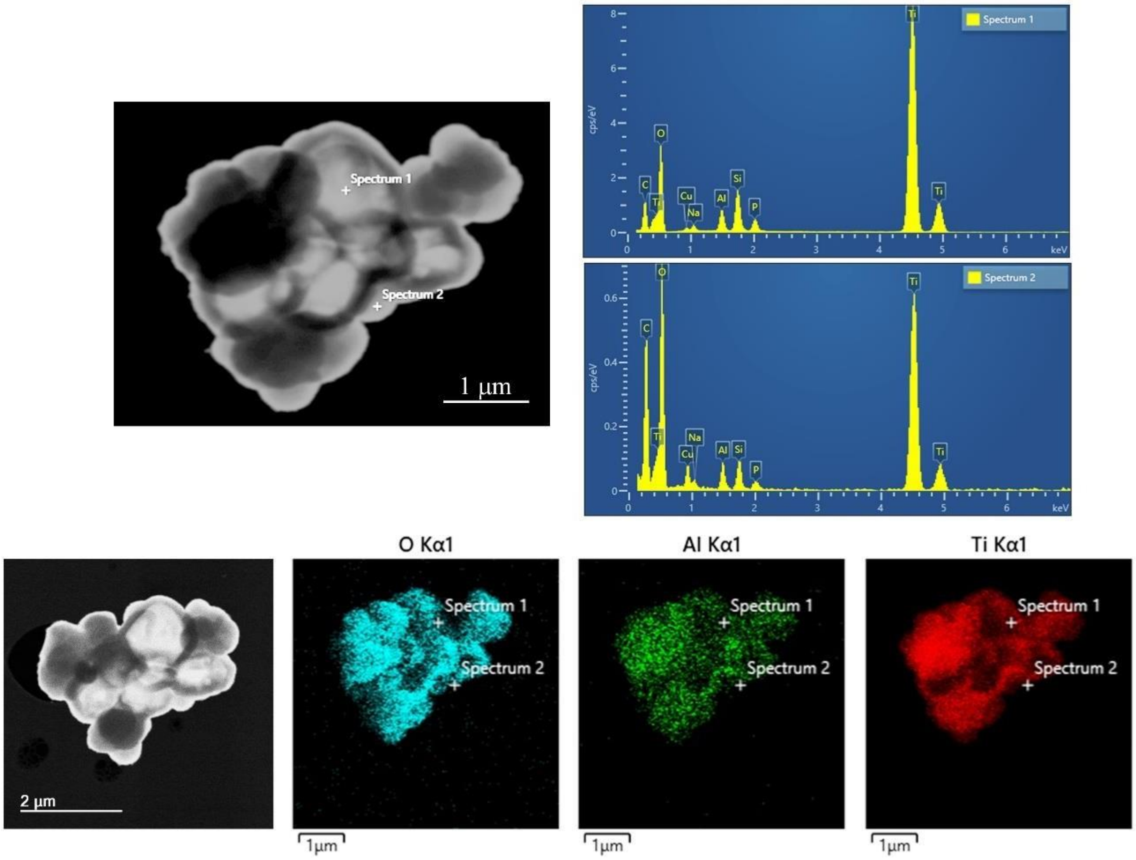

Figure 5.7: EDS spectra and compositional maps obtained for TiO_2@MIL-100. The positions from which the EDS spectra were taken are indicated in these images.

SEM images, TEM micrographs, and EELS spectra of HKUST-1 and TiO_2@HKUST-1 are shown in Figure 5.8. Octahedral-shaped particles were observed for HKUST-1, which agrees with the literature [107].

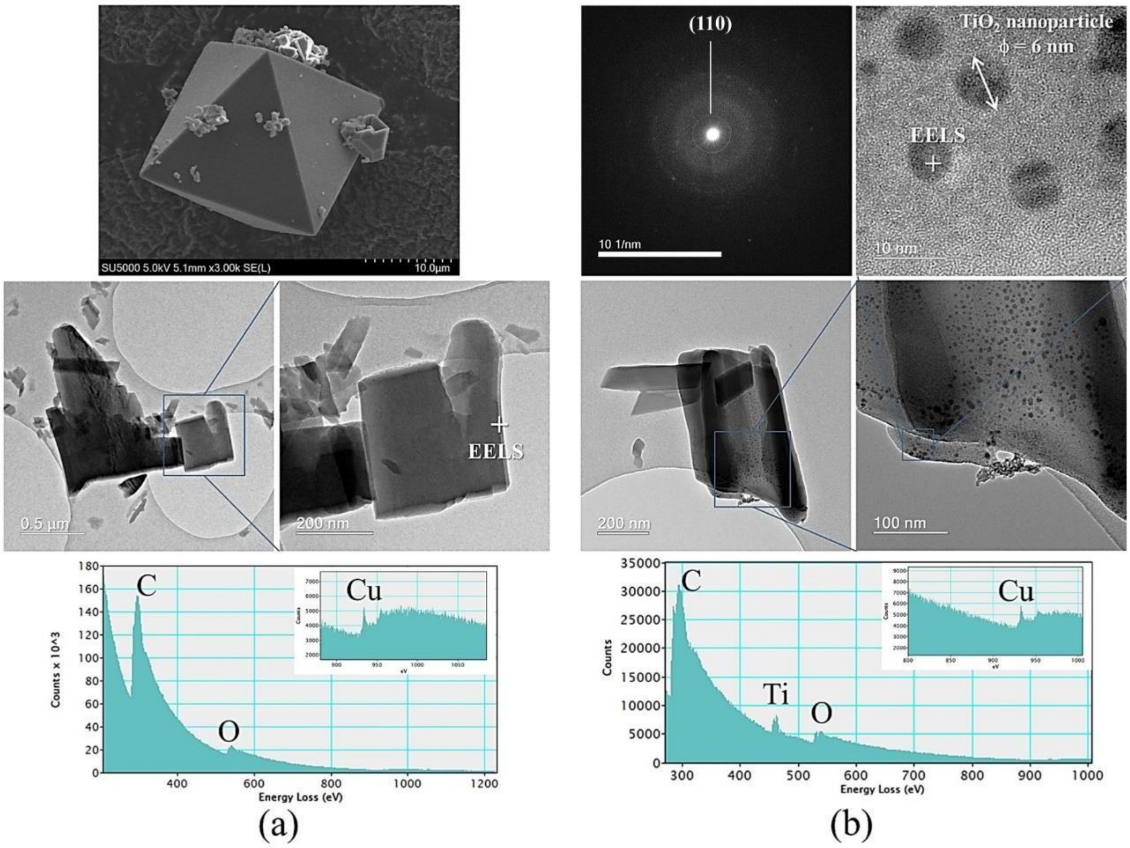

Figure 5.8: (a) SEM micrographs (top), TEM micrographs, and EELS spectrum of HKUST-1. (b) TEM images, EELS spectrum, and SAED pattern of TiO_2@Cu-btc. The location from which the EELS spectrum was taken is identified by a cross (+).

However, the same crystal morphology was not observed in the TEM displayed in Figure 5.8a, suggesting that the MOF's structure collapsed during the sample preparation (sonication in EtOH at room temperature for 5 min), which highlights its low chemical stability. The EELS spectrum collected for a titania nanoparticle is exhibited in Figure 5.6b. The molar composition (mol.%) of this particle was also 12Ti – 74O – 14Cu, differing from TiO_2@MIL-100. This is due to the environment where the EELS spectra were taken: in the former, the TiO_2 nanoparticle is rounded by others including underneath it; in the latter, it is rounded mostly by the copper trimesate phase, which contributes to the detection of copper and also rises the concentration of oxygen (see Figure 5.6 and Figure 5.8). Needle-shaped crystals are observed in Figure 5.9, which is in accord with the morphology of Cu_2(btc)(OH)(H_2O) crystals [38,116]. Moreover, TiO_2 nanoparticles of about 6 nm in size were observed anchored on the needle-like crystals of Cu_2(btc)(OH)(H2O) (Figure 5.8). A concentric Debye-Scherrer ring ascribed to the (110) crystal plane of rutile was observed in the obtained SAED pattern (Figure 5.8b), confirming that TiO_2 crystalized as rutile. Figure 5.9 displays the EDS spectrum and a composition map obtained for TiO_2@Cu-btc. These results reveal that titania is only present at the surface of Cu_2(btc)(OH)(H_2O)'s crystals and not necessarily close to its metal sites, as in TiO_2@MIL-100.

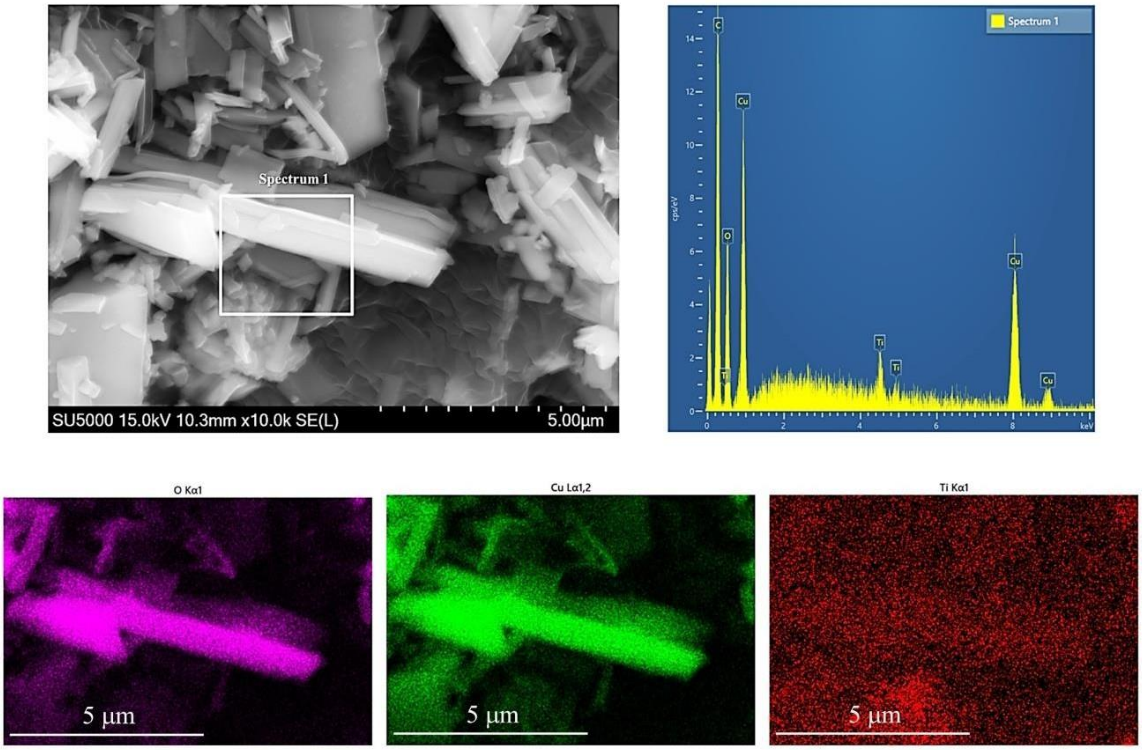

Figure 5.9: SEM image, EDS spectrum, and compositional map obtained for TiO_2@Cu-btc. The area from which the EDS spectrum was taken is highlighted in the SEM micrograph.

Figure 5.10 shows the gas sorption isotherms collected in this study. N_2 at 77K was used to analyze MIL-100(Al), TiO_2@MIL-100, and HKUST-1, while TiO2@Cu-btc was examined with Kr at 77K due to the low porosity of this sample compared to HKUST-1. The specific surface areas (SSA) ofthe compounds were calculated by the multipoint BET method.

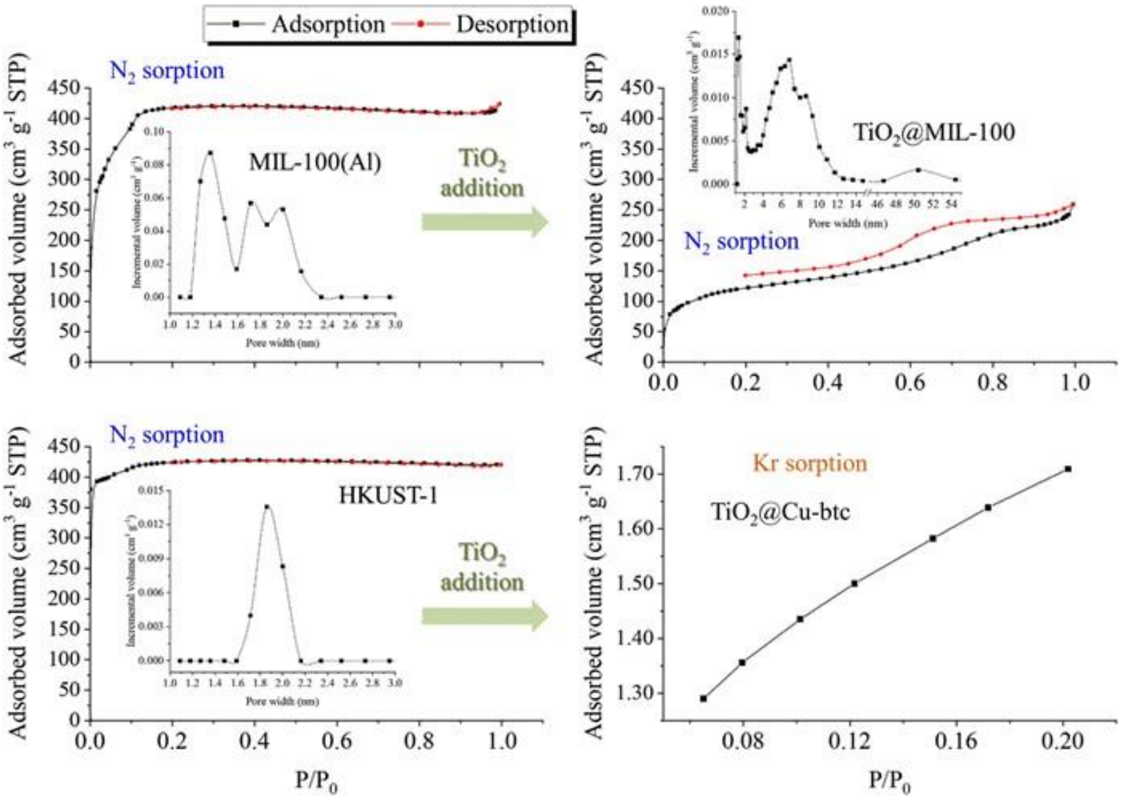

Figure 5.10: Gas sorption isotherms and pore size distributions of the samples prepared in this work. MIL-100(Al), TiO_2@MIL-100, and HKUST-1 were examined using N_2, while TiO_2@HKUST was analyzed with Kr.

MIL-100(Al) showed an SSA of 1787 $m^2.g^{-1}$, but this value lowered to 417 $m^2.g^{-1}$ after incorporating TiO_2 into the MOF. This finding reinforces that TiO_2 nanoparticles are also present both inside its framework and on the surface of its crystals, causing a partial blockage of pores. On the other hand, the coper trimesate experienced a variation of SSA from 1360 to 8 $m^2.g^{-1}$ after incorporating TiO_2 into it, highlighting the low porosity of $Cu_2(btc)(OH)(H_2O)$ and, by consequence, TiO_2@Cu-btc. According to IUPAC [147], MIL-100(Al) and HKUST-1 have a type-I isotherm usually reported for these materials [35,116]. TiO_2@MIL-100 displays a type-IV isotherm, commonly associated with mesoporous materials. Its higher mesoporosity when comparing to MIL-100(Al) (which also presents pores with more than 2 nm in diameter) can be explained by the collapse of some of its cavities during the growing processes of TiO_2 nanoparticles [148]. It is worth stressing that such nanoparticles were able to grow up to 5 nm in size (Figure 5.6). The slight difference between the adsorption and desorption branches in this sample can be due to the strong interaction between the N_2 molecules and Ti sites present in this MOF. Due to its low porosity, TiO_2@Cu-btc was evaluated only at relative pressures below 0.30, which is adequate to determine its SSA by the BET method, but insufficient to examine its isotherm deeply.

Incorporating TiO_2 into MIL-100(Al) gave rise to pores between 4 and 10 nm. In comparison, pores with sizes around 1.7 nm disappeared in MIL-100(Al) after this chemical modification, suggesting a partial blockage of the MOF's pore structure by TiO_2 nanoparticles and supporting that some of its cavities were collapsed by their growing process. This guarantees that TiO_2 nanoparticles could access the MOF's pore network and are also present inside the pores, which agrees with the EDS compositional map displayed in Figure 5.7.

Figure 5.11a and Figure 5.11b display spin trapping EPR spectra obtained with DMPO spin trap (100 mM) in aqueous solutions containing either TiO_2@MIL-100 or TiO_2@Cu-btc. While the dark spectrum of TiO_2@MIL-100 does not present any paramagnetic species, after 10 min of UVA illumination, signals due to different spin adducts appeared. On the other hand, the EPR spectrum of sample TiO_2@Cu-btc shows different spin adducts even in the dark that are transformed after 10 min UVA illumination. The presence of spin adducts without TiO_2@Cu-btc catalyst illumination indicates that ROS were present even before adding the spin trap, which probably remains from the transformation of HKUST-1 into Cu_2(btc (OH)(H_2O).

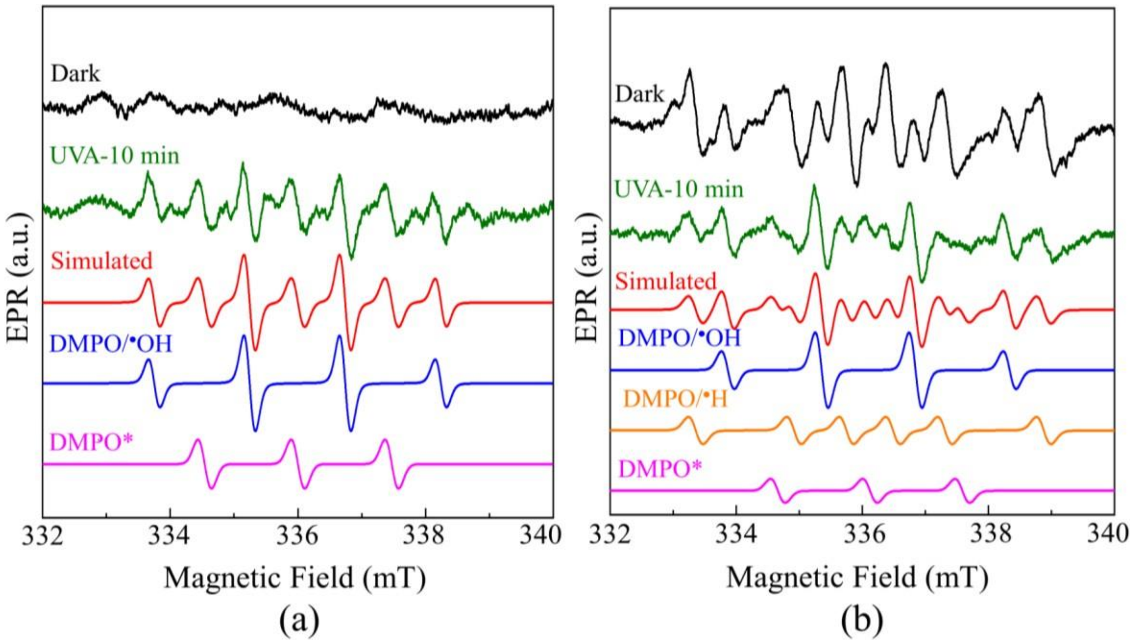

Figure 5.11: EPR spin trapping experiments with DMPO spin trap in aqueous solution (100 mM) containing either (a) TiO_2@MIL-100 or (b) TiO_2@Cu-btc catalysts. The experimental EPR spectra were obtained in the dark (black) and after 10 min UVA illumination (dark green). Simulated EPR spectra (red line) for the DMPO spin adducts: DMPO* (magenta, aN = 1.46 mT), DMPO/•OH (blue, aN = aH(β) = 1.50 mT), and DMPO/•H (orange, aN = 1.56 mT and aH(β) = 2.39 mT). The reader is encouraged to see this Figure in color in the online version of this work.

Two different spin adducts are clearly observed in Figure 5.11a and Figure 5.11b after UVA illumination; they were identified using the Easyspin simulation software [149]. The EPR signal of the first spin adduct (blue line in Figure 5.11a and Figure 5.11b) is characterized by a hyperfine interaction between an unpaired electron (S = ½), arising from a nitroxide group with the nuclear spin ($I = 1$) of ^{14}N (99.6%), and which also interacts with the nuclear spin ($I = ½$) of the hydrogen atom (^{1}H) at the β-site of the molecule, giving rise to six possible electronic spin transitions. The values of the isotropic hyperfine interaction constants obtained after simulating this spectrum were $a_N = a_{H(\beta)} = 1.50$ mT, which agrees with the values already reported for the DMPO/$^{\bullet}$OH adduct [150,151]. The spin adduct identified as DMPO* (magenta line in Figure 5.11a and Figure 5.11b) is not associated with the capture of any specific ROS but instead with the deprotonation of DMPO, resulting in a hyperfine interaction triplet between the electronic spin and the nuclear spin $I = 1$ of ^{14}N ($a_N = 1.46$ mT) [152]. This signal can be related to the interaction of the UVA light with DMPO molecules. The formation of hydroxyl radicals ($^{\bullet}OH$) during the UVA illumination of TiO_2@MIL-100 indicates the production of ROS from the exchange of charge carriers between the catalyst and the solvent (Type I mechanism). Another ROS which is probably formed during the illumination of the suspended catalyst particles is the superoxide radical ($^{\bullet}O_2^-$), which is formed from excited electrons in the catalyst particles and molecular oxygen dissolved in the solvent. The absence of spin adducts associated with the capture of $^{\bullet}O_2^-$ is probably due to its short half-life (a few seconds). The DMPO/$^{\bullet}OH$ spin adduct may be due to a direct formation process involving hydroxyl radicals or a secondary formation process involving superoxide radicals [153].

Figure 5.12a exhibit the EPR spectra taken for TiO_2@MIL-100 in the presence of PBN spin trap (200 mM) in a 1:1 ethanol-water solution for different UVA illumination times (in between 0 and 30 min). Despite the lower diversity of ROS interacting with PBN, the choice of this spin trap was based on the high stability of its spin adducts, allowing the evaluation of the kinetics of radical generation. The EPR spectrum collected during the illumination of TiO_2@MIL-100 is specific to the capture of the α-hydroxyethyl radical ($H_3C{-}^{\bullet}CH{-}OH$) by PBN (Figure 5.12b). The signal arises from six spin transitions and is explained by the hyperfine interaction of an unpaired electron centered on oxygen, with the nuclear spin (I = 1) from ^{14}N and in addition, also with the nuclear spin (I = ½) of ^{1}H at the β-site of the molecule. The values of the isotropic hyperfine interaction constants obtained by spectrum simulation (red line, Figure 5.12b) were $a_N = 1.48$ mT and $a_{H(\beta)} = 0.30$ mT, values consistent with those already reported elsewhere [154]. The formation of the α-hydroxyethyl radical results from the interaction between hydroxyl radicals and ethanol molecules present in the medium. The use of PBN as a spin trap confirmed the generation of the $^{\bullet}OH$ radicals, similar to the spin trapping experiment with DMPO, from TiO_2@MIL-100 and evidenced its ability to exchange charge carriers with the solvent molecules under illumination with UVA light. The same spin trapping experiments were also done with the TiO_2@Cu-btc catalyst sample. However, no PBN spin adducts were generated with this catalyst under UVA light.

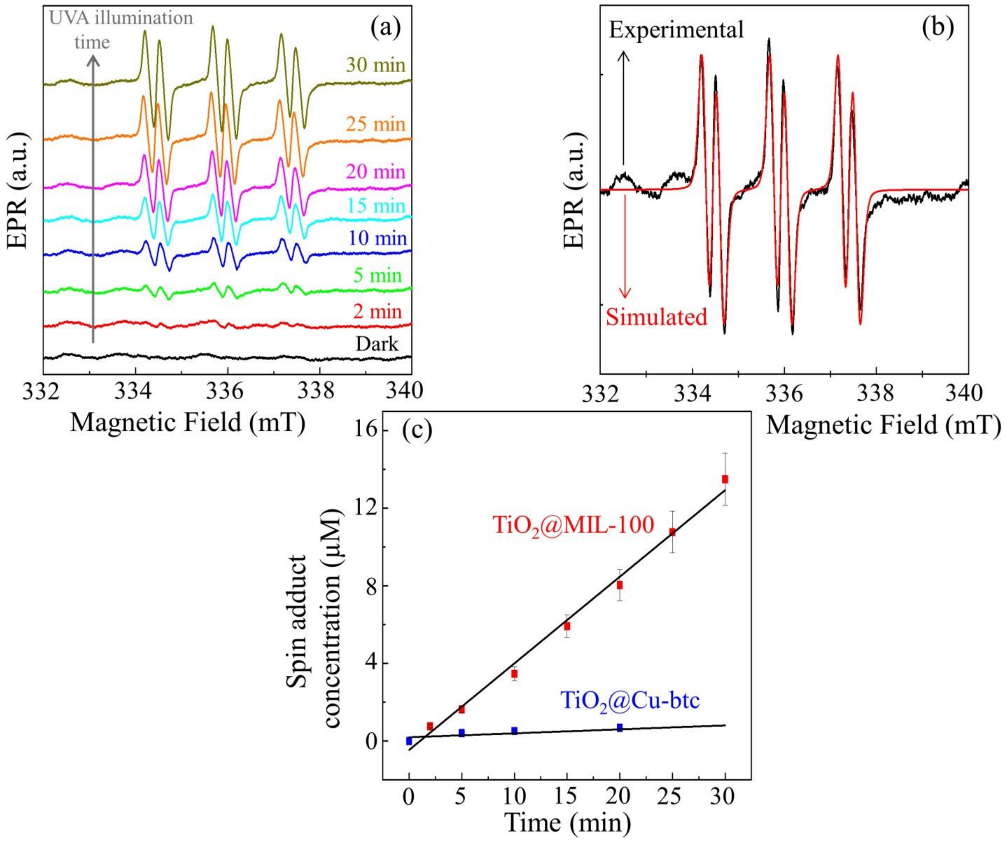

Figure 5.12: (a) PBN spin trapping EPR spectra obtained for a 1:1 ethanol-water solution containing TiO2@MIL-100 catalyst as a function of the UVA illumination time (0 to 30 min). (b) EPR spectrum obtained for TiO2@MIL-100 sample after 20 min of UVA illumination (black line). The red line corresponds to the spectrum simulation conducted for the α-hydroxyethyl PBN spin adduct. (c) Concentration of the PBN/ H3C–•CH–OH spin adduct as a function of the UVA illumination time for TiO2@MIL-100 (red dots) and TiO2@Cu-btc (blue dots). The reader is encouraged to see this Figure in color in the online version of this work.

The evaluation of the concentration of spin adducts generated upon the capture of α-hydroxyethyl by PBN during UVA illumination was performed from double integration of the EPR signals (Figure 5.12a) and compared with the signal intensity of a sample of known concentration (TEMPOL, 4-Hydroxy-Tempo, Sigma-Aldrich, 1 mM). The kinetics of spin adduct generation for the two samples are displayed in Figure 5.12c. The uncertainty in the spin adduct concentration is assumed to be within 10% of the value obtained by integration. The linear function associated with the spin adduct generation kinetics for sample TiO_2@MIL-100 is characteristic of a 1st order regime, i.e., $^{\bullet}$OH radical formation by charge carrier exchange during UVA illumination is a primary process and is not a secondary process resulting from cross-reactions.

The generation kinetics of spin adduct (PBN/ $H_3C–{}^{\bullet}CH–OH$) exhibited in Figure 5.12c establishes the photocatalytic activity of TiO_2@MIL-100 under illumination with UVA light. However, this characteristic is negligible on TiO_2@Cu-btc. Therefore, the stability of the MIL-100(Al) and its capacity of retaining TiO_2 nanoparticles inside its porous network guarantees numerous photocatalytic applications to TiO_2@MIL-100.

5.2 Photocatalytic tests

The adsorption and photodegradation of MB under UV light are shown in Figure 5.13. One can see that MIL-100(Al) presented higher adsorption capacity when comparing to the other compounds (it removed 45% of MB in the first 60 minutes, followed by TiO_2@MIL-100 with 33%, TiO_2@HKUST-1 with 32%, and HKUST-1 with 0%). This result is consistent with the higher SSA of the aluminum trimesate (1787 $m^2.g^{-1}$). As expected, the functionalization with TiO_2 decreased its adsorption capacity, probably due to the partial blockage of the MOF's pores and the decrease in its SSA ($SSA_{TiO2@MIL-100}$ = 417 $m^2.g^{-1}$). A different behavior was present in TiO_2@Cu-btc and HKUST-1. Despite its much higher SSA (1360 $m^2.g^{-1}$), HKUST-1 was not able to remove any amount of dye; whereas TiO_2@Cu-btc removed 32% of MB in dark conditions despite its low SSA (8 $m^2.g^{-1}$). This can be explained by an interaction between the positive charge of MB and the negative radicals present in TiO_2@Cu-btc's surface, as showed by spin trap EPR results. After illumination with the UVA light, TiO_2@MIL-100 was able to remove approximately 93% of MB; followed by TiO_2@Cu-btc, MIL-100(Al), and HKUST- 1, with 80%, 64%, and 20%, respectively.

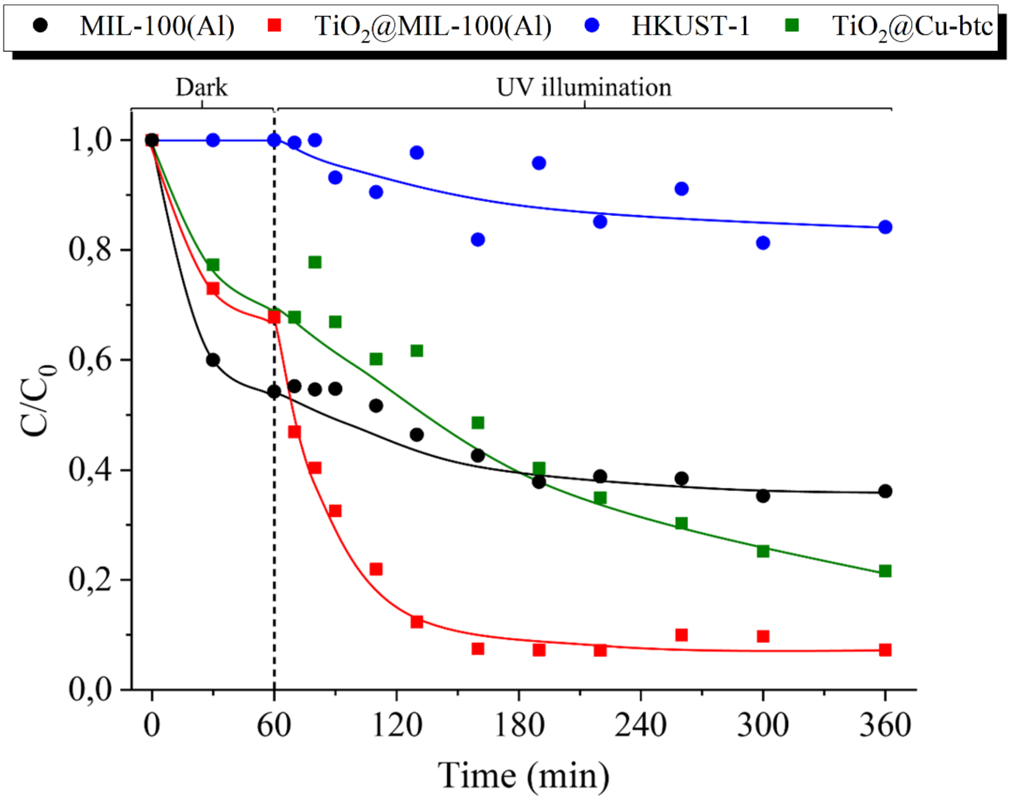

Figure 5.13: C/C$_0$ as a function of time on dark and irradiated conditions over MB.

The UV-Vis spectra and molecular structures of IBP and DIC are shown in Figure 14. IBP has a strong absorption band at 194 nm and a smaller one at 222 nm. Those bands have been related to π-π* transitions on its aromatic ring [155]. There is a bathochromic shift, also called redshift, in the spectrum of DIC compared to IBP. This behavior causes the absorption bands to shift towards longer wavelengths due to an additional aromatic ring observed in DIC's structure, and the nitrogen unpaired electrons. This scenario causes a higher delocalization of the electronic cloud and a noticeable shift in the absorption bands. DIC displays a strong absorption band at 198 nm and a broad one at 276 nm, associated with HOMO to LUMO transitions in π-π* orbitals [156].

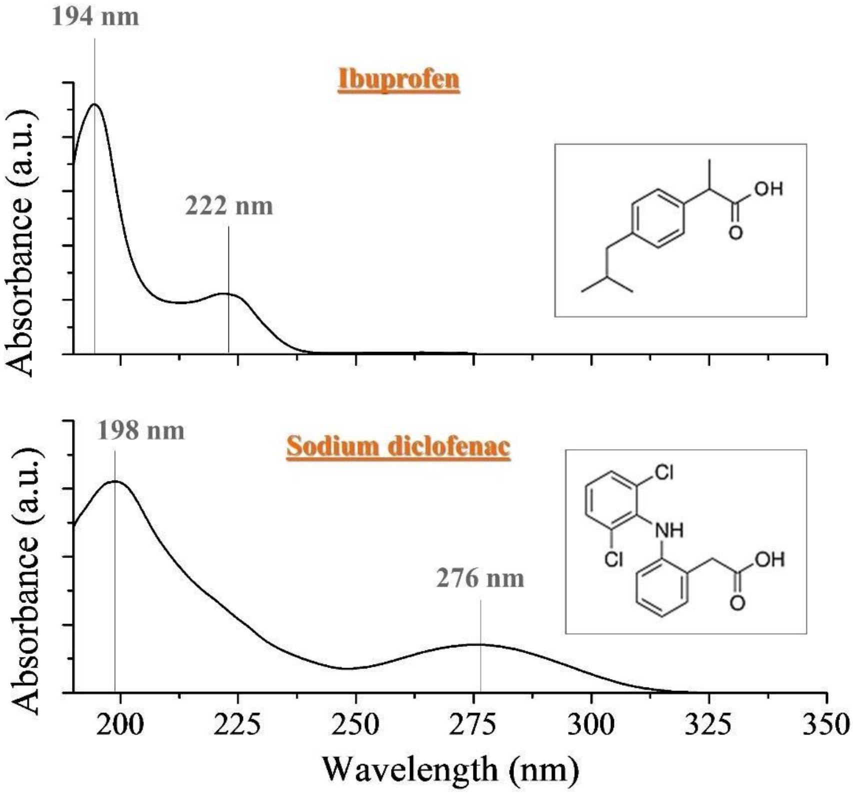

Figure 5.14: UV-Vis spectra and structural representation of IBP and DIC. Absorption spectra collected using aqueous solutions of IBP and DIC (10 mg.L^{-1}).

As observed in Figure 5.15, the addition of the MOF samples prepared here into aqueous solutions containing either IBP or DIC also caused a redshift on the spectra. This effect was more evident for KHUST-1 than for MIL-100(Al), and it has been ascribed to a pH change [62,157]. The initial pH of the water used in the photodegradation experiments was around 8.0. However, it lowered to 6.0 after reaching the adsorption equilibrium between the pollutant and samples, probably due to the deprotonation of carboxylic functions of the organic ligand, as well as the dissolution of Lewis acid Cu^{2+} cations in the case of the copper trimesate compounds.

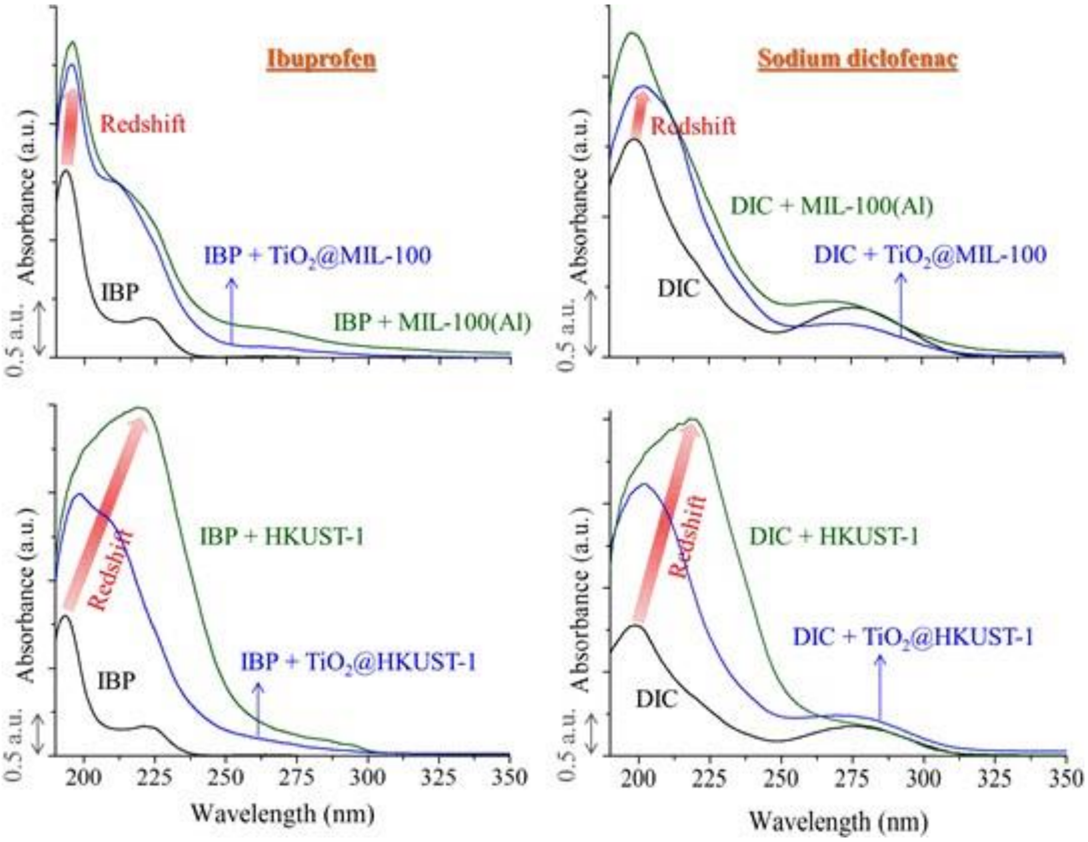

Figure 5.15: Absorption spectra of aqueous IBP and DIC solutions containing photocatalysts prepared in this work. These spectra were taken 12 h after preparing the solutions. The reader is encouraged to consult the online version of this Figure to see it in color.

As shown in Figure 5.16 and Figure 5.17, IBP and DIC solutions' illumination with UVA light caused a noticeable change in their UV-Vis spectra. This change is barely observed for solutions containing pure MOFs. However, it is clearly noticed for titania-loaded samples because the absorption spectra had a dramatic decrease in intensity as a function of time. A new absorption band centered at about 260 nm was noticed for IBP after 240 min of UVA illumination. This band has been related to p-Isobutyl-phenol as a by-product of IBP photodegradation, which is reinforced by the presence of an isosbestic point at 245 nm [158]. This compound results from IBP's decarboxylation due to its interaction with superoxide anion radicals ($^{\bullet}O_2^-$) formed under UVA light [62].

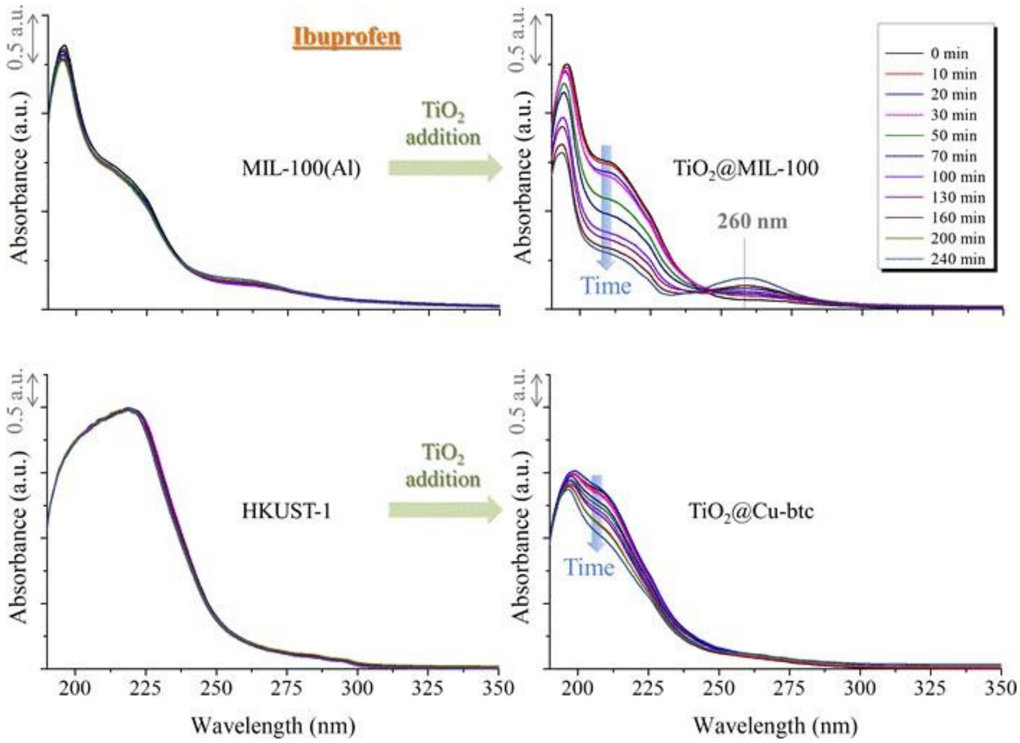

Figure 5.16: Effect of UVA illumination on the UV-vis absorption spectrum of IBP.

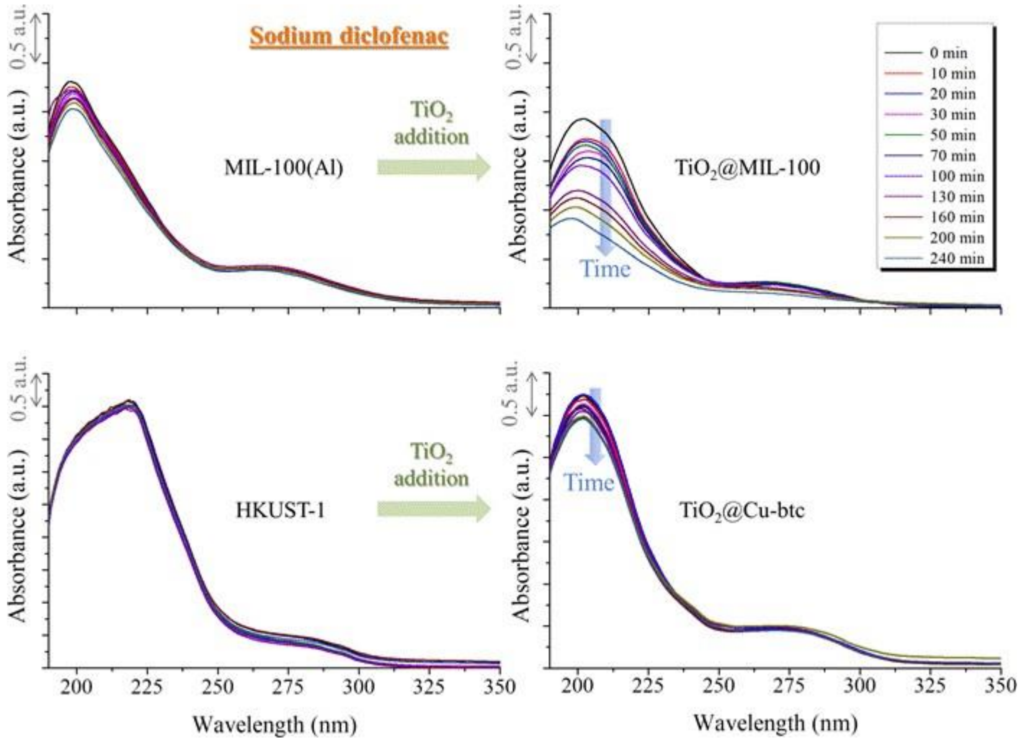

Figure 5.17: Effect of UVA illumination on the UV-vis absorption spectrum of DIC.

The Langmuir-Hinshelwood (L-H) kinetic model has been widely used to examine the degradation of organic pollutants by semiconductor photocatalysts [88]. It is based on Equation (5.6), where r is the pollutant oxidation rate ($mg.L^{-1}min^{-1}$), C the pollutant concentration ($mg.L^{-1}$), t the irradiation time (min), k the reaction rate ($mg.L^{-1}min^{-1}$), and K the adsorption coefficient ($L.mg^{-1}$).

$$r = \frac{dC}{dt} = \frac{kKC}{1 + KC} \tag{5.6}$$

Equation (5.6) can be rewritten for highly diluted solutions as expressed in Equation (5.7), where C_0 and C are the pollutant concentrations at the initial time and at a time t ($mg.L^{-1}$), and k_{app} (min^{-1}) is the apparent first-order rate constant.

$$\ln\left(\frac{C}{C_0}\right) = -k_{app}t \tag{5.7}$$

One notices from Equation (5.6) that k_{app} can be inferred by plotting $\ln(C/C_0)$ as a function of time.

The photodegradation of IBP under UVA illumination is displayed in Figure 5.18. The incorporation of TiO_2 into MIL-100(Al) and into the copper trimesate powder enhanced the photodegradation of this drug. Nonetheless, this effect was much more pronounced for MIL-100(Al), as expected since TiO_2 is present at a high concentration and in the form of anatase in this solid. While MIL-100(Al) removed 7% of IBP within 6 hours of illumination, TiO_2@MIL-100 was able to remove 62%. HKUST-1 and TiO_2@Cu-btc removed, at the same time, only 1 and 8%, respectively. Figure 5.18b displays the plot of ln (C/C_0) as a function of time. As expressed in Equation (5.7), k_{app} is given by the slope of this curve. MIL-100(Al) and KHUST-1 have ${k_{app}}_{IBP}$ of around 2.1×10^{-4} and 4.0×10^{-6} min^{-1}, respectively. On the other hand, TiO_2@MIL-100 and TiO_2@Cu-btc have ${k_{app}}_{IBP}$ as high as 5.4×10^{-3} and 3.3×10^{-4} min^{-1}, respectively.

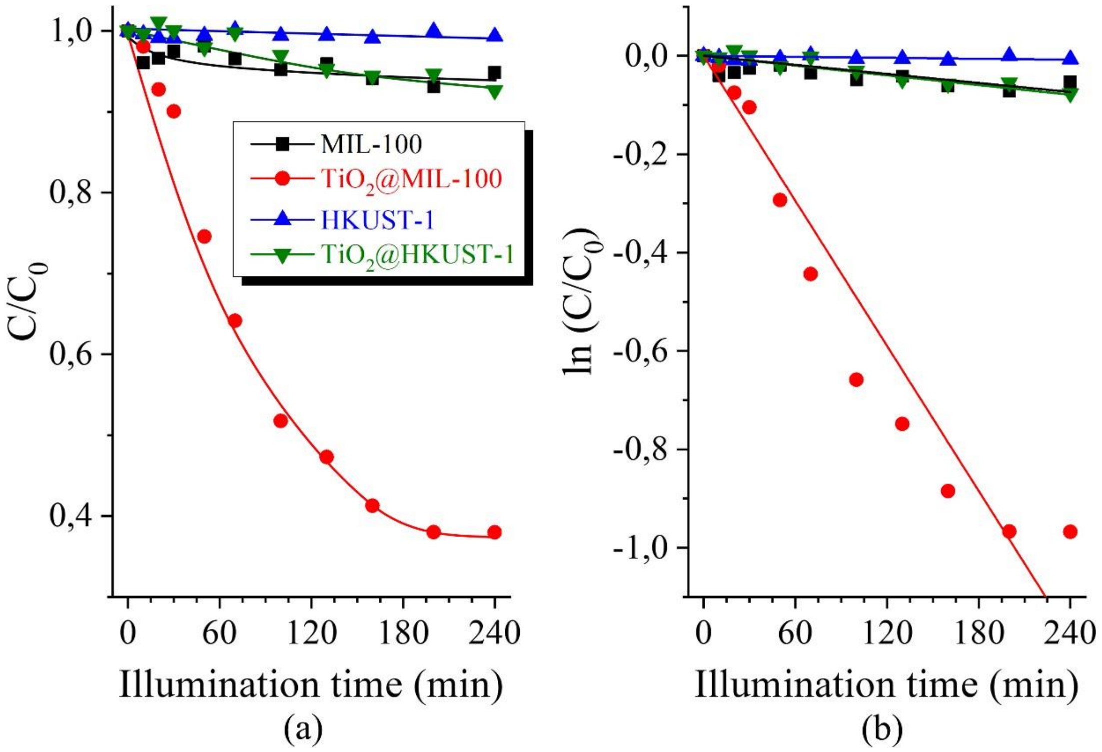

Figure 5.18: (a) C/C$_0$ and (b) ln C/C$_0$ as a function of IBP's illumination time.

Similar behavior was observed on the photodegradation of DIC as displayed in Figure 5.19. MIL-100(Al) and HKUST-1 displayed a $k_{app_{DIC}}$ of around 5.7×10^{-4} and 1.8×10^{-5} min^{-1}, respectively. On the other hand, the modified materials, namely TiO$_2$@MIL-100 and TiO$_2$@Cu-btc, have $k_{app_{DIC}}$ of 3.4×10^{-3} and 4.3×10^{-4} min^{-1}, respectively. In this case, MIL-100 removed 12% of DIC within 6 hours of illumination and TiO$_2$@MIL-100 was able to remove 54%. HKUST-1 and TiO$_2$@Cu-btc removed, at the same time, only 2 and 9%, respectively.

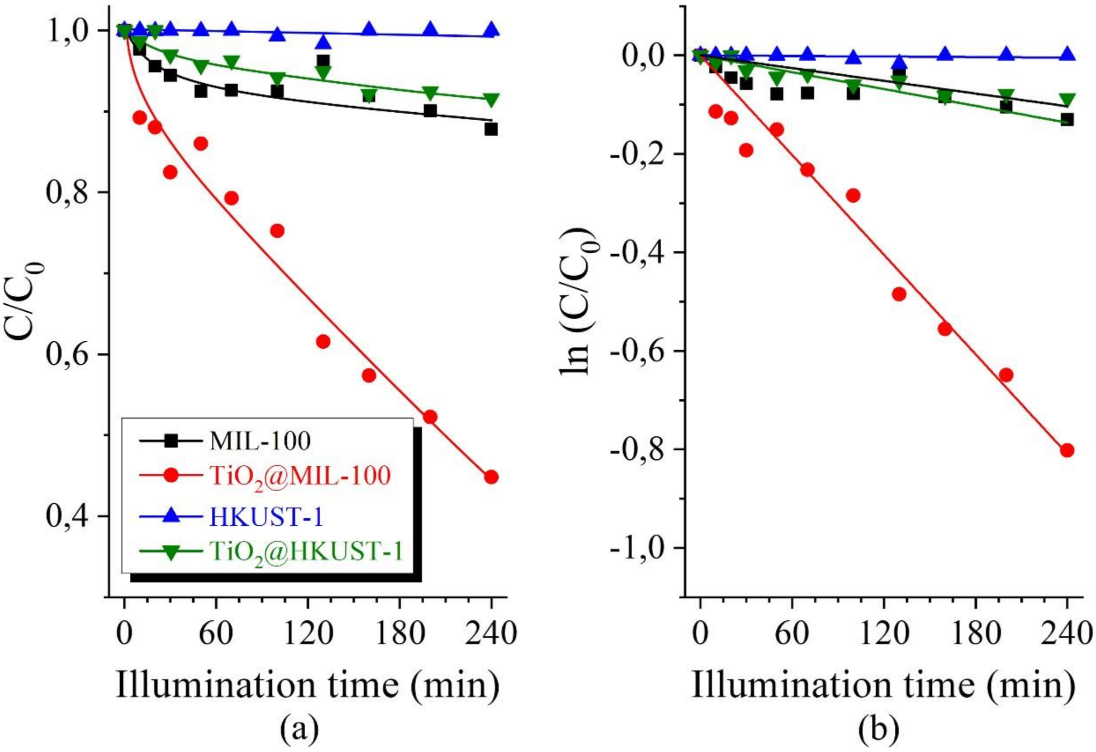

(a) (b)

Figure 5.19: (a) C/C_0 and (b) ln C/C_0 as a function of DIC's illumination time.

In both cases, the composites presented a better photoactivity than the pure MOFs. However, TiO_2@Cu-btc has a much lower photoactivity than TiO_2@MIL-100 which is related to its non- porous structure and, consequentially, to a smaller concentration of titania in this composite,as evidenced by XRD, FTIR, Raman, TG, SEM, and TEM (Figure 5.1 to Figure 5.9). Moreover, XRD and SAED patterns revealed that titania is present as rutile in TiO_2@Cu-btc, which has a lower photocatalytic activity than anatase (main crystalline phase of titania in TiO_2@MIL-100). These properties justify the lower photocatalytic activity of TiO_2@Cu-btccompared to TiO_2@MIL-100. In a further step, we plan to promote chemical etching of TiO_2@MIL-100, aiming to remove MIL-100(Al) and give rise to a thin titania shell. In this way, MIL-100(Al) will play a template role, allowing the preparation of titania samples with high surface areas and photocatalytic activities. The same procedure can be applied with TiO_2@Cu-btc aiming to produce rutile nanoparticles. Studies show that these polymorphic phases can present higher photoactivity when mixed together than separately [159,160]. Suchresults will be reported in future work.

6 CONCLUSIONS

In this work, MIL-100(Al) and HKUST-1 were successfully prepared by hydrothermal treatment. These materials presented surface areas up to 1787 $m^2.g^{-1}$ and were subsequently submitted to a chemical modification step, where the incorporation of sol-gel derived titania gave rise to new composites (TiO_2@MIL-100 and TiO_2@Cu-btc). The MIL-100(Al) withstood this step without displaying a collapse of its crystal structure, as proved by the maintenance of its main XRD peaks (220) and (311). However, due to the hydrolysis of copper-oxygen bonds, HKUST-1's structure did not outstand its chemical modification. Hence, a new non-porous copper-trimesate phase, known as $Cu_2(btc)(OH)(H_2O)$, was formed. In this case, the TiO_2-modified composite, or TiO_2@Cu-btc, presents its main peaks at 2θ about 9.0° and 10.0°. The presence of TiO_2 was observed on both modified MOFs' XRD. TiO_2@MIL-100 presented peaks ascribed to anatase, and TiO_2@Cu-btc to rutile. This evidence could not be supported by the study carried out with FTIR since these two polymorphic phases are not distinguished by this technique. However, Raman spectroscopy revealed band signatures that are ascribed to anatase and rutile in TiO_2@MIL-100 and TiO_2@Cu-btc, respectively. In this case, they are easily distinguished.

TiO_2 nanoparticles were observed by SEM and TEM microscopies anchored on the surface and within MIL-100's framework. SAED pattern confirmed their crystallization as anatase, and EDS chemical mapping revealed that they are distributed preferentially near aluminum sites. It was verified by TG analysis that the loading of titania in this sample was around 68 wt.%. The N_2 sorption tests showed a reduction in the SSA from 1787 to 417 $m^2.g^{-1}$ after titania incorporation. The presence of a higher mesoporosity was also verified on TiO_2@MIL-100, which is related to the collapse of some structural caves during the growth of TiO_2 nanoparticles. EPR results showed that TiO_2@MIL-100 was able to induce the formation of hydroxyl radicals during the UVA illumination. These entities are, in part, responsible for the degradation of IBP and DIC under UVA illumination. Titania insertion led to materials with narrower bandgaps (3.70 against 3.33 eV) and a higher capacity to degrade IBP ($K_{app} = 5.4 \times 10^{-3}$ min^{-1}) and DIC ($K_{app} = 3.4 \times 10^{-3}$ min^{-1}) under UVA illumination in comparison to MIL-100(Al) ($K_{app} = 2.1 \times 10\text{-}4$ and $K_{app} = 5.7 \times 10^{-4}$ for IBP and DIC, respectively). IBP degradation led to the formation of a co-product that was identified as being the p-Isobutyl-phenol, which was confirmed by UV-vis spectra: the characteristic band at 260 nm and the presence of an isosbestic point at 245 nm matches with other literature reports.

Despite the observed structural change in HKUST-1 and the fact that its bandgap (3.33 eV) remained constant after TiO2 incorporation, the process was able to form rutile anchored on the surface of $Cu_2(btc)(OH)(H_2O)$ crystals, as revealed by SEM and TEM microscopies. In this case, the SAED pattern presents rings associated with the (110) plan of rutile, and the EDS chemical mapping showed that titanium is homogeneously distributed along the $Cu_2(btc)(OH)(H_2O)$ crystals. This led to an increase on its K_{app} from 4.0×10^{-6} to 3.3×10^{-4} min^{-1} for IBP and from 1.8×10^{-5} to 4.3×10^{-4} min^{-1} for DIC. TG analysis showed that the loading of titania in this sample was around 9 wt.%. The N_2 sorption tests showed a reduction in the SSA from 1360 to 8 $m^2.g^{-1}$ after titania incorporation, which highlights the non-porosity structure of TiO_2@Cu-btc. EPR results showed that TiO_2@Cu-btc was not able to induce the formation of ROS under UVA illumination. This can be related to the extremely low concentration of rutile in this sample, due to its crystallization only at its surface.

A high crystalline, porous, and photoactive TiO_2@MOF composite was successfully produced through the impregnation of MIL-100 with anatase nanoparticles. It was proved that this material presents a good balance between its SSA and its photocatalytic activity. Moreover, the chemical stability of the sample during TiO_2 insertion was fundamental to this photocatalytic improvement as HKUST-1 did not present the same results due to its modification towards a non-porous copper trimesate. This proves that MOFs can be great candidates to anchor semiconductors' nanoparticles and combine their elevated SSA and photocatalytic properties to create efficient photoactive materials. In further steps, a chemical etching of the TiO_2@MIL-100 is envisaged for the production of highly dispersed anatase nanoparticles. This principle can be extended to TiO_2@Cu-btc to produce rutile nanoparticles.

6 CONCLUSÕES

Neste trabalho, MIL-100 (Al) e HKUST-1 foram preparados com sucesso por tratamento hidrotérmico. Esses materiais apresentaram áreas superficiais de até 1.787 $m^2.g^{-1}$ e foram posteriormente submetidos a uma etapa de modificação química, onde a incorporação do titânia sol-gel deu origem a novos compósitos (TiO_2@MIL-100 e TiO_2@Cu-btc) . O MIL-100(Al) resistiu a esta etapa sem apresentar colapso de sua estrutura cristalina, conforme comprovado pela manutenção de seus principais picos de DRX (220) e (311). No entanto, devido à hidrólise das ligações cobre-oxigênio, a estrutura do HKUST-1 não superou sua modificação química. Assim, uma nova fase de trimesato de cobre, não porosa, conhecida como Cu_2(btc)(OH)(H_2O), foi formada. Nesse caso, o compósito modificado com TiO2, ou TiO2@Cu-btc, apresenta seus picos principais em 2θ cerca de 9,0 ° e 10,0 °. A presença de TiO_2 foi observada no XRD de ambas as MOFs modificadas. TiO_2@MIL-100 apresentou picos atribuídos à fase anatasio e, TiO_2@Cu-btc, ao rutilo. Esta evidência não pôde ser suportada pelo estudo realizado com FTIR, uma vez que estas duas fases polimórficas não são distinguidas por esta técnica. No entanto, a espectroscopia Raman revelou assinaturas de banda que são atribuídas ao anatasio e ao rutilo no TiO_2@MIL-100 e TiO_2@Cu-btc, respectivamente. Nesse caso, eles são facilmente distinguidos.

Nanopartículas de TiO_2 foram observadas por microscopias SEM e TEM ancoradas na superfície e dentro dos cristais do trimesato de alumínio. O padrão SAED confirmou sua cristalização na forma de anatasio e o mapeamento químico feito por EDS revelou que os átomos de Ti estão distribuídos preferencialmente perto dos de alumínio. Foi verificado por análise de TG que o carregamento de titânia nesta amostra foi em torno de 68% em peso. Os testes de sorção de N_2 mostraram redução da SSA de 1787 para 417 $m^2.g^{-1}$ após a incorporação da titânia. A presença de maior mesoporosidade também foi verificada no TiO_2@MIL-100, que está relacionada ao colapso de alguns poros durante o crescimento de nanopartículas de TiO_2. Os resultados de EPR mostraram que TiO_2@MIL-100 foi capaz de induzir a formação de radicais hidroxila durante a iluminação UVA. Essas entidades são, em parte, responsáveis pela degradação do IBP e DIC sob a luz UVA. A inserção de Titânia criou materiais com bandgaps mais estreitos (3,70 contra 3,33 eV) e uma maior capacidade de degradar IBP ($K_{app} = 5{,}4 \times 10^{-3}$ min^{-1}) e DIC ($K_{app} = 3{,}4 \times$ 10-3 min^{-1}) sob iluminação UVA em comparação com MIL-100(Al) ($K_{app} = 2{,}1 \times 10^{-4}$ e $K_{app} = 5{,}7 \times 10^{-4}$ para IBP e DIC, respectivamente). A degradação do IBP levou à formação de um coproduto que foi identificado como sendo o p-isobutil-fenol, o que foi confirmado por espectros de UV-vis: a banda característica em 260 nm e a presença de um ponto isosbéstico em 245 nm coincide com outros relatos da literatura.

Apesar da mudança estrutural observada na HKUST-1 e do fato de seu bandgap (3,33 eV) ter permanecido constante após a incorporação do TiO_2, o processo foi capaz de formar rutilo ancorado na superfície dos cristais de $Cu_2(btc)(OH)(H_2O)$, como revelado por microscopias SEM e TEM. Neste caso, o padrão SAED apresenta anéis associados ao plano (110) do rutilo, e o mapeamento químico com EDS mostrou que o titânio está homogeneamente distribuído ao longo dos cristais de $Cu_2(btc)(OH)(H_2O)$. Isso levou a um aumento em seu K_{app} de $4{,}0 \times 10^{-6}$ para $3{,}3 \times 10^{-4}$ min^{-1} para IBP e de $1{,}8 \times 10^{-5}$ para $4{,}3 \times 10^{-4}$ min^{-1} para DIC. A análise TG mostrou que o carregamento de titânia nesta amostra foi de cerca de 9% em peso. Os testes de sorção de N_2 mostraram uma redução no SSA de 1360 para 8 m^2.g^{-1} após a incorporação da titânia, o que destaca a estrutura não porosa do TiO_2@Cu-btc. Os resultados de EPR mostraram que TiO_2@Cu-btc não foi capaz de induzir a formação de ROS sob iluminação UVA. Isso pode estar relacionado à baixíssima concentração de rutilo nesta amostra, devido à sua cristalização apenas em sua superfície.

Um composto TiO_2@MOF altamente cristalino, poroso e fotoativo foi produzido com sucesso através da impregnação da MIL-100(Al) com nanopartículas de anatasio. Foi comprovado que este material apresenta um bom equilíbrio entre sua SSA e sua atividade fotocatalítica. Além disso, a estabilidade química da amostra durante a inserção do TiO_2 foi fundamental para essa melhora fotocatalítica, pois o HKUST-1 não apresentou os mesmos resultados devido à sua modificação para um trimesato de cobre não poroso. Isso prova que as MOFs podem ser ótimas candidatas para ancorar nanopartículas de semicondutores, combinando suas elevadas SSA e propriedades fotocatalíticas para criar materiais fotoativos eficientes. Em outras etapas, um ataque químico no TiO_2@MIL-100 é considerado para a produção de nanopartículas de anatasio altamente dispersas. Este princípio pode ser estendido ao TiO_2@Cu-btc para produzir nanopartículas de rutilo.

7 ACKNOWLEDGEMENTS

We thank the financial support from CNPq (305013/2017-3 and 301423/2018), CAPES (PROEX), FAPEMIG (APQ-00792-17/red-00102-16), and PRPq-UFMG (05/2020). UFMG Microscopy Center, LEPCom (prof. Rodrigo Oréfice), and PMEL are acknowledged for the support provided in TEM, UV-Vis, and SEM tests, respectively. Research units UCCS and LASIRe as well as the University of Lille and Central Lille are recognized for their cooperationduring this work.

8 BIBLIOGRAPHICAL REFERENCES

[1] Albadarin AB, Collins MN, Naushad M, Shirazian S, Walker G, Mangwandi C. Activated lignin-chitosan extruded blends for efficient adsorption of methylene blue. Chem Eng J 2017;307:264–72. https://doi.org/10.1016/j.cej.2016.08.089.

[2] Hossain L, Sarker SK, Khan MS. Evaluation of present and future wastewater impacts of textile dyeing industries in Bangladesh. Environ Dev 2018;26:23–33. https://doi.org/10.1016/j.envdev.2018.03.005.

[3] Tajra A. Governo libera 51 agrotóxicos e totaliza 290 substâncias autorizadas no ano 2019.

[4] Dasgupta S, Mamingi N, Meisner C. Pesticide use in Brazil in the era of agroindustrialization and globalization. Environ Dev Econ 2001;6:459–82. https://doi.org/10.1017/S1355770X01000262.

[5] Araujo ACP, Telles DL, Gorni R, Lima LLA. Organochlorine pesticide contamination in the ipojuca basin, brazil. Environ Technol (United Kingdom) 1998;19:109–13. https://doi.org/10.1080/09593331908616662.

[6] Dores EFGC, Carbo L, Ribeiro ML, De-Lamonica-Freire EM. Pesticide levels in ground and surface waters of primavera do Leste Region, Mato Grosso, Brazil. J Chromatogr Sci 2008;46:585–90. https://doi.org/10.1093/chromsci/46.7.585.

[7] Azevedo AL. Acidente em Mariana é o maior da história com barragem de rejeitos. O Globo 2015. https://oglobo.globo.com/brasil/acidente-em-mariana-o-maior-da-historia-com-barragens-de-rejeitos-18067899 (accessed December 6, 2020).

[8] Cagnin RC, Quaresma VS, Chaillou G, Franco T, Bastos AC. Arsenic enrichment in sediment on the eastern continental shelf of Brazil. Sci Total Environ 2017;607–608:304–16. https://doi.org/10.1016/j.scitotenv.2017.06.162.

[9] Brumadinho ainda enterra seus mortos oito meses após rompimento de barragem. J Nac 2019. https://g1.globo.com/jornal-nacional/noticia/2019/09/30/brumadinho-ainda-enterra-seus-mortos-8-meses-apos-rompimento-de-barragem.ghtml (accessed December 6, 2020).

[10] Freitas R, Fiúza P, Costa D. Com impactos na agricultura, mineração e turismo, tragédia da Vale traz incertezas para futuro da economia de Brumadinho. G1 2019. https://g1.globo.com/mg/minas-gerais/noticia/2019/07/24/com-impactos-na-

agricultura-mineracao-e-turismo-tragedia-da-vale-traz-incertezas-para-futuro-da-economia-de-brumadinho.ghtml.

[11] Quadra GR, Silva PSA, Paranaíba JR, Josué IIP, Souza H, Costa R, et al. Investigation of medicines consumption and disposal in Brazil: A study case in a developing country. Sci Total Environ 2019;671:505–9. https://doi.org/10.1016/j.scitotenv.2019.03.334.

[12] aus der Beek T, Weber FA, Bergmann A, Hickmann S, Ebert I, Hein A, et al. Pharmaceuticals in the environment-Global occurrences and perspectives. Environ Toxicol Chem 2016;35:823–35. https://doi.org/10.1002/etc.3339.

[13] Wang J, Zhao S qi, Zhang M ya, He B shu. Targeted eco-pharmacovigilance for ketoprofen in the environment: Need, strategy and challenge. Chemosphere 2018;194:450–62. https://doi.org/10.1016/j.chemosphere.2017.12.020.

[14] Fast C. Resíduos de drogas e hormônios na água preocupam cientistas. UFRGS 2017. http://www.ufrgs.br/secom/ciencia/residuos-de-medicamentos-e-hormonios-na-agua-preocupam-cientistas/ (accessed October 7, 2019).

[15] Yang DA, Cho HY, Kim J, Yang ST, Ahn WS. CO2 capture and conversion using Mg-MOF-74 prepared by a sonochemical method. Energy Environ Sci 2012;5:6465–73. https://doi.org/10.1039/c1ee02234b.

[16] Yu J, Mu C, Yan B, Qin X, Shen C, Xue H, et al. Nanoparticle/MOF composites: Preparations and applications. Mater Horizons 2017;4:557–69. https://doi.org/10.1039/c6mh00586a.

[17] Chebbi M, Azambre B, Volkringer C, Loiseau T. Dynamic sorption properties of Metal-Organic Frameworks for the capture of methyl iodide. Microporous Mesoporous Mater 2018;259:244–54. https://doi.org/10.1016/j.micromeso.2017.10.018.

[18] Zamaro JM, Pérez NC, Miró EE, Casado C, Seoane B, Téllez C, et al. HKUST-1 MOF: A matrix to synthesize CuO and CuO-CeO 2 nanoparticle catalysts for CO oxidation. Chem Eng J 2012;195–196:180–7. https://doi.org/10.1016/j.cej.2012.04.091.

[19] Li SL, Xu Q. Metal-organic frameworks as platforms for clean energy. Energy Environ Sci 2013;6:1656–83. https://doi.org/10.1039/c3ee40507a.

[20] Férey G. Hybrid porous solids: Past, present, future. Chem Soc Rev 2008;37:191–214.

https://doi.org/10.1039/b618320b.

[21] Chen Q, He Q, Lv M, Xu Y, Yang H, Liu X, et al. Selective adsorption of cationic dyes by UiO-66-NH 2. Appl Surf Sci 2015;327:77–85. https://doi.org/10.1016/j.apsusc.2014.11.103.

[22] Assaad T, Assfour B. Metal organic framework MIL-101 for radioiodine capture and storage. J Nucl Mater 2017;493:6–11. https://doi.org/10.1016/j.jnucmat.2017.05.036.

[23] Bai Y, Dou Y, Xie LH, Rutledge W, Li JR, Zhou HC. Zr-based metal-organic frameworks: Design, synthesis, structure, and applications. Chem Soc Rev 2016;45:2327–67. https://doi.org/10.1039/c5cs00837a.

[24] Wang TC, Bury W, Gómez-Gualdrón DA, Vermeulen NA, Mondloch JE, Deria P, et al. Ultrahigh Surface Area Zirconium MOFs and Insights into the Applicability of the BET Theory. J Am Chem Soc 2015;137:3585–91. https://doi.org/10.1021/ja512973b.

[25] Kong C, Du H, Chen L, Chen B. Nanoscale MOF/organosilica membranes on tubular ceramic substrates for highly selective gas separation. Energy Environ Sci 2017;10:1812–9. https://doi.org/10.1039/c7ee00830a.

[26] Ökte AN, Karamanis D, Chalkia E, Tuncel D. The effect of ZnO or TiO2 loaded nanoparticles on the adsorption and photocatalytic performance of Cu-BTC and ZIF-8 MOFs. Mater Chem Phys 2017;187:5–10. https://doi.org/10.1016/j.matchemphys.2016.11.059.

[27] Li Y, Pang A, Wang C, Wei M. Metal-organic frameworks: Promising materials for improving the open circuit voltage of dye-sensitized solar cells. J Mater Chem 2011;21:17259–64. https://doi.org/10.1039/c1jm12754c.

[28] Wang H, Yu T, Tan X, Zhang H, Li P, Liu H, et al. Enhanced Photocatalytic Oxidation of Isopropanol by HKUST-1@TiO 2 Core-Shell Structure with Ultrathin Anatase Porous Shell: Toxic Intermediate Control. Ind Eng Chem Res 2016;55:8096–103. https://doi.org/10.1021/acs.iecr.6b01400.

[29] Gu Y, Wu YN, Shen J, Li Z, Chen S, Lu H, et al. Turning Redundant Ligands into Treasure: A New Strategy for Constructing MIL-53(Al)@Nanoscale TiO2 Layers. Chem - A Eur J 2015;21:17485–90. https://doi.org/10.1002/chem.201503052.

[30] Hu Y, Huang Z, Zhou L, Wang D, Li G. Synthesis of nanoscale titania embedded in MIL-101 for the adsorption and degradation of volatile pollutants with thermal desorption gas chromatography and mass spectrometry detection. J Sep Sci

2014;37:1482–8. https://doi.org/10.1002/jssc.201400100.

[31] Gonçalves BS, Souza TCC de, Castro VG de, Silva GG, Houmard M, Nunes EHM. Solvent effect on the structure and photocatalytic behavior of TiO2-RGO nanocomposites. To Be Publ 2019:1–13. https://doi.org/10.1557/jmr.2019.342.

[32] Malekshahi Byranvand M, Nemati Kharat A, Fatholahi L, Malekshahi Beiranvand Z. A Review on Synthesis of Nano-TiO2 via Different Methods. J Nanostructures 2013;3:1–9. https://doi.org/10.7508/jns.2013.01.001.

[33] Gonçalves BS, Palhares HG, Souza TCCD, Castro VGD, Silva GG, Silva BC, et al. Effect of the carbon loading on the structural and photocatalytic properties of reduced graphene oxide-TiO2 nanocomposites prepared by hydrothermal synthesis. J Mater Res Technol 2019;8:6262–74. https://doi.org/10.1016/j.jmrt.2019.10.020.

[34] Guo Z, Ma R, Li G. Degradation of phenol by nanomaterial TiO2 in wastewater. Chem Eng J 2006;119:55–9. https://doi.org/10.1016/j.cej.2006.01.017.

[35] Volkringer C, Popov D, Loiseau T, Férey G, Burghammer M, Riekel C, et al. Synthesis, single-crystal X-ray microdiffraction, and NMR characterizations of the giant pore metal-organic framework aluminum trimesate MIL-100. Chem Mater 2009;21:5695–7. https://doi.org/10.1021/cm901983a.

[36] Lin KS, Adhikari AK, Ku CN, Chiang CL, Kuo H. Synthesis and characterization of porous HKUST-1 metal organic frameworks for hydrogen storage. Int. J. Hydrogen Energy, vol. 37, 2012, p. 13865–71. https://doi.org/10.1016/j.ijhydene.2012.04.105.

[37] Jeremias F, Khutia A, Henninger SK, Janiak C. MIL-100(Al, Fe) as water adsorbents for heat transformation purposes - A promising application. J Mater Chem 2012;22:10148–51. https://doi.org/10.1039/c2jm15615f.

[38] Álvarez JR, Sánchez-González E, Pérez E, Schneider-Revueltas E, Martínez A, Tejeda-Cruz A, et al. Structure stability of HKUST-1 towards water and ethanol and their effect on its CO2 capture properties. Dalt Trans 2017;46:9192–200. https://doi.org/10.1039/c7dt01845b.

[39] Harada M. Harada1995. Crit Rev Toxicol 1995;25:1–24. https://doi.org/10.3109/10408449509089885.

[40] Greenstone M, Hanna R. Environmental regulations, air and water pollution, and infant mortality in India. Am Econ Rev 2014;104:3038–72. https://doi.org/10.1257/aer.104.10.3038.

[41] Karn SK, Harada H. Surface water pollution in three urban territories of Nepal, India, and Bangladesh. Environ Manage 2001;28:483–96. https://doi.org/10.1007/s002670010238.

[42] Carvalho MS de, Moreira RM, Ribeiro KD, Almeida AM de. Concentração de metais no rio Doce em Mariana , Minas Gerais , Brasil Concentration of metals in the Doce river in Mariana , Minas Gerais , Brazil. Acta Bras 2017;1:37–41.

[43] Morales LA. New England Watersheds: A Data Driven Portrait of Water Pollution in the North Eastern United States. Elements 2018;13. https://doi.org/10.6017/eurj.v13i2.9956.

[44] Audry S, Schäfer J, Blanc G, Jouanneau JM. Fifty-year sedimentary record of heavy metal pollution (Cd, Zn, Cu, Pb) in the Lot River reservoirs (France). Environ Pollut 2004;132:413–26. https://doi.org/10.1016/j.envpol.2004.05.025.

[45] Hama Aziz KH, Miessner H, Mueller S, Kalass D, Moeller D, Khorshid I, et al. Degradation of pharmaceutical diclofenac and ibuprofen in aqueous solution, a direct comparison of ozonation, photocatalysis, and non-thermal plasma. Chem Eng J 2017;313:1033–41. https://doi.org/10.1016/j.cej.2016.10.137.

[46] Monna F, Lancelot J, Croudace IW, Cundy AB, Lewis JT. Pb isotopic composition of airborne particulate material from France and the Southern United Kingdom: Implications for Pb pollution sources in urban areas. Environ Sci Technol 1997;31:2277–86. https://doi.org/10.1021/es960870+.

[47] Gadipelly C, Pérez-González A, Yadav GD, Ortiz I, Ibáñez R, Rathod VK, et al. Pharmaceutical industry wastewater: Review of the technologies for water treatment and reuse. Ind Eng Chem Res 2014;53:11571–92. https://doi.org/10.1021/ie501210j.

[48] Khan NA, Hasan Z, Jhung SH. Adsorptive removal of hazardous materials using metal-organic frameworks (MOFs): A review. J Hazard Mater 2013;244–245:444–56. https://doi.org/10.1016/j.jhazmat.2012.11.011.

[49] Empresa têxtil de Joinville é multada por crime ambiental e poluição de rio. G1 2012. http://g1.globo.com/sc/santa-catarina/noticia/2012/07/empresa-textil-de-joinville-e-multada-por-crime-ambiental-e-poluicao-de-rio.html (accessed December 6, 2020).

[50] Holkar CR, Jadhav AJ, Pinjari D V., Mahamuni NM, Pandit AB. A critical review on textile wastewater treatments: Possible approaches. J Environ Manage 2016;182:351–66. https://doi.org/10.1016/j.jenvman.2016.07.090.

[51] Mathur N, Bhatnagar P, Nagar P, Bijarnia MK. Mutagenicity assessment of effluents from textile/dye industries of Sanganer, Jaipur (India): A case study. Ecotoxicol Environ Saf 2005;61:105–13. https://doi.org/10.1016/j.ecoenv.2004.08.003.

[52] Jing HP, Wang CC, Zhang YW, Wang P, Li R. Photocatalytic degradation of methylene blue in ZIF-8. RSC Adv 2014;4:54454–62. https://doi.org/10.1039/c4ra08820d.

[53] Jones OAH, Voulvoulis N, Lester JN. Human pharmaceuticals in the aquatic environment a review. Environ Technol (United Kingdom) 2001;22:1383–94. https://doi.org/10.1080/09593330.2001.11090873.

[54] Onesios KM, Yu JT, Bouwer EJ. Biodegradation and removal of pharmaceuticals and personal care products in treatment systems: A review. Biodegradation 2009;20:441–66. https://doi.org/10.1007/s10532-008-9237-8.

[55] Zhang D, Gersberg RM, Ng WJ, Tan SK. Removal of pharmaceuticals and personal care products in aquatic plant-based systems: A review. Environ Pollut 2014;184:620–39. https://doi.org/10.1016/j.envpol.2013.09.009.

[56] Jung C, Son A, Her N, Zoh KD, Cho J, Yoon Y. Removal of endocrine disrupting compounds, pharmaceuticals, and personal care products in water using carbon nanotubes: A review. J Ind Eng Chem 2015;27:1–11. https://doi.org/10.1016/j.jiec.2014.12.035.

[57] Carmalin Sophia A, Lima EC, Allaudeen N, Rajan S. Application of graphene based materials for adsorption of pharmaceutical traces from water and wastewater- a review. Desalin Water Treat 2016;57:27573–86. https://doi.org/10.1080/19443994.2016.1172989.

[58] Patrolecco L, Capri S, Ademollo N. Occurrence of selected pharmaceuticals in the principal sewage treatment plants in Rome (Italy) and in the receiving surface waters. Environ Sci Pollut Res 2015;22:5864–76. https://doi.org/10.1007/s11356-014-3765-z.

[59] Han S, Choi K, Kim J, Ji K, Kim S, Ahn B, et al. Endocrine disruption and consequences of chronic exposure to ibuprofen in Japanese medaka (Oryzias latipes) and freshwater cladocerans Daphnia magna and Moina macrocopa. Aquat Toxicol 2010;98:256–64. https://doi.org/10.1016/j.aquatox.2010.02.013.

[60] Lee J, Ji K, Lim Kho Y, Kim P, Choi K. Chronic exposure to diclofenac on two

freshwater cladocerans and Japanese medaka. Ecotoxicol Environ Saf 2011;74:1216–25. https://doi.org/10.1016/j.ecoenv.2011.03.014.

[61] Iovino P, Chianese S, Canzano S, Prisciandaro M, Musmarra D. Ibuprofen photodegradation in aqueous solutions. Environ Sci Pollut Res 2016;23:22993–3004. https://doi.org/10.1007/s11356-016-7339-0.

[62] Padilla Villavicencio M, Escobedo Morales A, Ruiz Peralta M de L, Sánchez-Cantú M, Rojas Blanco L, Chigo Anota E, et al. Ibuprofen Photodegradation by Ag2O and Ag/Ag2O Composites Under Simulated Visible Light Irradiation. Catal Letters 2020;150:2385–99. https://doi.org/10.1007/s10562-020-03139-6.

[63] Musa KAK, Eriksson LA. Theoretical study of ibuprofen phototoxicity. J Phys Chem B 2007;111:13345–52. https://doi.org/10.1021/jp076553e.

[64] Nadais H, Li X, Alves N, Couras C, Andersen HR, Angelidaki I, et al. Bio-electro-Fenton process for the degradation of Non-Steroidal Anti-Inflammatory Drugs in wastewater. Chem Eng J 2018;338:401–10. https://doi.org/10.1016/j.cej.2018.01.014.

[65] Rabiet M, Togola A, Brissaud F, Seidel JL, Budzinski H, Elbaz-Poulichet F. Consequences of treated water recycling as regards pharmaceuticals and drugs in surface and ground waters of a medium-sized mediterranean catchment. Environ Sci Technol 2006;40:5282–8. https://doi.org/10.1021/es060528p.

[66] Zhang N, Liu G, Liu H, Wang Y, He Z, Wang G. Diclofenac photodegradation under simulated sunlight: Effect of different forms of nitrogen and Kinetics. J Hazard Mater 2011;192:411–8. https://doi.org/10.1016/j.jhazmat.2011.05.038.

[67] Escapa C, Coimbra RN, Paniagua S, García AI, Otero M. Comparative assessment of diclofenac removal from water by different microalgae strains. Algal Res 2016;18:127–34. https://doi.org/10.1016/j.algal.2016.06.008.

[68] Song S, Su Y, Adeleye AS, Zhang Y, Zhou X. Optimal design and characterization of sulfide-modified nanoscale zerovalent iron for diclofenac removal. Appl Catal B Environ 2017;201:211–20. https://doi.org/10.1016/j.apcatb.2016.07.055.

[69] Mestre AS, Pires J, Nogueira JMF, Carvalho AP. Activated carbons for the adsorption of ibuprofen. Carbon N Y 2007;45:1979–88. https://doi.org/10.1016/j.carbon.2007.06.005.

[70] Azimi A, Azari A, Rezakazemi M, Ansarpour M. Removal of Heavy Metals from Industrial Wastewaters: A Review. ChemBioEng Rev 2017;4:37–59.

https://doi.org/10.1002/cben.201600010.

[71] Forgacs E, Cserháti T, Oros G. Removal of synthetic dyes from wastewaters: A review. Environ Int 2004;30:953–71. https://doi.org/10.1016/j.envint.2004.02.001.

[72] Demirbas A. Agricultural based activated carbons for the removal of dyes from aqueous solutions: A review. J Hazard Mater 2009;167:1–9. https://doi.org/10.1016/j.jhazmat.2008.12.114.

[73] Singh K, Arora S. Removal of synthetic textile dyes from wastewaters: A critical review on present treatment technologies. Crit Rev Environ Sci Technol 2011;41:807–78. https://doi.org/10.1080/10643380903218376.

[74] Tijani JO, Fatoba OO, Madzivire G, Petrik LF. A review of combined advanced oxidation technologies for the removal of organic pollutants from water. Water Air Soil Pollut 2014;225. https://doi.org/10.1007/s11270-014-2102-y.

[75] Ali I, Asim M, Khan TA. Low cost adsorbents for the removal of organic pollutants from wastewater. J Environ Manage 2012;113:170–83. https://doi.org/10.1016/j.jenvman.2012.08.028.

[76] Aksu Z. Application of biosorption for the removal of organic pollutants: A review. Process Biochem 2005;40:997–1026. https://doi.org/10.1016/j.procbio.2004.04.008.

[77] Ding F, Yakobson BI. Challenges in hydrogen adsorptions: From physisorption to chemisorption. Front Phys 2011;6:142–50. https://doi.org/10.1007/s11467-011-0171-6.

[78] Morimoto T, Nagao M, Tokuda F. The relation between the amounts of chemisorbed and physisorbed water on metal oxides. J Phys Chem 1969;73:243–8. https://doi.org/10.1021/j100721a039.

[79] Bhadra BN, Seo PW, Jhung SH. Adsorption of diclofenac sodium from water using oxidized activated carbon. Chem Eng J 2016;301:27–34. https://doi.org/10.1016/j.cej.2016.04.143.

[80] Bhadra BN, Ahmed I, Kim S, Jhung SH. Adsorptive removal of ibuprofen and diclofenac from water using metal-organic framework-derived porous carbon. Chem Eng J 2017;314:50–8. https://doi.org/10.1016/j.cej.2016.12.127.

[81] Yagub MT, Sen TK, Afroze S, Ang HM. Dye and its removal from aqueous solution by adsorption: A review. Adv Colloid Interface Sci 2014;209:172–84. https://doi.org/10.1016/j.cis.2014.04.002.

[82] Marques FC, Stumbo AM, Canela MC. EstratÉGias e materiais utilizados em fotocatÁlise heterogÊnea para geraÇÃo de hidrogÊnio atravÉs da fotÓlise da Água. Quim Nova 2017;40:561–71. https://doi.org/10.21577/0100-4042.20170015.

[83] H JL. International Commission on Atomic Weights. Science (80-) 1900;12:346–7. https://doi.org/10.1126/science.12.296.346-a.

[84] Fox MA, Dulay MT. Heterogeneous Photocatalysis. Chem Rev 1993;93:341–57. https://doi.org/10.1021/cr00017a016.

[85] MILLS A, DAVIES RH, WORSLEY D. ChemInform Abstract: Water Purification by Semiconductor Photocatalysis. ChemInform 2010;25:no-no. https://doi.org/10.1002/chin.199412335.

[86] Baccaro A, Gutz I. Fotoeletrocatálise Em Semicondutores: Dos Princípios Básicos Até Sua Conformação À Nanoescala. Quim Nova 2017;41:326–39. https://doi.org/10.21577/0100-4042.20170174.

[87] Hoffmann MR, Martin ST, Choi W, Bahnemann DW. Environmental Applications of Semiconductor Photocatalysis. Chem Rev 1995;95:69–96. https://doi.org/10.1021/cr00033a004.

[88] Konstantinou IK, Albanis TA. TiO2-assisted photocatalytic degradation of azo dyes in aqueous solution: Kinetic and mechanistic investigations: A review. Appl Catal B Environ 2004;49:1–14. https://doi.org/10.1016/j.apcatb.2003.11.010.

[89] Fujishima A, Zhang X, Tryk DA. TiO2 photocatalysis and related surface phenomena. Surf Sci Rep 2008;63:515–82. https://doi.org/10.1016/j.surfrep.2008.10.001.

[90] Dias EM, Petit C. Towards the use of metal-organic frameworks for water reuse: A review of the recent advances in the field of organic pollutants removal and degradation and the next steps in the field. J Mater Chem A 2015;3:22484–506. https://doi.org/10.1039/c5ta05440k.

[91] Deng X, Li Z, García H. Visible Light Induced Organic Transformations Using Metal-Organic-Frameworks (MOFs). Chem - A Eur J 2017;23:11189–209. https://doi.org/10.1002/chem.201701460.

[92] Janiak C, Vieth JK. MOFs, MILs and more: Concepts, properties and applications for porous coordination networks (PCNs). New J Chem 2010;34:2366–88. https://doi.org/10.1039/c0nj00275e.

[93] Margeta K, Logar NZ, Šiljeg M, Anamarija F. Natural Zeolites in Water Treatment –

How Effective is Their Use. Water Treat 2013;5:81–112.

[94] Silva P, Vilela SMF, Tomé JPC, Almeida Paz FA. Multifunctional metal-organic frameworks: From academia to industrial applications. Chem Soc Rev 2015;44:6774–803. https://doi.org/10.1039/c5cs00307e.

[95] Férey G. Building units design and scale chemistry. J Solid State Chem 2000;152:37–48. https://doi.org/10.1006/jssc.2000.8667.

[96] O'Keeffe M, Eddaoudi M, Li H, Reineke T, Yaghi OM. Frameworks for extended solids: Geometrical design principles. J Solid State Chem 2000;152:3–20. https://doi.org/10.1006/jssc.2000.8723.

[97] Kim M, Cahill JF, Fei H, Prather KA, Cohen SM. Postsynthetic Ligand and Cation Exchange in Robust Metal-Organic Frameworks. J Am Chem Soc 2012;134:18082–8. https://doi.org/10.1021/ja3079219.

[98] Howarth AJ, Liu Y, Li P, Li Z, Wang TC, Hupp JT, et al. Chemical, thermal and mechanical stabilities of metal-organic frameworks. Nat Rev Mater 2016;1:1–15. https://doi.org/10.1038/natrevmats.2015.18.

[99] Volkringer C, Falaise C, Devaux P, Giovine R, Stevenson V, Pourpoint F, et al. Stability of metal-organic frameworks under gamma irradiation. Chem Commun 2016;52:12502–5. https://doi.org/10.1039/c6cc06878b.

[100] Volkringer C, Loiseau T, Guillou N, Férey G, Elkaïm E, Vimont A. XRD and IR structural investigations of a particular breathing effect in the MOF-type gallium terephthalate MIL-53(Ga). J Chem Soc Dalt Trans 2009;53:2241–9. https://doi.org/10.1039/b817563b.

[101] Huo SH, Yan XP. Metal-organic framework MIL-100(Fe) for the adsorption of malachite green from aqueous solution. J Mater Chem 2012;22:7449–55. https://doi.org/10.1039/c2jm16513a.

[102] Munn AS, Millange F, Frigoli M, Guillou N, Falaise C, Stevenson V, et al. Iodine sequestration by thiol-modified MIL-53(Al). CrystEngComm 2016;18:8108–14. https://doi.org/10.1039/c6ce01842d.

[103] Ke F, Qiu LG, Yuan YP, Peng FM, Jiang X, Xie AJ, et al. Thiol-functionalization of metal-organic framework by a facile coordination-based postsynthetic strategy and enhanced removal of Hg 2+ from water. J Hazard Mater 2011;196:36–43. https://doi.org/10.1016/j.jhazmat.2011.08.069.

[104] Merrifield JD, Davids WG, MacRae JD, Amirbahman A. Uptake of mercury by thiol-grafted chitosan gel beads. Water Res 2004;38:3132–8. https://doi.org/10.1016/j.watres.2004.04.008.

[105] Mai FD, Lu CS, Wu CW, Huang CH, Chen JY, Chen CC. Mechanisms of photocatalytic degradation of Victoria Blue R using nano-TiO2. Sep Purif Technol 2008;62:423–36. https://doi.org/10.1016/j.seppur.2008.02.006.

[106] Lee KM, Lai CW, Ngai KS, Juan JC. Recent developments of zinc oxide based photocatalyst in water treatment technology: A review. vol. 88. Elsevier Ltd; 2016. https://doi.org/10.1016/j.watres.2015.09.045.

[107] Wang H, Yu T, Tan X, Zhang H, Li P, Liu H, et al. Enhanced Photocatalytic Oxidation of Isopropanol by HKUST-1@TiO2 Core-Shell Structure with Ultrathin Anatase Porous Shell: Toxic Intermediate Control. Ind Eng Chem Res 2016;55:8096–103. https://doi.org/10.1021/acs.iecr.6b01400.

[108] Vinogradov A V., Zaake-Hertling H, Hey-Hawkins E, Agafonov A V., Seisenbaeva GA, Kessler VG, et al. The first depleted heterojunction TiO2–MOF-based solar cell.Chem Commun 2014;50:10210–3. https://doi.org/10.1039/c4cc01978d.

[109] Ramasubbu V, Alwin S, Mothi EM, Sahaya Shajan X. TiO2 aerogel–Cu-BTC metal-organic framework composites for enhanced photon absorption. Mater Lett 2017;197:236–40. https://doi.org/10.1016/j.matlet.2017.03.132.

[110] Hanaor DAH, Sorrell CC. Review of the anatase to rutile phase transformation. J Mater Sci 2011;46:855–74. https://doi.org/10.1007/s10853-010-5113-0.

[111] Palhares HG, Gonçalves BS, Silva LMC, Nunes EHM, Houmard M. Clarifying the roles of hydrothermal treatment and silica addition to synthesize TiO2-based nanocomposites with high photocatalytic performance. J Sol-Gel Sci Technol 2020;95:119–35. https://doi.org/10.1007/s10971-020-05265-4.

[112] López R, Gómez R. Band-gap energy estimation from diffuse reflectance measurements on sol-gel and commercial TiO 2: A comparative study. J Sol-Gel Sci Technol 2012;61:1–7. https://doi.org/10.1007/s10971-011-2582-9.

[113] Diaz-Uribe C, Vallejo W, Ramos W. Methylene blue photocatalytic mineralization under visibleirradiation on TiO 2 thin films doped with chromium. Appl Surf Sci 2014;319:121–7. https://doi.org/10.1016/j.apsusc.2014.06.157.

[114] Haouas M, Volkringer C, Loiseau T, Férey G, Taulelle F. In situ NMR, ex situ XRD

and SEM study of the hydrothermal crystallization of nanoporous aluminum trimesates MIL-96, MIL-100, and MIL-110. Chem Mater 2012;24:2462–71. https://doi.org/10.1021/cm300439e.

[115] Loera-Serna S, Oliver-Tolentino MA, de Lourdes López-Núñez M, Santana-Cruz A, Guzmán-Vargas A, Cabrera-Sierra R, et al. Electrochemical behavior of [Cu3(BTC)2] metal–organic framework: The effect of the method of synthesis. J Alloys Compd 2012;540:113–20. https://doi.org/https://doi.org/10.1016/j.jallcom.2012.06.030.

[116] Giovine R, Pourpoint F, Duval S, Lafon O, Amoureux JP, Loiseau T, et al. The Surprising Stability of Cu3(btc)2 Metal-Organic Framework under Steam Flow at High Temperature. Cryst Growth Des 2018;18:6681–93. https://doi.org/10.1021/acs.cgd.8b00931.

[117] Palhares HG, Gonçalves BS, Silva LMC, Nunes EHM, Houmard M. Clarifying the roles of hydrothermal treatment and silica addition to synthesize TiO2-based nanocomposites with high photocatalytic performance. J Sol-Gel Sci Technol 2020;95:119–35. https://doi.org/10.1007/s10971-020-05265-4.

[118] Fischer K, Gawel A, Rosen D, Krause M, Latif AA, Griebel J, et al. Low-temperature synthesis of anatase/rutile/brookite TiO2 nanoparticles on a polymer membrane for photocatalysis. Catalysts 2017;7. https://doi.org/10.3390/catal7070209.

[119] Cheng H, Ma J, Zhao Z, Qi L. Hydrothermal Preparation of Uniform Nanosize Rutile and Anatase Particles. Chem Mater 1995;7:663–71. https://doi.org/10.1021/cm00052a010.

[120] Xu M, Gao Y, Moreno EM, Kunst M, Muhler M, Wang Y, et al. Photocatalytic activity of bulk TiO2 anatase and rutile single crystals using infrared absorption spectroscopy. Phys Rev Lett 2011;106:138302(1)-138302(4). https://doi.org/10.1103/PhysRevLett.106.138302.

[121] Zhang J, Zhou P, Liu J, Yu J. New understanding of the difference of photocatalytic activity among anatase, rutile and brookite TiO2. Phys Chem Chem Phys 2014;16:20382–6. https://doi.org/10.1039/c4cp02201g.

[122] Xu F, Yu Y, Yan J, Xia Q, Wang H, Li J, et al. Ultrafast room temperature synthesis of GrO@HKUST-1 composites with high CO2 adsorption capacity and CO2/N2 adsorption selectivity. Chem Eng J 2016;303:231–7. https://doi.org/10.1016/j.cej.2016.05.143.

[123] Feng Y, Wang C, Ke F, Zang J, Zhu J. MIL-100(Al) gels as an excellent platform loaded with doxorubicin hydrochloride for pH-triggered drug release and anticancer effect. Nanomaterials 2018;8:446. https://doi.org/10.3390/nano8060446.

[124] Ye R-P, Lin L, Chen C-C, Yang J-X, Li F, Zhang X, et al. Synthesis of robust MOF-derived Cu/SiO2 catalyst with low copper loading via sol-gel method for the dimethyl oxalate hydrogenation reaction. ACS Catal 2018;8:3382–94. https://doi.org/10.1021/acscatal.8b00501.

[125] Crişan M, Brăileanu A, Răileanu M, Zaharescu M, Crişan D, Drăgan N, et al. Sol-gel S-doped TiO2 materials for environmental protection. J Non Cryst Solids 2008;354:705–11. https://doi.org/10.1016/j.jnoncrysol.2007.07.083.

[126] Vasconcelos DCL, Nunes EHM, Sabioni ACS, Vasconcelos PMP, Vasconcelos WL. Optical characterization of 316L stainless steel coated with sol-gel titania. J Non Cryst Solids 2012;358. https://doi.org/10.1016/j.jnoncrysol.2012.07.035.

[127] Yang J, Peterlik H, Lomoschitz M, Schubert U. Preparation of mesoporous titania by surfactant-assisted sol-gel processing of acetaldoxime-modified titanium alkoxides. J Non Cryst Solids 2010;356:1217–27. https://doi.org/10.1016/j.jnoncrysol.2010.04.035.

[128] Worrall SD, Bissett MA, Hill PI, Rooney AP, Haigh SJ, Attfield MP, et al. Metal-organic framework templated electrodeposition of functional gold nanostructures. Electrochim Acta 2016;222:361–9. https://doi.org/10.1016/j.electacta.2016.10.187.

[129] Li X, Lachmanski L, Safi S, Sene S, Serre C, Grenèche JM, et al. New insights into the degradation mechanism of metal-organic frameworks drug carriers. Sci Rep 2017;7:1–11. https://doi.org/10.1038/s41598-017-13323-1.

[130] Zhu Y, Liu T, Ding C. Structural characterization of TiO2 ultrafine particles. J Mater Res 1999;14:442–6. https://doi.org/10.1557/JMR.1999.0063.

[131] Song P, Zhang XY, Sun MX, Cui XL, Lin YH. Graphene oxide modified TiO2 nanotube arrays: enhanced visible light photoelectrochemical properties. Nanoscale 2012;4:1800–4. https://doi.org/10.1039/c2nr11938b.

[132] Todaro M, Alessi A, Sciortino L, Agnello S, Cannas M, Gelardi FM, et al. Investigation by raman spectroscopy of the decomposition process of HKUST-1 upon exposure to air. J Spectrosc 2016;2016. https://doi.org/10.1155/2016/8074297.

[133] Prestipino C, Regli L, Vitillo JG, Bonino F, Damin A, Lamberti C, et al. Local

structure of framework Cu(II) in HKUST-1 metallorganic framework: Spectroscopic characterization upon activation and interaction with adsorbates. Chem Mater 2006;18:1337–46. https://doi.org/10.1021/cm052191g.

[134] Zhao Z, Kou T, Zhang L, Zhai S, Wang W, Wang Y. Dealloying induced N-doping in spindle-like porous rutile TiO2 for enhanced visible light photocatalytic activity. Corros Sci 2018;137:204–11. https://doi.org/10.1016/j.corsci.2018.03.049.

[135] Wang PF, Li ZH, Zhu YM. Research on the direct doping effect of silicon on cubic boron nitride ceramics by UV-VIS diffuse reflectance. Mater Chem Phys 2010;123:356–9. https://doi.org/10.1016/j.matchemphys.2010.05.050.

[136] Schiavello M. Heterogeneous Photocatalysis (Wiley Series in Photoscience & Photoengineering). New York, NY: 1997.

[137] López R, Gómez R. Band-gap energy estimation from diffuse reflectance measurements on sol-gel and commercial TiO2: A comparative study. J Sol-Gel Sci Technol 2012;61:1–7. https://doi.org/10.1007/s10971-011-2582-9.

[138] Nosaka Y, Nosaka AY. Reconsideration of intrinsic band alignments within anatase and rutile TiO2. J Phys Chem Lett 2016;7:431–4. https://doi.org/10.1021/acs.jpclett.5b02804.

[139] García Márquez A, Demessence A, Platero-Prats AE, Heurtaux D, Horcajada P, Serre C, et al. Green microwave synthesis of MIL-100(Al, Cr, Fe) nanoparticles for thin-film elaboration. Eur J Inorg Chem 2012;100:5165–74. https://doi.org/10.1002/ejic.201200710.

[140] Guerrero VV, Yoo Y, McCarthy MC, Jeong HK. HKUST-1 membranes on porous supports using secondary growth. J Mater Chem 2010;20:3938–43. https://doi.org/10.1039/b924536g.

[141] Al-Janabi N, Hill P, Torrente-Murciano L, Garforth A, Gorgojo P, Siperstein F, et al. Mapping the Cu-BTC metal-organic framework (HKUST-1) stability envelope in the presence of water vapour for CO2 adsorption from flue gases. Chem Eng J 2015;281:669–77. https://doi.org/10.1016/j.cej.2015.07.020.

[142] Canioni R, Roch-Marchal C, Sécheresse F, Horcajada P, Serre C, Hardi-Dan M, et al. Stable polyoxometalate insertion within the mesoporous metal organic framework MIL-100(Fe). J Mater Chem 2011;21:1226–33. https://doi.org/10.1039/c0jm02381g.

[143] Tian H, Peng J, Du Q, Hui X, He H. One-pot sustainable synthesis of magnetic MIL-

100(Fe) with novel Fe3O4 morphology and its application in heterogeneous degradation. Dalt Trans 2018;47:3417–24. https://doi.org/10.1039/c7dt04819j.

[144] Hejazi R, Mahjoub AR, Khavar AHC, Khazaee Z. Fabrication of novel type visible-light-driven TiO2@MIL-100 (Fe) microspheres with high photocatalytic performance for removal of organic pollutants. J Photochem Photobiol A Chem 2020;400:112644. https://doi.org/10.1016/j.jphotochem.2020.112644.

[145] Lv H, Zhao H, Cao T, Qian L, Wang Y, Zhao G. Efficient degradation of high concentration azo-dye wastewater by heterogeneous Fenton process with iron-based metal-organic framework. J Mol Catal A Chem 2015;400:81–9. https://doi.org/10.1016/j.molcata.2015.02.007.

[146] Li Y, Wen L, Tan T, Lv Y. Sequential Co-immobilization of enzymes in metal-organic frameworks for efficient biocatalytic conversion of adsorbed CO2 to formate. Front Bioeng Biotechnol 2019;7:394. https://doi.org/10.3389/fbioe.2019.00394.

[147] Sing KSW. Reporting physisorption data for gas/solid systems with special reference to the determination of surface area and porosity. Pure Appl Chem 1982;54:2201–18.https://doi.org/10.1351/pac198557040603.

[148] Meilikhov M, Yusenko K, Esken D, Turner S, Van Tendeloo G, Fischer RA. Metals@MOFs - Loading MOFs with metal nanoparticles for hybrid functions. Eur J Inorg Chem 2010:3701–14. https://doi.org/10.1002/ejic.201000473.

[149] Stoll S, Schweiger A. EasySpin, a comprehensive software package for spectral simulation and analysis in EPR. J Magn Reson 2006;178:42–55. https://doi.org/10.1016/j.jmr.2005.08.013.

[150] Zhao H, Joseph J, Zhang H, Karoui H, Kalyanaraman B. Synthesis and biochemical applications of a solid cyclic nitrone spin trap: a relatively superior trap for detecting superoxide anions and glutathiyl radicals. Free Radic Biol Med 2001;31:599–606. https://doi.org/10.1016/S0891-5849(01)00619-0.

[151] Villamena FA. EPR spin trapping. In: Villamena F, editor. React. Species Detect. Biol. 2nd ed., Boston, MA: Elsevier; 2017, p. 163–202.

[152] Bilski P, Reszka K, Bilska M, Chignell CF. Oxidation of the spin trap 5,5-dimethyl-1-pyrroline N-oxide by singlet oxygen in aqueous solution. J Am Chem Soc 1996;118:1330–8. https://doi.org/10.1021/ja952140s.

[153] Scott MJ, Billiar TR, Stoyanovsky DA. N-tert-butylmethanimine N-oxide is an

efficient spin-trapping probe for EPR analysis of glutathione thiyl radical. Sci Rep 2016;6:38773. https://doi.org/10.1038/srep38773.

[154] Jenkins CA, Murphy DM, Rowlands CC, Egerton TA. EPR study of spin-trapped free radical intermediates formed in the heterogeneously-assisted photodecomposition of acetaldehyde. J Chem Soc Perkin Trans 2 1997:2479–85. https://doi.org/10.1039/A702944F.

[155] Choina J, Kosslick H, Fischer C, Flechsig GU, Frunza L, Schulz A. Photocatalytic decomposition of pharmaceutical ibuprofen pollutions in water over titania catalyst. Appl Catal B Environ 2013;129:589–98. https://doi.org/10.1016/j.apcatb.2012.09.053.

[156] Wang Y, Han Q, Zhang H, Yan Y. Evaluation of the binding interactions of p-acetylaminophenol, aspirin, ibuprofen and aminopyrine with norfloxacin from the view of antipyretic and anti-inflammatory. J Mol Liq 2020;312:113397. https://doi.org/10.1016/j.molliq.2020.113397.

[157] Sibrian-Vazquez M, Escobedo JO, Lowry M, Fronczek FR, Strongin RM. Field effects induce bathochromic shifts in xanthene dyes. J Am Chem Soc 2012;134:10502–8. https://doi.org/10.1021/ja302445w.

[158] Tian H, Fan Y, Zhao Y, Liu L. Elimination of ibuprofen and its relative photo-induced toxicity by mesoporous BiOBr under simulated solar light irradiation. RSC Adv 2014;4:13061–70. https://doi.org/10.1039/c3ra47304j.

[159] Bakardjieva S, Šubrt J, Štengl V, Dianez MJ, Sayagues MJ. Photoactivity of anatase-rutile TiO2 nanocrystalline mixtures obtained by heat treatment of homogeneously precipitated anatase. Appl Catal B Environ 2005;58:193–202. https://doi.org/10.1016/j.apcatb.2004.06.019.

[160] Bacsa RR, Kiwi J. Effect of rutile phase on the photocatalytic properties of nanocrystalline titania during the degradation of p-coumaric acid. Appl Catal B Environ 1998;16:19–29. https://doi.org/10.1016/S0926-3373(97)00058-1.